Astronomy & Astrophysics manuscript no. sn2011dh
April 11, 2014

Late-time spectral line formation in Type IIb supernovae, with application to SN 1993J, SN 2008ax, and SN 2011dh

Anders Jerkstrand[1], Mattias Ergon[2], Stephen Smartt[1], Claes Fransson[2], Jesper Sollerman[2], Stefan Taubenberger[3], and Jason Spyromilio[4]

[1] Astrophysics Research Centre, School of Mathematics and Physics, Queen's University Belfast, Belfast BT7 1NN, UK
[2] The Oskar Klein Centre, Department of Astronomy, Stockholm University, Albanova, 10691 Stockholm, Sweden
[3] Max-Planck-Institut für Astrophysik, Karl-Schwarzschild-Str. 1, D-85741 Garching, Germany
[4] ESO, Karl-Schwarzschild-Strasse 2, 85748 Garching, Germany

Received.....; accepted.....

ABSTRACT

We investigate line formation processes in Type IIb supernovae (SNe) from 100 to 500 days post-explosion using spectral synthesis calculations. The modeling identifies the nuclear burning layers and physical mechanisms that produce the major emission lines, and the diagnostic potential of these. We compare the model calculations with data on the three best observed Type IIb SNe to-date - SN 1993J, SN 2008ax, and SN 2011dh. Oxygen nucleosynthesis depends sensitively on the main-sequence mass of the star and modeling of the [O I] $\lambda\lambda$6300, 6364 lines constrains the progenitors of these three SNe to the $M_{\rm ZAMS} = 12-16$ M$_\odot$ range (ejected oxygen masses $0.3 - 0.9$ M$_\odot$), with SN 2011dh towards the lower end and SN 1993J towards the upper end of the range. The high ejecta masses from $M_{\rm ZAMS} \gtrsim 17$ M$_\odot$ progenitors give rise to brighter nebular phase emission lines than observed. Nucleosynthesis analysis thus supports a scenario of low/moderate mass progenitors for Type IIb SNe, and by implication an origin in binary systems. We demonstrate how oxygen and magnesium recombination lines may be combined to diagnose the magnesium mass in the SN ejecta. For SN 2011dh, a magnesium mass of of $0.03 - 0.2$ M$_\odot$ is derived, which gives a Mg/O ratio consistent with the solar value. Nitrogen left in the He envelope from CNO-burning gives strong [N II] $\lambda\lambda$6548, 6583 emission lines that dominate over Hα emission in our models. The hydrogen envelopes of Type IIb SNe are too small and dilute to produce any noticeable Hα emission or absorption after ~150 days in the models, and nebular phase emission seen around 6550 Å is in many cases likely caused by [N II] $\lambda\lambda$6548, 6584. Finally, the influence of radiative transport on the emergent line profiles is investigated. Even as steady-state conditions set in after ~100 days, significant line blocking in the metal core remains for several hundred days, which affects the emergent spectrum. These radiative transfer effects lead to early-time blue-shifts of the emission line peaks, which gradually disappear as the optical depths decrease with time. The modelled evolution of this effect matches the observed evolution in SN 2011dh.

Key words. supernovae: general – supernovae: individual: SN 2011dh – supernovae: individual: SN 2008ax – supernovae: individual: SN 1993J – line: formation – line: identification – radiative transfer

1. Introduction

Massive stars that have retained their helium envelopes but lost all or most of their hydrogen envelopes explode as Type Ib and IIb supernovae (SNe), respectively. The Type Ib class was recognized with SN 1983N and SN 1984L (Elias et al. 1985; Uomoto & Kirshner 1985; Wheeler & Levreault 1985). Initially unclear whether these were thermonuclear or core-collapse events, identification of strong helium lines (Harkness et al. 1987), association with galactic spiral arms and HII regions (Porter & Filippenko 1987), strong radio emission (Sramek et al. 1984; Panagia et al. 1986), and oxygen lines in the nebular spectra (Gaskell et al. 1986; Porter & Filippenko 1987; Schlegel & Kirshner 1989) soon established them as originating from massive stars.

The Type IIb class was established with SN 1987K (Filippenko 1988) and the well-studied SN 1993J (Filippenko et al. 1993; Nomoto et al. 1993), after theoretical conception by Woosley et al. (1988). SNe of this type are characterized by hydrogen lines in their spectra at early times which subsequently fade away. In both Type IIb and Ib SNe, the metal and helium emission lines are significantly broader than in Type IIP SNe, as there is little or no hydrogen in the ejecta to take up the explosion energy. The light curves and spectral evolution are similar for Type IIb and Type Ib SNe (Woosley et al. 1994; Filippenko et al. 1994), a similarity further strengthened by subtle evidence of trace hydrogen in many Type Ib SNe (Branch et al. 2002; Elmhamdi et al. 2006).

A promising candidate mechanism for removing the hydrogen envelopes from the Type IIb progenitors is Roche lobe overflow to a binary companion (e.g. Podsiadlowski et al. 1992). This mechanism has the attractive property of naturally leaving hydrogen envelopes of mass $0.1 - 1$ M$_\odot$ for many binary configurations (Woosley et al. 1994), and the detection of a companion star to SN 1993J (Maund et al. 2004) gave important credibility to this scenario. However, population synthesis modeling by Claeys et al. (2011) predicted a significantly lower Type IIb rate than observed (~10% of the core-collapse rate, Li et al. (2011); Smith et al. (2011); Eldridge et al. (2013)).

Wind-driven mass loss in single stars is another candidate for producing Type IIb progenitors, but also in this scenario it is difficult to reproduce the observed rate, as this mechanism has no natural turn-off point as the envelope reaches the $0.1 - 1$ M$_\odot$ range (Claeys et al. 2011) that would give a Type IIb SN. Whereas revision of the distribution of binary system parameters could potentially change the predicted rates for SNe from

binary interaction by large factors (e.g. Sana et al. 2012), the prospects of obtaining much higher Type IIb rates from single stars is probably smaller. Recent downward revisions of theoretical Wolf-Rayet mass loss rates have also cast some doubt over the general ability of wind-driven mass loss to produce stripped-envelope core-collapse SNe (Yoon et al. 2010).

To advance our understanding of the nature of these SNe, modeling of their light curves and spectra must be undertaken. One important analysis technique is nebular phase spectral modeling. In this phase, emission lines from the entire ejecta are visible and provide an opportunity to derive information about mass and composition of the ejecta, which in turn can constrain the nature of the progenitor. The radioactive decay of ^{56}Co and other isotopes power the SN nebula for many years and decades after explosion, and modeling of the gas state allows inferences over abundances and mixing to be made. Spectral synthesis codes that solve for the statistical and thermal equilibrium in each compositional layer of the ejecta, taking non-thermal and radiative rates into account (e.g. Dessart & Hillier 2011; Jerkstrand et al. 2011; Maurer et al. 2011) can be used to compare models with observations.

Here, we report on spectral modeling of Type IIb SN ejecta in the 100 − 500 day phase, and the application of these models to the interpretation of observations of the three best observed events in the IIb class to-date; SN 1993J, SN 2008ax, and SN 2011dh. We place particular emphasis on the well-observed SN 2011dh, which exploded in the nearby (7.8 Mpc) Whirlpool Galaxy (M51) on May 31, 2011. The detection and confirmed disappearance of the progenitor star (Maund et al. 2011; Van Dyk et al. 2011; Ergon et al. 2014a; Van Dyk et al. 2013), as well as hydrodynamical modeling of the early (0-100 days) light curve (Bersten et al. 2012; Ergon et al. 2014a,b), and single-zone exploratory nebular modeling (Shivvers et al. 2013) have pointed towards a progenitor of Zero-Age Main Sequence (ZAMS) mass $M_{\rm ZAMS} \sim 13$ M$_\odot$. Such a progenitor would, with little doubt, imply a binary mechanism being responsible for the loss of the H envelope. An important additional analysis needed is modeling of the late-time spectra using stellar evolution/explosion models, which is one of the aims of this paper. With this modeling we aim to identify lines, characterize line formation processes, derive constraints on mixing and clumping, and to provide Type IIb model spectra for generic future use. In a companion paper (Ergon et al. 2014b, E14b hereafter), the observations and data reduction for SN 2011dh is presented, as well as further modeling and analysis of this SN.

2. Observational data

For our analysis we use the spectra of SN 1993J, SN 2008ax, and SN 2011dh listed in Table 1.

2.1. SN 2011dh

The observations and data reductions are described in E14b. Following Ergon et al. (2014a, E14a hereafter), we adopt a distance of 7.8 Mpc, an extinction $E_{\rm B-V} = 0.07$ mag, a recession velocity of 600 km s^{-1}, a ^{56}Ni mass of 0.075 M$_\odot$, and an explosion epoch of May 31 2011.

2.2. SN 2008ax

The spectra are from Calar Alto, Asiago, TNG (Taubenberger et al. 2011), and from MDM and MMT (Milisavljevic et al. 2010). Both sets of spectra were, up to 360 days, flux calibrated to the photometry in Taubenberger et al. (2011). We adopt a distance of 9.6 Mpc (Pastorello et al. 2008; Taubenberger et al. 2011) an extinction $E_{\rm B-V} = 0.40$ mag (Taubenberger et al. 2011), a recession velocity 565 km s^{-1} (Milisavljevic et al. 2010), a ^{56}Ni mass of 0.10 M$_\odot$ (Taubenberger et al. 2011), and an explosion of March 3 2008 (Taubenberger et al. 2011).

2.3. SN 1993J

Spectra include observations with the 1.8 m Asiago telescope (Barbon et al. 1995), which were downloaded from the SUSPECT database, and a dataset taken at the Isaac Newton Group of telescopes (ING). The first ING spectrum was reported in Lewis et al. (1994) and the remaining have been kindly provided by P. Meikle. The ING dataset includes spectra from the 2.5 m Isaac Newton Telescope (INT), with the FOS1 and IDS spectrographs (the FOS1 spectrum was presented in Lewis et al. (1994)). The IDS spectra were all taken with the same setup, the R300V grating and the EEV5 CCD, which has a dispersion of 3.1 Å per pixel and a slit width of 1.5 arcseconds, resulting in a resolution of 6.2 Å. The other spectra were taken at the 4.2 m William Herschel Telescope (WHT) with the double-armed ISIS spectrograph. The R158B and R158R gratings were used with the detectors TEK1 (24 μm pixels) and EEV3 (22.5 μm pixels) in the blue and red arm respectively, up to December 17 1993. For the later two epochs listed in Table 1 the red arm detector was changed to TEK2. The resolutions listed are the full-width-half-maxima of single unresolved lines at the slit widths employed.

All spectra were flux calibrated to match ING *BVR* photometry, or *VR* when *B* was not covered. An exception was the 283 day spectrum, where only the *I* band was covered, which was calibrated to this band. We adopt a distance of 3.63 Mpc (Freedman et al. 1994; Ferrarese et al. 2000) an extinction $E_{\rm B-V} = 0.17$ mag (E14a), a recession velocity 130 km s^{-1} (Maund et al. 2004), and a ^{56}Ni mass of 0.09 M$_\odot$ (Woosley et al. 1994, corrected for the larger distance assumed here). The explosion epoch is taken as March 28 1993 (Barbon et al. 1995).

3. Modeling

We use the code described in Jerkstrand et al. (2011) and Jerkstrand et al. (2012, J12 hereafter) to compute the physical conditions and synthetic spectra for a variety of ejecta structures. The code computes the gamma ray and positron deposition in the ejecta, solves the equations for the non-thermal energy deposition channels (Kozma & Fransson 1992), computes statistical and thermal equilibrium in each zone, and iterates with a Monte Carlo simulation of the radiation field to obtain radiative rates. Some updates to the code are specified in Appendix B.

The ejecta used here have composition as described in Sect. 3.1 and velocity/mixing structures as described in Sect. 3.2.

3.1. Nucleosynthesis

We use nucleosynthesis calculations from the evolution and explosion (final kinetic energy 1.2×10^{51} erg) of solar metallicity, non-rotating stars with the KEPLER code (Woosley & Heger 2007). These stars end their lives with most of their hydrogen envelopes intact, but as the nuclear burning after H exhaustion is largely uncoupled from the dynamic state of the H envelope (e.g. Chiosi & Maeder 1986; Ensman & Woosley 1988), the nu-

Table 1. List of observed spectra used. The phases are relative to the estimated explosion epochs.

SN	Date	Phase (days)	Wl (Å)	Resolution (Å)	Telescope (spectrograph)	Source
SN 1993J	1993-07-12	106	3380-10660	11	INT (FOS1)	Lewis et al. (1994)
	1993-07-23	117	3300-9400	11	Asiago 1.8m (B&C/300)	Barbon et al. (1995)
	1993-09-15	171	4000-9150	22	Asiago 1.8m (B&C/1200)	Barbon et al. (1995)
	1993-09-20	176	3400-9340	8	WHT (ISIS)	Meikle et al. unpublished
	1993-11-07	224	4000-8800	8	WHT (ISIS)	Meikle et al. unpublished
	1993-12-17	264	3500-9500	10	WHT (ISIS)	Meikle et al. unpublished
	1994-01-05	283	3500-9200	8	WHT (ISIS)	Meikle et al. unpublished
	1994-02-17	326	3700-9400	6	INT (IDS)	Meikle et al. unpublished
	1994-04-20	388	5600-9400	6	INT (IDS)	Meikle et al. unpublished
	1994-05-17	415	3400-9200	8	WHT (ISIS)	Meikle et al. unpublished
SN 2008ax	2008-06-11	100	3350-9300	11	TNG (DOLORES)	Taubenberger et al. (2011)
	2008-06-27	116	3300-6400	13	Calar Alto-2.2m (CAFOS,B200)	Taubenberger et al. (2011)
	2008-07-03	122	4400-7900	11	MDM/CCDS	Milisavljevic et al. (2010)
	2008-07-11	130	8800-24500	22,26	TNG (NICS)	Taubenberger et al. (2011)
	2008-07-24	143	3600-9400	24,38	Asiago 1.82m (AFOSC)	Taubenberger et al. (2011)
	2008-08-01	151	4500-7700	6	MDM/Modspec	Milisavljevic et al. (2010)
	2008-12-08	280	4200-7700	24	Asiago 1.82m (AFOSC)	Taubenberger et al. (2011)
	2008-01-25	328	4150-8000	7	MMT/Blue channel	Milisavljevic et al. (2010)
	2009-02-25	359	5200-9200	16	TNG (DOLORES)	Taubenberger et al. (2011)
	2009-04-22	415	4200-7800	11	MDM/CCDS	Milisavljevic et al. (2010)
	2009-05-16	439	4000-6500	11	MDM/CCDS	Milisavljevic et al. (2010)
SN 2011dh	2011-09-07	99	3300-10500	12	CA-2.2m (CAFOS)	E14a
	2011-10-30	152	3700-8200	10	AS-1.22m (AFOSC)	E14b
	2011-12-15	198	8900-15100	20	WHT (LIRIS)	E14b
	2011-12-19	202	3200-10000	8,15	WHT (ISIS)	E14b
	2011-12-23	206	14000-25000	55	TNG (NICS)	E14b
	2012-03-19	293	3200-9100	16	NOT (ALFOSC)	E14b
	2012-05-24	359	3440-7600	15	GTC (OSIRIS)	E14b
	2012-05-25	360	4800-10000	21	GTC (OSIRIS)	E14b
	2012-07-20	415	3600-7000	17	GTC (OSIRIS)	E14b

cleosynthesis is little affected by the late-time mass loss in the Type IIb progenitors (Roche lobe overflow begins only in the helium burning stage or later (e.g. Woosley et al. 1994)).

Table 2 lists the masses of selected elements in the ejecta for different progenitor masses. It is clear that determining the oxygen mass is a promising approach for estimating the main-sequence mass, as the oxygen production shows a strong and monotonic dependency on $M_{\rm ZAMS}$. Silicon, calcium, and magnesium also have strong dependencies on $M_{\rm ZAMS}$, but the production functions are not strictly monotonic.

The stellar evolution and explosion simulations give ejecta with distinct zones of roughly constant composition, each containing the ashes of a particular burning stage. We divide the ejecta along these boundaries, resulting in zones which we designate Fe/Co/He, Si/S, O/Si/S, O/Ne/Mg, O/C, He/C, He/N, and H, named after their most common constituent elements (the Fe/Co/He zone is sometimes also referred to as the ^{56}Ni zone). The mass and composition of these zones are listed in Appendix D.

3.2. Ejecta structure

gg A major challenge to SN spectral modeling is the complex mixing of the ejecta that occurs as hydrodynamical instabilities grow from asymmetries in the explosion itself and from the reverse shocks being reflected from the interfaces between the nuclear burning layers. In contrast to Type IIP SNe (which have $M_{\rm H-env}$ $\sim$10 M$_\odot$), the small H envelope masses ($M_{\rm H-env}$ $\sim$0.1 M$_\odot$) in Type IIb explosions render Rayleigh-Taylor mixing at the He/H interface inefficient (Shigeyama et al. 1994). The consequence is that hydrogen remains confined to high velocities ($V \gtrsim 10^4$ km s^{-1}), as evidenced by the hydrogen lines in the spectra of SN 1993J, SN 2008ax, and SN 2011dh (E14a).

However, asymmetries in the explosion itself and reverse shocks at the Si/O and O/He interfaces may still cause significant mixing of the inner layers. Linear stability analysis and 2D hydrodynamical simulations show that such mixing can be extensive, especially for low-mass helium cores (Shigeyama et al. 1990; Hachisu et al. 1991, 1994; Nomoto et al. 1995; Iwamoto et al. 1997). Such strong mixing is supported by models of many Type Ib/IIb light curves (Shigeyama et al. 1990, 1994; Woosley et al. 1994; Bersten et al. 2012, E14b). Further support for mixing comes from the similar line profiles of the various emission lines in the nebular phase.

This hydrodynamical mixing is believed to occur on macroscopic and not microscopic (atomic) scales, as the diffusion time-scale is much longer than the hydrodynamical time-scale of the ejecta (Fryxell et al. 1991; McCray 1993). While our limited understanding of the turbulent cascade cannot completely rule out that microscopic mixing occurs by turbulence (Timmes et al. 1996), there are strong indications from the chemically inhomogeneous structure of Cas A (e.g. Ennis et al. 2006), spectral modeling (Fransson & Chevalier 1989) and the survival of molecules (Liu & Dalgarno 1996; Gearhart et al. 1999) that microscopic does not occur to any large extent in SN explosions.

The consequence of the large-scale mixing is that the final hydrodynamic structure of the ejecta is likely to be significantly different from what is obtained in 1D explosion simulations. For our modeling we adopt a scenario where significant macroscopic

Table 2. Ejected element masses in the Woosley & Heger (2007) models (assuming $M_{\rm H-env}$ = 0.1 $M_\odot$ and M(^{56}Ni) = 0.075 $M_\odot$), for different $M_{\rm ZAMS}$. Ejecta that we model in this paper are marked with an asterisk (see Appendix D for detailed compositions).

$M_{\rm ZAMS}$ ($M_\odot$)	$M_{\rm total}$	$M_{\rm He}$	$M_{\rm C}$	$M_{\rm O}$	$M_{\rm Na}$	$M_{\rm Mg}$	$M_{\rm Si}$	$M_{\rm Ca}$	$M_{\rm 56Ni}$	$M_{\rm others}$
12*	1.7	1.0	0.081	0.30	8.3×10^{-4}	0.020	0.042	0.0027	0.075	0.17
13*	2.1	1.1	0.10	0.51	5.6×10^{-4}	0.043	0.063	0.0037	0.075	0.21
14	2.3	1.2	0.12	0.66	7.8×10^{-4}	0.050	0.063	0.0036	0.075	0.26
15	2.5	1.2	0.15	0.78	2.1×10^{-3}	0.045	0.065	0.0038	0.075	0.22
16	2.8	1.2	0.17	0.88	3.8×10^{-3}	0.045	0.030	0.0025	0.075	0.32
17*	3.6	1.2	0.19	1.3	6.4×10^{-3}	0.074	0.16	0.011	0.075	0.55
18	3.7	1.3	0.17	1.6	1.6×10^{-3}	0.14	0.10	0.0036	0.075	0.39

mixing is taken to occur. Lacking any published grids of multi-dimensional Type IIb simulations to use as input, we attempt to create realistic structures by dividing the ejecta into three major components, a well-mixed core, a partially mixed He envelope, and an unmixed H envelope.

3.2.1. The core

The core is the region between 0 and 3500 km s^{-1} (which as shown later gives a good reproduction of the metal emission lines profiles of the three objects studied here[1]) where complete macroscopic mixing is applied. The core contains the metal zones (Fe/Co/He, Si/S, O/Si/S, O/Ne/Mg, O/C), and, based on the mixing between the oxygen and helium layers seen in the multidimensional simulations, 0.1 $M_\odot$ of the He/C zone.

Each zone in the core is distributed over $N_{\rm cl} = 10^4$ identical clumps (see Jerkstrand et al. (2011) for details on how this is implemented). This number is constrained to be large ($N_{\rm cl} \gtrsim 10^3$) by the fine-structure seen in the nebular emission lines of SN 1993J and SN 2011dh (Matheson et al. 2000, E14b).

This mixing treatment is referred to as the "medium mixing" scenario. We also run some models where we apply an even stronger mixing by putting 50% of the Fe/Co/He zone out in the helium envelope, referred to as the "strong mixing" scenario (we do this by adding three equal-mass shells of Fe/Co/He into the He envelope between 3500 km s^{-1} and 6200 km s^{-1}, see also Sect. 3.2.2). The motivation for this strong mixing comes from constraints from the diffusion-phase light-curve, which requires significant amounts of ^{56}Ni at high velocities (Woosley et al. 1994; Bersten et al. 2012, E14b). We leave investigation of completely unmixed models for a future analysis.

We assume uniform density for the O/Si/S, O/Ne/Mg, O/C, and He/C components. The Fe/Co/He and Si/S clumps expand in the substrate due to the first days of radioactive heating and obtain a lower density (e.g. Herant & Benz 1991). In J12 a density contrast of a factor $\chi = 30$ between the Fe/Co/He zone and the other metal zones for the Type IIP SN 2004et was derived. Each model here has a density structure $1/\chi - 1/(\chi/10) - 1 - 1 - 1 - 1$ for the Fe/Co/He - Si/S - O/Si/S - O/Ne/Mg - O/C - He/C components (we allow some expansion also of the Si/S zone since it contains some of the ^{56}Ni), where we use either $\chi = 30$ or $\chi = 210$.

3.2.2. The He envelope

We place alternating shells of He/C and He/N-zone material in a He envelope between $V_{\rm core} = 3500$ km s^{-1} and $V_{\rm He/H} = 11\,000$ km s^{-1} (see Sect. 3.2.3 for this value for the He/H interface velocity). We take the density profile of the He envelope from the simulations of Bersten et al. (2012), rescaled with a constant to conserve the mass. The shells in each He/C-He/N pair have the same density, and the spacing between each pair is logarithmic with $V_{\rm i+1}/V_{\rm i} = 1.2$. When ^{56}Ni shells are mixed out into the He envelope ("strong mixing"), we take 10% of the volume of the first three pairs and allocate it to a ^{56}Ni shell (increasing the density in the He/C and He/C shells by the corresponding factor).

3.2.3. The H envelope

Outside the He envelope, we attach a H envelope between 11 000 km s^{-1} and 25 000 km s^{-1}, with mass 0.1 $M_\odot$ and mass fractions 0.54 H, 0.44 He, 1.2×10^{-4} C, 1.0×10^{-2} N, 3.2×10^{-3} O, 3.0×10^{-3} Ne, with solar abundances for the other elements. These abundances are based on the model for SN 1993J by Woosley et al. (1994), which has significant mixing of CNO ashes into the base of the H envelope (see also Shigeyama et al. (1994)), and is in agreement with observational constraints from SN 1993J (Fransson et al. 2005). This envelope mass gives a total H mass in agreement with the constraints derived from the 0 − 100 day phase by E14a.

The inner velocity of the hydrogen envelope ($V_{\rm He/H} = 11\,000$ km s^{-1}) is determined from the Hα absorption line seen during the first 100 days (E14a). We use a density profile of $\rho(V) \propto V^{-6}$, which is a rough fit to the Type IIb ejecta models by Woosley et al. (1994). The H shells are spaced logarithmically with $V_{\rm i+1}/V_{\rm i} = 1.1$ (the density profile here is steeper than in the He envelope, and we thus use a somewhat finer zoning). We terminate the envelope at 25 000 km s^{-1}, beyond which little gas is present.

3.3. Molecules

The formation of molecules has a potentially large impact on the thermal evolution of the ejecta in the nebular phase. That molecules can form in stripped-envelope SNe was evidenced by the detection of the CO first overtone in the Type Ic SN 2000ew at 100 days (Gerardy et al. 2002). A second detection was reported for the Type Ic SN 2007gr (Hunter et al. 2009), where high observational cadence showed the onset of CO overtone emission at somewhere between 50 − 70 days. For Type Ib and IIb SNe, there have been no previous detections of CO, although a feature seen around 2.3 μm in SN 1993J at 200 and 250 days (Matthews et al. 2002) could possibly be due to the CO first overtone. SN 2011dh shows an unambigous detection of this overtone (E14b).

Our code does not contain a molecular chemical reaction network, so we need to parameterize molecule formation and its impact on ejecta conditions. Here, we compute models in two

[1] A more detailed investigation of the line profiles in SN 2011dh is given in E14b.

limiting cases; complete molecular cooling of the O/Si/S and O/C layers, and no molecular cooling. In the models with molecular cooling, we follow the treatment in J12 by assuming that CO dominates the cooling of the O/C zone and SiO dominates the cooling of the O/Si/S zone. We fix the temperature evolution of these zones to be the ones derived for SN 1987A (Liu et al. 1992; Liu & Dalgarno 1994). If molecular cooling is strong, the optical/NIR spectrum is not sensitive to the exact value of this temperature.

3.4. Dust

As with molecules, formation of dust in the ejecta has a potentially large impact on physical conditions and the emergent spectral energy distribution. No clear dust detection in stripped-envelope SNe has so far been reported in the literature, although in SN 1993J, a strong continuum component, detectable in K and L' bands, arose in the SED after 100 days (Matthews et al. 2002), and was interpreted as possibly coming from dust forming in the ejecta.

The higher expansion velocity in H-poor SNe leads to two opposing effects on the thermal evolution (and thereby the dust formation epoch); the gamma-ray trapping is lower, lowering the heating rates, and the density is lower, lowering the cooling rates. The opposing trends make it difficult to predict whether dust formation would occur earlier or later than in hydrogen-rich SNe.

We compute models both with and without dust. We model the dust as a smooth gray opacity in the core region of the SN, which turns on at 200 days with a radial optical depth $\tau = 0.25$. The flux absorbed by the dust in the radiative transfer simulations is re-emitted as a blackbody with surface area $A_{\rm dust} = x_{\rm dust} A_{\rm core}$, where $x_{\rm dust}$ is a free parameter and $A_{\rm core} = 4\pi\,(V_{\rm core} t)^2$. The dust emission occurs mainly in the K band and the mid-infrared bands, and is discussed in more detail in E14b.

3.5. Positrons

About 3.5% of the ^{56}Co decay energy is in kinetic energy of positrons. Since the positron absorption cross section is much larger than the gamma-ray cross section, positrons will come to dominate the power budget when the optical depth to the gamma-rays falls below ~ 0.035. For typical ejecta masses and energies, this transition will occur after 1-2 years (e.g. Sollerman et al. 2002).

The trajectories of the positrons, and in turn the zones in which they deposit their kinetic energy in, depend on the strength and structure of the magnetic field in the ejecta, which is unknown. Here we treat the positrons in two limits; $B \rightarrow \infty$ (on-the-spot absorption) and $B = 0$ (transport assuming no magnetic deflection with an opacity $\kappa_{e+} = 8.5\left(\bar{Z}/\bar{A}/0.5\right)\,{\rm cm}^2\,{\rm g}^{-1}$ (Axelrod 1980; Colgate et al. 1980), where $\bar{A}$ is the mean atomic weight and $\bar{Z}$ is the mean nuclear charge. We refer to these two cases as "local" and "non-local".

3.6. Overview of models

Table 3 lists the properties of the various models that we run. All models have an initial ^{56}Ni mass of 0.075 $M_\odot$, a metal core between 0 and 3500 km s^{-1}, a He envelope between 3500 and 11 000 km s^{-1}, and a H envelope between 11 000 and 25 000 km s^{-1}. The models differ in progenitor mass, ^{56}Ni mixing, positron treatment, molecular cooling, dust formation, and core density contrast factor. The lowest progenitor mass in the WH07 grid is 12 $M_\odot$ which sets the lower limit to our grid. We will find that metal emission lines from $M_{\rm ZAMS} = 17\ M_\odot$ ejecta are already stronger than the observed lines in the Type IIb SNe studied here, and we therefore do not investigate models from higher masses in this work. Our progenitor mass range is therefore 12 – 17 $M_\odot$.

Table 4 shows the model combinations that differ in only one parameter, which allows comparisons of how each parameter impacts the spectrum.

All model spectra presented in the paper have been convolved with a Gaussian with $R = 300$; this serves to damp out Monte Carlo noise and is of the same order as the spectral resolution of most instruments used to collect the data.

3.7. Line luminosity measurements

In some sections we present line luminosity measurements from both observed and modelled spectra. Such quantities are not strictly well-defined for SN spectra due to strong line blending by both individual strong lines and by the forest of weak lines that make up the quasi-continuum (e.g. Li & McCray 1996). Asymmetries and offsets from the rest wavelength cause further complications. These issues make it preferable to perform the line luminosity extractions by automated algorithms, rather than "by-eye" selections of continuum levels and integration limits. The advantage of this process is that it is well defined, removes bias, and is repeatable by others. The disadvantage is that the algorithms may fail in capturing the right feature when strong blending or large offsets are present. A visual inspection of the fits is therefore always performed to limit these cases.

The algorithm we apply is as follows; for each of the three observed SNe we select a velocity $V_{\rm line}$ that represents typical emission line widths. For the SNe in this paper we use $V_{\rm line} = 3500$ km s^{-1} for SN 2011dh, $V_{\rm line} = 4500$ km s^{-1} for SN 2008ax, and $V_{\rm line} = 4500$ km s^{-1} for SN 1993J (SN 2008ax and SN 1993J have somewhat broader lines than SN 2011dh). For the models (which all have $V_{\rm core} = 3500$ km s^{-1}) we use $V_{\rm line} = 3500$ km s^{-1}. We identify the minimum flux values within $[\lambda_0^{\rm blue} \times (1 - 1.25 V_{\rm line}/c)\,, \lambda_0^{\rm blue}] = [0.985\lambda_0^{\rm blue}, \lambda_0^{\rm blue}]$ on the blue side and $[\lambda_0^{\rm red}, \lambda_0^{\rm red} \times (1 + 1.25 V_{\rm line}/c)] = [\lambda_0^{\rm red}, 1.015\lambda_0^{\rm red}]$ on the red side[2], and take the continuum to be the line connecting these points. The line luminosity is then taken as the integral of the flux minus this continuum.

While the luminosity is automatically extracted, we estimate the error bars on each measurement by manual inspection of how complex the line blending appears to be, and whether some flux could be missed due to asymmetric or offset lines. The quantity that we plot and compare between observations and models is the line luminosity relative to the ^{56}Co decay power

$$L_{\rm norm}(t) = \frac{L_{\rm line}(t)}{1.06\times10^{42}\,\frac{M_{\rm ^{56}Ni}}{0.075 M_\odot}\,(e^{-t/111.4\ d} - e^{-t/8.8\ d})\,{\rm erg\ s^{-1}}}, \quad (1)$$

which is independent of distance. For optical lines, this ratio is also insensitive to the extinction as the ^{56}Co mass is determined in a phase where the bulk of the radiation emerges in the optical bands and thus suffers the same bias as the optical line luminosity estimates. Instead, the systematic error for $L_{\rm norm}$ is dominated by the uncertainty in the ^{56}Co mass determined for a *given* distance and extinction.

[2] For lines with several components (e.g. [Ca II] $\lambda\lambda$7291, 7323) we use the shortest wavelength on the left side ($\lambda_0^{\rm blue}$) and the longest wavelength on the right side ($\lambda_0^{\rm red}$). For single lines $\lambda_0^{\rm blue} = \lambda_0^{\rm red} = \lambda_0$.

Table 3. Properties of models computed. Further description can be found in the main text of Sect. 3.

Model	M_{ZAMS} ($M_\odot$)	Mixing	e^+	Mol. cooling	Dust	Contrast factor χ
12A	12	Medium	Non-local	O/Si/S & O/C	No	30
12B	12	Strong	Non-local	None	Yes	210
12C	12	Strong	Local	None	Yes	210
12D	12	Strong	Local	O/Si/S & O/C	Yes	210
13A	13	Medium	Non-local	O/Si/S & O/C	No	30
13B	13	Medium	Local	O/Si/S & O/C	No	30
13C	13	Strong	Non-local	O/Si/S & O/C	No	30
13D	13	Strong	Non-local	O/Si/S & O/C	Yes	30
13E	13	Strong	Non-local	O/Si/S & O/C	No	210
13F	13	Strong	Non-local	None	Yes	210
13G	13	Strong	Local	None	Yes	210
17A	17	Strong	Local	None	Yes	210

Table 4. Model combinations that differ in only one parameter. The value of the parameter is given in parenthesis.

Parameter	Model combination
$M_{\rm ZAMS}$	12C (12), 13G (13), 17A (17)
	12A (12), 13A (13)
Mixing	13A (medium) and 13C (strong)
e+	12B (local) and 12C (non-local)
	13A (non-local) and 13B (local)
Mol. cooling	12C (none) and 12D (O/Si/S & O/C zones)
Dust	13C (no dust) and 13D (with dust)
Contrast factor χ	13C (χ = 30) and 13E (χ = 210)

4. Results

We review the results of the model calculations by comparing model spectra with observed ones, and discuss line formation element by element. Of the models presented in Table 3, model 12C ($M_{\rm ZAMS}$ = 12 $M_\odot$, strong mixing, local positron absorption, no molecular cooling, dust formation at 200 days, and χ = 210) shows good overall agreement with the spectral evolution of SN 2011dh (Figs. 1, 2). In particular, this model reproduces well the evolution of the [O I] $\lambda\lambda$6300, 6364 lines (Fig. 12). A dust component is necessary to reproduce the NIR spectrum at 200 days (Fig. 2), both in model 12C and in the other models (see E14b for further analysis of this dust component). Figure 3 shows that the last NIR spectrum of SN 2008ax at 130 days showed no such dust component.

4.1. Hydrogen lines

The hydrogen envelope of 0.1 $M_\odot$ receives little of the energy input from ^{56}Co, typically around 0.5% of the total deposition at all epochs in the 100−500 day range. This is too little to produce any detectable emission from Hα or from any other lines in our models. That radioactivity is unable to power Hα in the nebular phase of Type IIb SNe is a result previously discussed by Patat et al. (1995); Houck & Fransson (1996) and Maurer et al. (2010). That a strong emission line around 6550 Å is nevertheless often seen in Type IIb spectra is usually explained by powering by X-rays from circumstellar interaction. Although that process undoubtedly occurred after about a year for SN 1993J, it has proven difficult to quantitatively reproduce the luminosity and line profile evolution at earlier times (Patat et al. 1995; Taubenberger et al. 2011). In particular, a circumstellar interaction powered Hα does not reproduce the rather narrow emission line profile usually seen, as hydrogen is confined to velocities over $\sim 10^4$ km s^{-1}. In our models, a strong line in this spectral region is instead produced by [N II] $\lambda\lambda$6548, 6583, arising as cooling lines from the He/N layers (Fig. 6, Sect. 4.4), removing the need for any Hα component at all.

Some caution is needed in drawing conclusions from steady-state modeling of Hα, because the dilute hydrogen envelope is the first region to be affected by time-dependent effects. Its low density leads to both cooling and recombination time-scales becoming comparable to, and then exceeding, the radioactive decay time scale. Figure 7 shows the ratio of recombination time to radioactive decay time scale ($\tau_{\rm rec}/\tau_{\rm 56Co}$), and the adiabatic cooling relative to the total cooling for the inner hydrogen envelope shell in model 12C. We see that breakdown of the steady-state assumption (that both of these ratios are $\ll$ 1) begins at 150-200 days. This breakdown will lead to temperature and ionization balance differing from those obtained in steady-state calculations (Fransson & Kozma 1993). Whether the H emission may become strong enough to be detectable under the influence of this time-dependence has to be investigated with such modeling. We note, however, that the ionization level in the steady-state model is $x_{\rm HII} \sim x_{\rm e} \gtrsim 1/4$ over the 100-300 day interval (Fig. 7) and so even in a situation of complete ionization ($x_{\rm HII} \sim x_{\rm e} \sim 1$), the recombination lines would be at most a factor 10-20 brighter (as the recombination rate scales with $x_{\rm HII} \cdot x_{\rm e}$). As Fig. 6 shows, a factor 10 increase in Hα would still be too little to match the observed luminosity. It therefore appears to be a robust result that (^{56}Co-powered) Hα is undetectable after ~200 days in Type IIb SNe.

In the models all lines in the Balmer series (and higher n) are optically thin after ~150 day thereby preventing any scattering components to form. Our conclusion is therefore that the hydrogen envelope cannot affect the spectrum neither by emission nor absorption by H lines after ~150 days. This result is in agreement with the SN 1993J analysis by Houck & Fransson (1996), who found that the Hα emission in their models was inadequate to account for the observed flux around 6550 Å. In the Houck & Fransson (1996) models N II was not included, and the inclusions of this ion in the models presented here resolves the apparent discrepancy regarding the nature of the 6550 Å feature.

In SN 1993J, circumstellar interaction started dominating the output of the SN after about a year, leading to a leveling off in all photometric bands to almost constant flux levels (e.g. Zhang et al. 2004). The 6500-6600 region then became dominated by Hα from circumstellar interaction, showing a broad and boxy

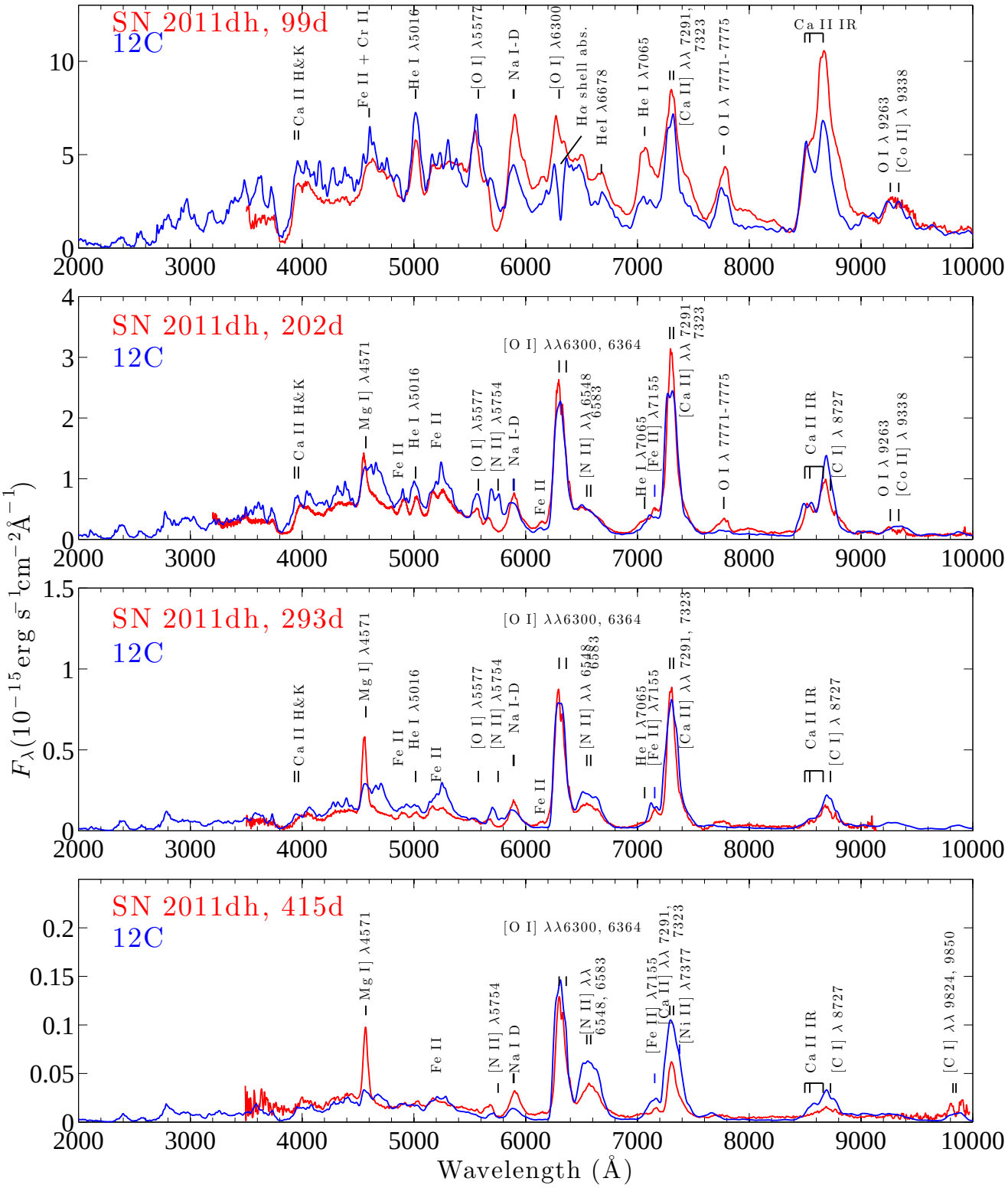

Fig. 1. SN 2011dh (dereddened and redshift corrected) at 99 days (top), 202 days (second panel), 293 days (third panel), and 415 days (bottom) (red) and model 12C at 100, 200 300, and 400 days (blue), scaled with exponential factors $\exp(-2\Delta t/111.4)$, where Δt is the difference between observed and modelled phase (here $\Delta t = -1, +2, -7, +15$ days). The decay rate of double the ^{56}Co rate corresponds to the flux evolution in most photometric bands (E14b).

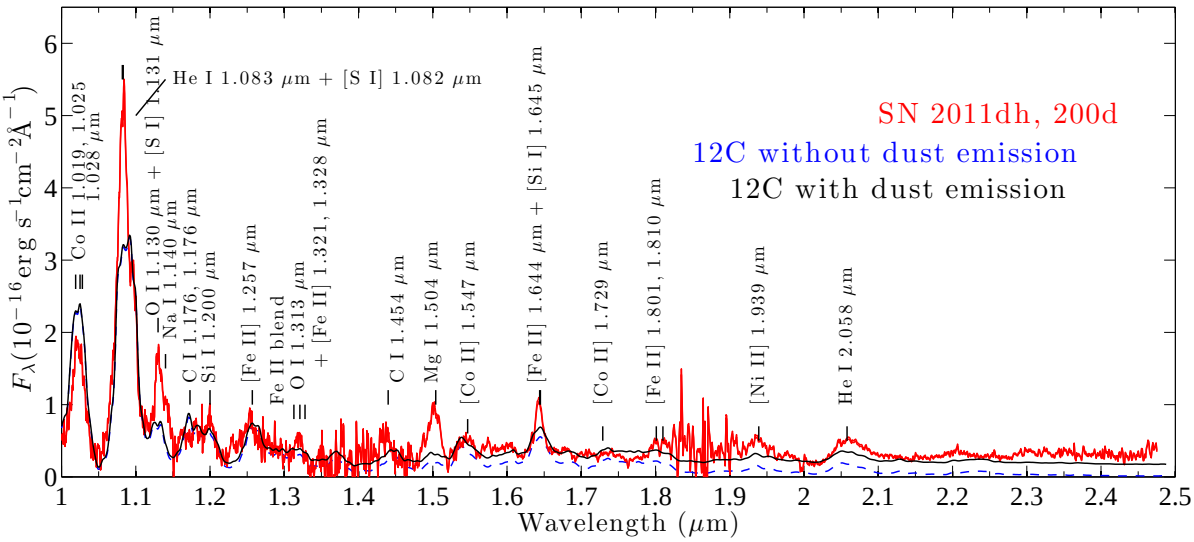

Fig. 2. SN 2011dh (dereddened and redshift corrected) in the NIR at 200 days (red; The observed spectrum is composed of 1-1.5 μm observations at 198 days scaled with $\exp(-2\times2/111.4)$ and 1.5 − 2.5 μm observations at 206 days, scaled with $\exp(+2\times6/111.4)$) and model 12C without (blue) and with (black) a dust component (τ = 0.25, $V_{\rm dust}$ = 3500 km s^{-1}, $x_{\rm dust}$ = 0.05). Line identifications from the model are labelled. A dust component clearly improves the fit above 1.5 μm.

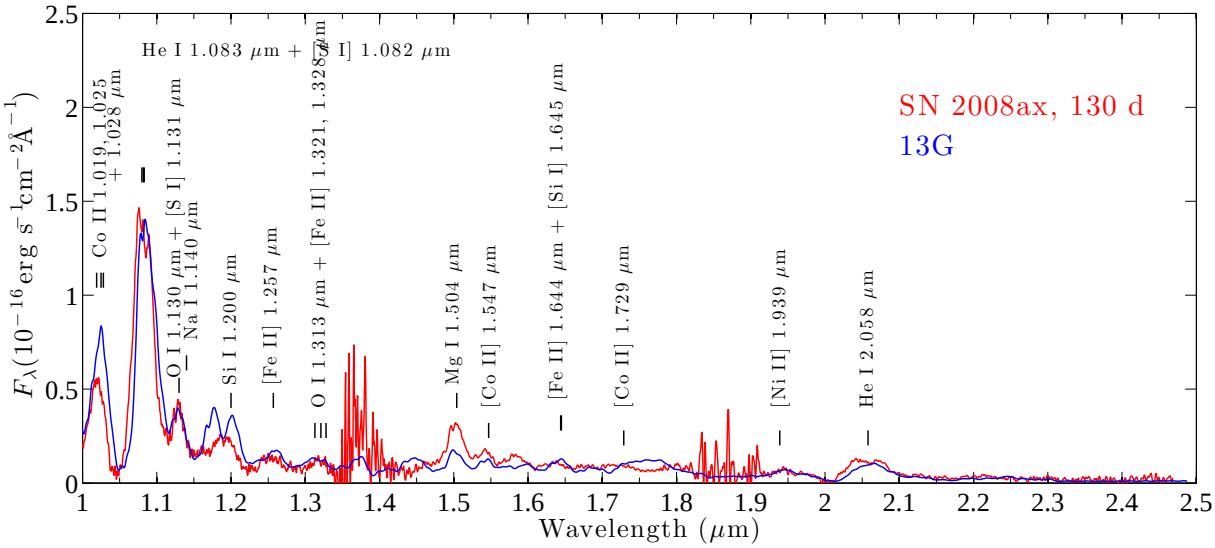

Fig. 3. SN 2008ax (dereddened and redshift corrected) in the NIR at 130 days (red) and model 13G at 150 days (rescaled to 130 days, and rescaled with a factor 1.33 to compensate for the higher ^{56}Ni mass, blue). Line identifications from the model are labelled.

line profile with almost constant flux (Filippenko et al. 1994; Patat et al. 1995; Houck & Fransson 1996). This interpretation was validated by similar Hβ and Hγ emission lines emerging in the spectrum. No such flattening was observed in SN 2011dh, at least up to 500 days, and the spectral region continues to be dominated by the [N II] $\lambda\lambda$6548, 6583 lines from the ejecta.

Before ∼150 days, Hα is optically thick and will affect the spectrum with absorption (Houck & Fransson 1996; Maurer et al. 2011). If the bulk of the photons are emitted from a core region with a velocity scale much smaller than the inner velocity of the H-envelope, this absorption will be in the form of a band centered at $\lambda_{\rm c} \sim 6563\times(1-V_{\rm H}/c) \sim 6320$ Å (using $V_{\rm H} = 1.1\times10^4$ km s^{-1}), with a width governed by the velocity distribution of both the hydrogen layer and the emitting region. The width will roughly correspond to the larger of these velocity scales. Since they are both of order a few thousand km s^{-1}, the width of the absorption band will be $\Delta\lambda \sim 2\Delta V/c\lambda_{\rm c} \sim 150$ Å, where we have used $\Delta V \sim 3500$ km s^{-1}. SN 2008ax, and SN 2011dh all exhibit distinct absorption bands throughout the 0 - 100 day evolution (E14a), all with absorption minima corresponding to $V_{\rm H} \sim 10^4$ km s^{-1}, and the identification with Hα secured by a similar band seen in Hβ. Whereas the feature continuously fades in SN 2008ax and SN 2011dh, it remains strong in SN 1993J, which is plausible given the higher hydrogen envelope mass in this SN, 0.2 − 0.4 M$_\odot$ (Woosley et al. 1994; Houck & Fransson 1996).

The absorption band emerges in the models at 100 days (Figs. 1, 6). The absorption begins around 6350 Å, ($\approx \lambda_{\rm c}$ +

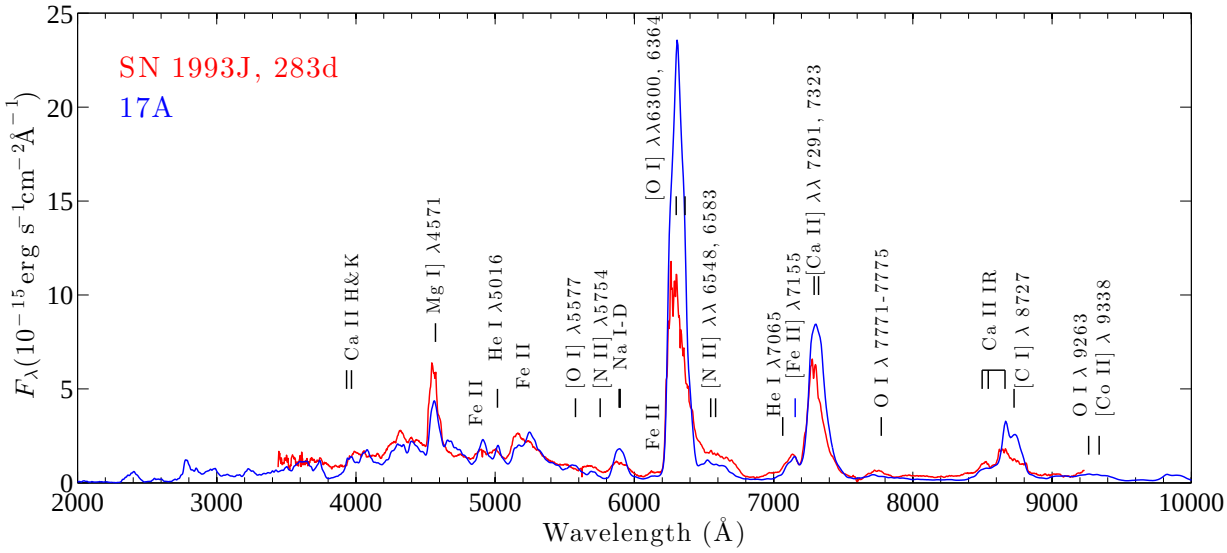

Fig. 4. SN 1993J (dereddened and redshift corrected) at 283 days (red), and model 17A at 300 days, rescaled to 283 days and rescaled with factor 1.2 to compensate for the higher ^{56}Ni mass (blue).

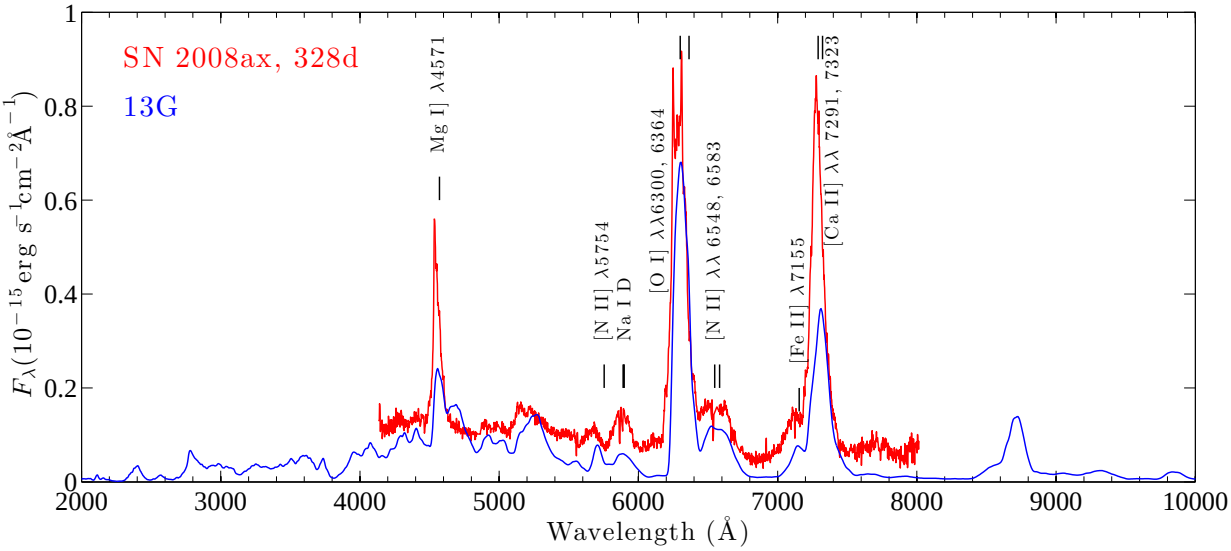

Fig. 5. SN 2008ax (dereddened and redshift corrected) at 328 days (red), and model 13G at 300 days, rescaled to 328 days and rescaled by 1.33 to compensate for the higher ^{56}Ni mass (blue).

$1/2\Delta\lambda$ = 6390 Å), reaches its maximum at 6315 Å ($\approx \lambda_c$ = 6320 Å) and ceases at 6260 Å ($\approx \lambda_c - 1/2\Delta\lambda$ = 6250) Å. The observed profile shows a similar structure, with a minimum at 6325 Å, a possible cut-off to the left at 6275 Å, but no clear cut-off to the right. The region is complex, with an [Fe II] line contributing on the red side as well. The absorption in the model is stronger than in the observed spectrum, and it is therefore unlikely that the hydrogen density in the model is underestimated. Finally, we note that Hβ and the other Balmer lines are optically thin in the model in the time interval studied here, and therefore do not produce similar absorption bands (which would be positioned at $\sim$ 4690 Å and 4180 Å for Hβ and Hγ.)

4.2. Helium lines

He line formation in the nebular phase is complex, as He is present in several compositionally distinct regions in the SN. CNO-burning leaves the progenitor with a He/N layer enriched in nitrogen and depleted in carbon. The inner parts of this zone later goes through incomplete (shell) helium burning, which destroys nitrogen and burns some of the helium to mainly carbon. The resulting He/C layer is then macroscopically mixed to an uncertain extent into the core, as the O/C-He/C interface gives rise to Rayleigh-Taylor instabilities in the explosion (Iwamoto et al. 1997). Freeze-out from nuclear statistical equilibrium in the explosive burning also leaves a large mass fraction (20 – 50%) of He in the ^{56}Ni clumps. Despite the much lower mass of He in these clumps compared to that in the He/N and He/C zones, this

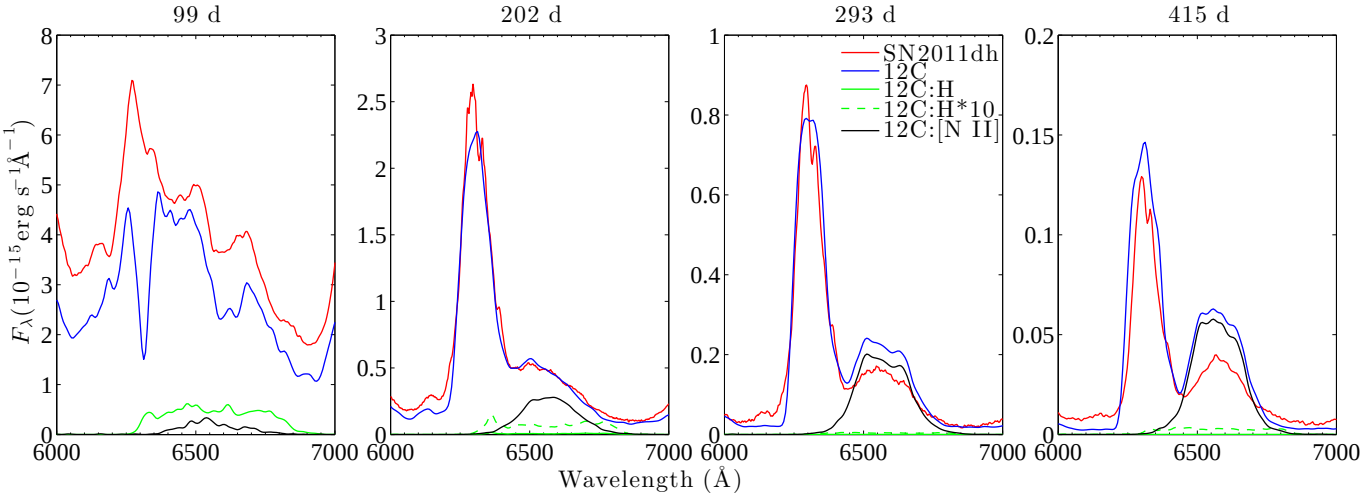

Fig. 6. Same as Fig. 1, zoomed in at 6000-7000 Å, and also showing the [N II] $\lambda\lambda$6548, 6583 contribution (black), the H contribution (green), and the H contribution multiplied by 10 (dashed green) to the model spectrum. From 200 days and on, the [N II] $\lambda\lambda$6548, 6583 lines are fully responsible for the feature between 6400 – 6700 Å.

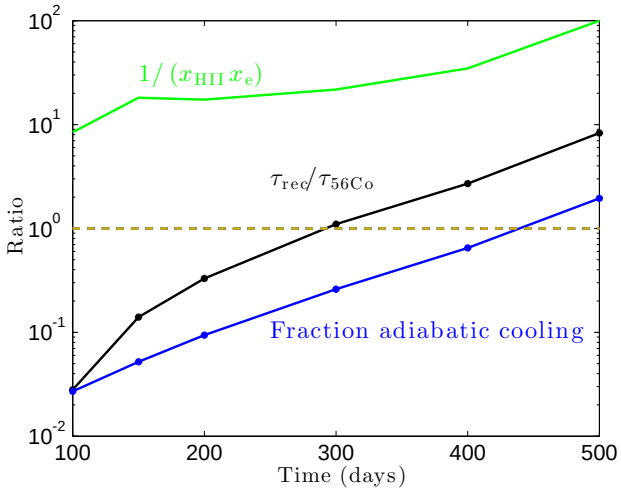

Fig. 7. The hydrogen recombination time-scale $\tau_{\rm rec} = (\alpha n_{\rm e})^{-1}$ relative to the ^{56}Co decay time scale ($\tau_{56\rm Co}$=111.4 days) (black), the adiabatic cooling relative to the radiative cooling (blue), and the quantity $1/(x_{\rm HII}x_e)$, all in the innermost H shell in model 12C.

He can contribute to the total He line emission if local trapping of the decay products is efficient (e.g. Kjær et al. 2010).

He-line analysis must thus consider contributions from three distinct zones (and possibly from the He in the H envelope as well). We find the He/C and He/N zones in the envelope and the He in the ^{56}Ni clumps to all significantly contribute to the He lines, with a smaller contribution by the He/C clumps mixed into the core.

4.2.1. He I λ1.083 μm and He I λ2.058 μm

In Fig. A.1 we plot the contribution of He lines to the model spectrum at 100, 300 and 500 days. At all epochs, He I λ1.083 μm is the strongest He emission line in the models. There is however some blending of this line with [S I] λ1.082 μm (Fig. A.3), particularly at late times. This conclusion was also reached for SN 1987A (Li & McCray 1995; Kozma & Fransson 1998), and the presence of a strong line here also in Type Ic SNe is explained by this sulphur line (Mazzali et al. 2010). He I λ2.058 μm does not suffer from any significant line blending in the models, and detection of this line therefore appears less ambiguous for establishing the presence of He in the SN ejecta.

The lower levels of the He I λ1.083 μm and He I λ2.056 μm lines (2s(^{3}S) and 2s(^{1}S), respectively) are meta-stable. Having only weak radiative de-excitation channels to the ground state ($A = 1.1 \times 10^{-4}$ s^{-1} and $A = 51$ s^{-1} (two-photon), respectively), these level populations become quite high, being limited by excitation and ionization processes rather than radiative de-excitation. The result is significant optical depths in the transitions; they are both optically thick throughout the helium envelope at 200 days. This optical depth means that both lines have scattering components, which are seen in the observed lines in SN 2011dh at 88 days (E14a) and 200 days (Fig. 2). At later times He I λ1.083 μm stays optically thick, whereas He I λ2.058 μm becomes optically thin (Fig. 9), as its two-photon decay channel becomes significant.

The populations of the meta-stable levels are high enough that some cooling occurs from them. In general the He I λ1.083 μm and He I λ2.058 μm lines have contributions from both scattering, recombination, non-thermal excitation, and collisional excitation. Figure 8 gives some insight into the formation of these lines by showing the various populating processes in the innermost He/N shell in model 13G at 100, 200 and 300 days. The He I λ2.058 μm line is mainly driven by cascades from levels above as well as some thermal excitation at early times and non-thermal excitations and later times. The situation is somewhat different for He I λ1.083 μm. Its parent state has a much smaller high-energy collisional cross section with respect to the ground state and non-thermal excitations are negligible. There is instead an important contribution by thermal collisional excitation from the meta-stable 2s(^{3}S) state. The cooling done by this transition is a few percent of the total cooling in the time interval studied here. Collisional excitation is less efficient for He I λ2.058 μm, because the 2s(^1S) state has in general a significantly lower population than 2s(^{1}S), as it can be emptied via twophoton decay with $A = 51$ s^{-1} (the two-photon decay channel of 2s(^{3}S) is inefficient ($A \sim 10^{-9}$ s^{-1}, Li & McCray (1995)).

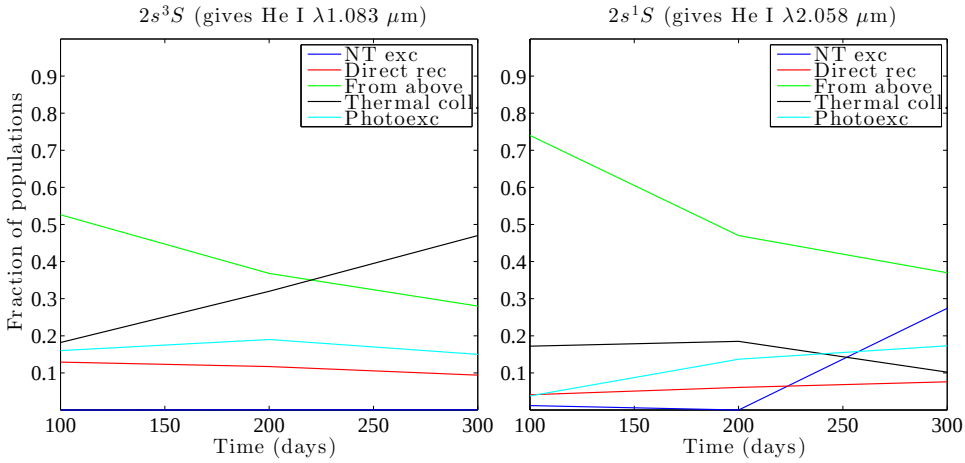

Fig. 8. Relative importance of processes that populate the parent states of He I λ1.083 μm and He I λ2.058 μm, in the innermost He/N shell in model 13G.

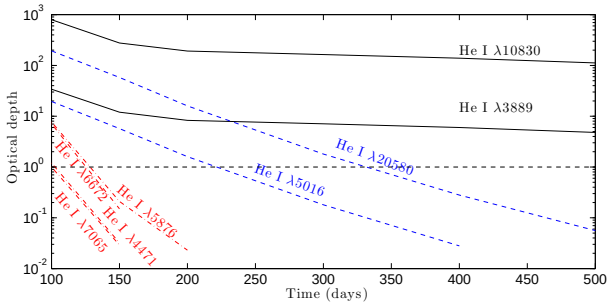

Fig. 9. Optical depths of He I lines over time, in the innermost He envelope of model 12C. Lines from the meta-stable 2s(^{3}S) are marked in solid black, from the meta-stable 2s(^{1}S) in dashed blue, and from non-metastable states in dash-dotted red.

Model 12C gives a reasonable reproduction of the He I NIR lines in SN 2011dh at 200 days, although the observed lines have more flux at in particular low velocities (Fig. 2). For the He I λ1.083 μm line, it is possible that this contribution is from (an underproduced) S I rather than He. Model 13G (which has very similar He lines) gives good agreement with SN 2008ax at 130 days (Fig. 3), which has more of a flat-topped He I λ1.083 μm line. Both these SNe are therefore in good agreement with models having $\sim$ 1 M$_\odot$ of helium in the ejecta.

4.2.2. Optical helium lines

In the optical, the strongest lines in the models are He I λ5016, He I λ6678, and He I λ7065 (Fig. A.1). All of these are present at 100 days in SN 2011dh (Fig. 1). At later times the optical helium lines quickly diminish in strength and are harder to detect. Fig. 9 shows how the optical depths in He I λ3889 and He I λ5016 stay high in the nebular phase; the reason is that these lines have one of the meta-stable states as lower levels. He I λ3889 and He I λ5016 are thus expected to have the strongest absorption components in the optical regime. Whereas He I λ3889 is difficult to disentangle from the Ca II H&K lines, a strong scattering component of He I λ5016 is seen up to at least 300 days in SN 2011dh (Fig. 1). Late-time modeling of this line may be able to further constrain the helium mass and distribution.

The other optical lines (He I λ4471, He I λ5876, He I λ6672 and He I λ7065) do not have meta-stable lower states, and although some are still optically thick at 100 days, by 150 days they are all optically thin. One consequence is that the absorption seen around 5800 Å (Fig. 1) is not due to He I λ5876 after 150 days, but rather due to Na I-D. He I λ5876 emission also does not emerge directly in the model, as most of its flux scatters in these Na I-D lines (Sect. 4.6).

4.3. Carbon lines

Figure A.1 shows the contribution by carbon (dominated by C I emission) to the spectrum. At all times significant emission is only redward of 8000 Å. At 100 days there is a large number of intermediate strength lines, but later the C I spectrum is dominated by [C I] λ8727 and [C I] $\lambda\lambda$9824, 9850. Also C I λ1.176 μm and C I λ1.454 μm are relatively strong in the models, and at least C I λ1.454 μm appears to be detected in SN 2011dh (Fig. 2).The emission is mainly from the carbon in the O/C zone, but there is also a contribution from the carbon in the He/C zone (Fig. A.7).

The presence of either [C I] λ8727 or [C I] $\lambda\lambda$9824, 9850 in the observed spectra is difficult to ascertain; [C I] λ8727 is blended with the strong Ca II λ8662 line, and the spectral region covering [C I] $\lambda\lambda$9824, 9850 has poor observational coverage. In SN 2008ax, the day 280 spectrum covers the region, and shows a feature that coincides with the line. The day 299 spectrum of SN 1993J, however, shows no distinct line at this wavelength. Spectra of SN 2011dh at 360 and 415 days cover the wavelength regime, but are noisy and difficult to interpret. The day 415 spectrum appears to show two lines, one that peaks at ~9800 Å and one that peaks at ~9900 Å.

Both [C I] λ8727 and [C I] $\lambda\lambda$9824, 9850 are cooling lines, and are therefore sensitive to CO formation in the O/C zone. Without CO, the C I lines are strong as a significant amount of cooling in this zone occurs through this channel. In model 13G, the neutral fraction of carbon is 26, 75, and 88% at 100, 300 and 500 days, and C I does ~20% of the cooling. Significant CO formation will however quench these lines as CO would take over most of the cooling. Model 12C (which has no CO cooling) does a quite good reproduction of the Ca II IR + [C I] λ8727 blend, although there is a growing overproduction with time, possibly as CO cooling becomes more and more important. Models with full CO cooling have the opposite problem, with an underproduced Ca II IR + [C I] λ8727 line at early times (Sect. 5.1.4).

4.4. Nitrogen lines

4.4.1. [N II] $\lambda\lambda$6548, 6583

As discussed in Sect. 4.1, cooling of the $\sim$1 $M_\odot$ He/N envelope by [N II] $\lambda\lambda$6548, 6583 is responsible for almost all emission in the 6400-6800 Å range in the models, exceeding the Hα contribution by large factors after 150 days (Fig. 6). The [N II] lines naturally obtain somewhat flat-topped profiles as most of the He/N layers expand with high velocities (3500-11 000 km s^{-1}), but an important distinction to the Hα component is that Hα must be flat-topped over a larger wavelength range $\sim$6320-6800 Å since H is confined to $V > 11000$ km s^{-1}, whereas the minimum He/N velocity of 3500 km s^{-1}corresponds to a flat top between 6490-6640 Å. Figs. 1 and 3 show that the observed line profiles in SN 2008ax and SN 2011dh have flat-topped parts extending out to between $\sim$6600-6650 Å, in better agreement with an interpretation as originating in the He envelope than in the H envelope. The discrepancy between interpreting the emission in this range with Hα was originally pointed out by Taubenberger et al. (2011). Figure 4 shows that SN 1993J has a flat-topped part that extends to somewhat longer wavelengths ($\sim$ 6700 Å), and combined with the lower H velocities in this SN the situation is more ambiguous.

Our models satisfactorily reproduce the [N II] $\lambda\lambda$6548, 6583 feature in SN 2011dh, both in terms of luminosity and line profile (Fig. 6). The observed profile is initially flat-topped (as in the models) but becomes less so with time; this possibly indicates that some of the He/N zone is mixed into the core (the models have only a mixed-in He/C component). Satisfactory reproduction is also achieved for SN 1993J and SN 2008ax (Figs. 4 and 5). However, by 400 days Hα has completely taken over in SN 1993J (Fig. 10) due to strong circumstellar interaction; note how the line profile expands to a flat-topped region out to 6750 Å ($V_{\rm exp} \sim 9000$ km s^{-1}).

Since the [N II] identification is an important result, it is warranted to attempt to understand how robust it is. A first question to consider is the mass and composition of the He/N layer. All WH07 models in the $M_{\rm ZAMS} = 12 - 20$ $M_\odot$ range have total He zone masses between $1.1 - 1.3$ $M_\odot$. The fraction that is still rich in N, i.e. has not been processed by helium shell burning, is 80% at the low-mass end and 30% at the high mass end. The mass of the He/N layer thus varies by about a factor two over the $12 - 20$ $M_\odot$ range, from 0.9 to 0.4 $M_\odot$. The prediction would be, assuming all other things constant, that ejecta from lower mass stars would have stronger [N II] $\lambda\lambda$6548, 6583 emission lines.

The nitrogen abundance in the He/N layer is about 1% (by mass). The abundance of other possible cooling agents (carbon, oxygen, magnesium, silicon and iron) are $\sim$0.1%. Helium makes up $\sim$98% of the zone mass, but being a poor coolant itself, the He/N layers are quite hot compared to the other zones. The fraction of the nitrogen that is singly ionized is close to unity in all models at all times, so there should not be any strong sensitivity to the ionization balance. Combining these results - moderate variations in the predicted mass of the He/N layer, a robust prediction for a high temperature, and weak sensitivity to the nitrogen ionization balance, strong [N II] $\lambda\lambda$6548, 6583 emission appears to be a robust property of the models.

If [N II] $\lambda\lambda$6549, 6583 is predicted to be a strong line in the nebular phase of helium-rich SNe, we would expect to see it in both Type IIb and Type Ib SNe. While the emission line is strong in the three Type IIb objects studied here as well as in the Type IIb SNe 2011ei (Milisavljevic et al. 2013) and 2011hs (Bufano et al. 2014), it appears dim or absent in SN 2001ig (Silverman et al. 2009) and SN 2003bg (Hamuy et al. 2009; Mazzali et al. 2009). Also for Type Ib SNe, some have spectra that exhibit this line (e.g. SN 1996N (Sollerman et al. 1998) and SN 2007Y (Stritzinger et al. 2009)), while others (e.g. SN 2008D (Tanaka et al. 2009) and SN 2009jf (Valenti et al. 2011)) do not. One possible explanation for the lack of this line in some He-rich SNe could be that the He/N zone (but not the interior He/C zone) has been lost due to stellar winds or binary mass transfer. Another explanation could be that helium shell burning has engulfed the entire He/N envelope in these stars and depleted the nitrogen.

4.4.2. [N II] λ5754

In Fig. A.2 we plot the contribution by nitrogen lines to the spectrum. The only other nitrogen line emitting at detectable levels is [N II] λ5754, which in many ways is analogous to the [O I] λ5577 line (both arise from the second excited state and are temperature sensitive). The red side of this line is scattered by the Na I-D lines (Fig. 11). There is an emission feature in all SN 2011dh spectra centered at $\sim$ 5670 Å that we identify with this blue edge of [N II] λ5754 (Fig. 1) - it is also seen in SN 1993J and SN 2008ax (Fig. 10). The blue edge goes to $\sim$5600 Å in the observed spectra which would correspond to an expansion velocity of $\sim$8000 km s^{-1}, making an identification with the helium envelope as the source of the emission plausible. Furthermore, our models confirm that Na I-D is optically thick throughout the He envelope throughout the period studied here (Sect. 4.6). The predicted absorption cut is thus around 5890 Å $\times$ $(1 - 1 \times 10^4/3 \times 10^5) \sim$ 5700 Å (see also Fig. 11), in good agreement with the observed line.

The [N II] λ5754 line luminosity in the model at 400 days matches the observed one reasonably well, although the line profile it is too narrow (Fig. 1). No other emission lines are predicted in the relevant range, further strengthening the identification. However, at 200 and 300 days the line is too strong (Fig. 1). As [N II] λ5754 is more temperature-sensitive than [N II] $\lambda\lambda$6548, 6584, this can be caused by an even slightly too high model temperature in the He/N layers. The model temperatures are between 10 000-12 000 K in the various He/N shells at 200 days. Since [N II] λ5754 is more temperature sensitive than [N II] $\lambda\lambda$6548, 6584, a lower temperature would decrease or eliminate [N II] λ5754 while affecting [N II] $\lambda\lambda$6548, 6584 less (compare to how [O I] λ5577 rapidly disappears as the SN evolves while [O I] $\lambda\lambda$6300, 6364 persists). Thus, the model overproduction of [N II] $\lambda\lambda$5754 does not per-se invalidate the [N II] $\lambda\lambda$6548, 6584 identification.

After $\sim$ 400 days, the model starts overproducing the [N II] $\lambda\lambda$6548, 6583 doublet compared to observations of SN 2011dh. While adiabatic cooling is still only 1-12% in the various He/N layers at 300 days, by 400 days it has reached 3-26%, and the steady-state assumption starts breaking down in the outer layers. It is thus plausible that the temperature computed with our steady-state models starts overestimating the true temperature in the outer helium envelope at $\sim$400 days.

4.5. Oxygen lines

The oxygen lines that emerge in the models are [O I] λ5577, [O I] $\lambda\lambda$6300, 6364, O I λ7774[3], O I λ9263[4], O I λ1.129 μm + O I λ1.130 μm and O I λ1.316 μm (Fig. A.2). Inspection of the

[3] Three lines between 7771-7775 Å.

[4] Nine lines between 9261-9266 Å.

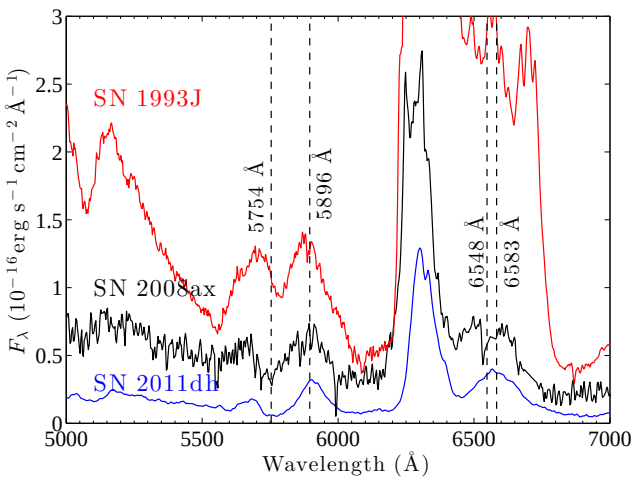

Fig. 10. The 5000 - 7000 Å region at 415 days in SN 2011dh (blue), SN 2008ax (black) and SN 1993J (red), all dereddened, redshift corrected, and scaled to the same distance (7.8 Mpc). We identify the feature at ~5700 Å with the blue side of [N II] λ5754, with the red side being lost in scattering into Na I-D.

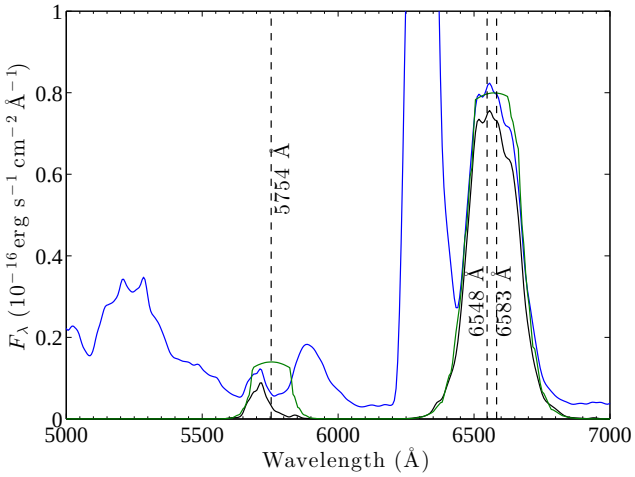

Fig. 11. The [N II] emissivity in model 12C at 400 days (green), and the N II photons that emerge in the radiative transfer simulation (black). Note how most of the [N II] λ5754 emission is absorbed (by Na I D in the He envelope). Total emergent spectrum in blue.

various populating mechanisms show that [O I] λ5557 and [O I] $\lambda\lambda$6300, 6364 are mainly driven by thermal collisional excitation at all times, as they are close to the ground state and in addition radiative recombination to singlet states from the O II ground state is forbidden. The O I λ7774, O I λ9263, O I λ1.129 + λ1.130 μm and O I λ1.316 μm lines are on the other hand mainly driven by recombination.

4.5.1. [O I] $\lambda\lambda$6300, 6364

Figure 12 shows the luminosity of [O I] $\lambda\lambda$6300, 6364 (relative to the ^{56}Co decay power) for SN 2011dh, SN 2008ax, and SN 1993J[5], and in the models. All three SNe show luminosities in this line that is bracketed by the model luminosities from $M_{\rm ZAMS}$ = 12 − 17 M$_\odot$ progenitors, in which the oxygen mass range is $M_{\rm O}$ = 0.3 – 1.3 M$_\odot$. SN 1993J has the brightest normalized oxygen luminosity, roughly halfway between the 13 and 17 M$_\odot$ models, suggesting a ~15 M$_\odot$ progenitor ($M_{\rm O}$ = 0.8 M$_\odot$). In the WH07 models, oxygen production grows sharply for progenitors over ~16 M$_\odot$, and as the comparison with the 17 M$_\odot$ model shows, none of these SNe exhibit the strong [O I] $\lambda\lambda$6300, 6364 lines expected from the ejecta from such high-mass stars. Figure 4 shows model 17A compared to SN 1993J at 300 days - there is reasonable overall agreement with this model, but the oxygen lines are about a factor two too strong.

An important quantity to attempt to constrain is the oxygen zone density, which is possible if the optical depths of the [O I] $\lambda\lambda$6300, 6364 lines can be determined. In SN 1987A, the [O I] $\lambda\lambda$6300, 6364 lines began to depart from the optically thick 1:1 regime already at 100 days, and passed τ = 1 around 400-500 days (Spyromilio & Pinto 1991; Li & McCray 1992). Since the expansion velocities here are about a factor two higher, the densities for a similar oxygen mass and filling factor are a factor eight lower. As the optical depths evolve as t^{-2}, the τ = 1 limit is then expected to be reached by 400/ $\sqrt{8}$ ~150 days instead of 400 days.

Since the expansion velocity of the metal core of the SN is greater than the 3047 km s^{-1} separating the [O I] λ6300 and [O I] λ6364 lines, the two lines are blended and the individual components of the doublet cannot be directly extracted. Figure 13 shows the best fit to the doublet line profile in SN 2011dh for an optically thin (black) and an optically thick (blue) model with Gaussian components. The optically thin version gives a better fit at all times, although at 100 days neither fit is good, likely due to line blending and radiative transfer effects (see Sect. 4.16 for more on this). If we take the lines to have entered the optically thin regime at 150 days, and use the Sobolev expression for the optical depth (ignoring the correction for stimulated emission)

$$\tau_{6300} = \frac{A_{6300}\lambda^3}{8\pi}\frac{g_{\rm up}}{g_{\rm low}} t n_{\rm low} \ , \qquad (2)$$

we obtain, with A_{6300} = 5.6 × 10^{-3} s^{-1}, λ = 6300 × 10^{-8} cm, $g_{\rm up}$ = 5 (the statistical weight of the upper level), $g_{\rm low}$ = 5 (the statistical weight of the lower level), and $n_{\rm low} = \frac{5}{9}\rho_i/16m_p$ [6] an upper limit to the density of the oxygen of $\rho_{\rm O} < 7 \times 10^{-14}$ g cm^{-3} at 150 days. This limit is satisfied by all the models computed here, which have $\rho_{\rm O}$ between (0.8 − 5) × 10^{-14} g cm^{-3} at 150 days. For the oxygen masses in the ejecta from 12, 13 and 17 M$_\odot$ progenitors (0.3, 0.5 and 1.3 M$_\odot$), this limit corresponds to filling factor limits $f_{\rm O} \gtrsim 0.02, 0.04$ and 0.09 (for $V_{\rm core}$ = 3500 km s^{-1}). Additional constraints on the oxygen zone filling factor from small-scale fluctuation in the line profiles is derived in E14b, this analysis gives a constraint $f_{\rm O} < 0.07$, which is already in tension with the minimum filling factor needed for the 17 M$_\odot$ model. Independent of luminosity, these constraints from the line-profile structure of [O I] $\lambda\lambda$6300, 6364 therefore constrain the thermally emitting oxygen mass in SN 2011dh to less than 1.3 M$_\odot$.

4.5.2. [O I] λ5577

[O I] λ5577 arises from 2p^4(^{1}S) which is 4.2 eV above the ground state and is efficiently populated by thermal collisions in the early nebular phase, when the temperature is high. Since

[5] For SN 1993J, we include data up to about one year, after which circumstellar interaction began to dominate the spectrum.

[6] Assuming most oxygen is neutral and in an LTE ground multiplet, and approximation which is validated by the model calculations.

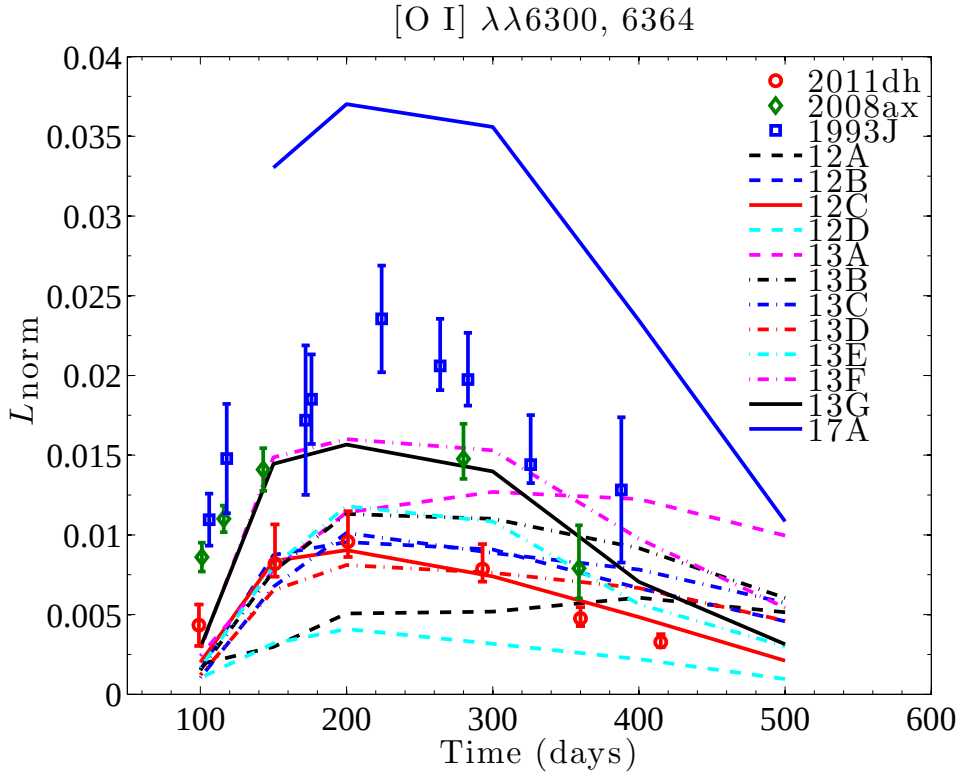

Fig. 12. The luminosity in [O I] $\lambda\lambda$6300, 6364 normalized to the total ^{56}Co decay power (see Eq. 1) for SN 1993J, SN 2008ax, and SN 2011dh, and in the models.

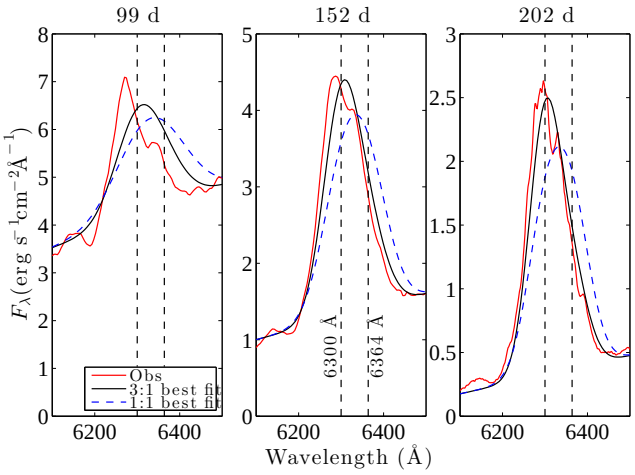

Fig. 13. The [O I] $\lambda\lambda$6300, 6364 feature in SN 2011dh (red) and the best double Gaussian fits assuming optically thin (3:1) emission (black solid line) and optically thick (1:1) emission (blue dashed line). The optically thin fits are superior at all times.

the [O I] $\lambda\lambda$6300, 6364 lines are driven by thermal collisions at all times, the [O I] λ5577/[O I] $\lambda\lambda$6300, 6364 ratio can serve as a thermometer for the oxygen region. Two effects complicate this simple diagnostic, however; at early times line blending and radiative transfer effects make it difficult to assess to true emissivities in the lines (Sect. 4.16), and at later times, when these complications abate, the [O I] λ5577 line falls out of LTE, which introduces an additional dependency on electron density.

Figure 14 shows the luminosity in [O I] λ5577 and the ratio [O I] λ5577/[O I] $\lambda\lambda$6300, 6364. It is noteworthy how similar the evolution of these line ratios are in the three SNe. Most of the models overproduce this ratio by a factor $\sim$ 2. Since both lines are driven by thermal collisions, one possible reason for this is that the oxygen-zone temperatures are too high in the models. This in turn must be caused by either a too close mixing between the gamma-ray emitting ^{56}Ni clumps and the oxygen clumps, or an underestimate in the cooling ability of the oxygen zone. The cooling efficiency has some dependency on the density of the oxygen clumps; a higher density leads to more frequent collisions, which increases the efficiency of collisional cooling, but a higher density also leads to higher radiative trapping, which reduces the efficiency of the cooling. Comparing models 13C and 13E, which only differ in contrast factor χ, model 13E (which has a higher χ and therefore a higher O-zone density) has a higher O/Ne/Mg zone temperature (6060 K vs 5860 K at 150 days), suggesting that the second effect dominates at this time. Apart from the temperature effect, a higher density also brings the [O I] λ5577 parent state closer to LTE (departure coefficient 0.8 instead of 0.5), and the combined effect is a higher [O I] λ5577/[O I] $\lambda\lambda$6300, 6364 line ratio (the parent state of [O I] λ6300, 6364 has a weaker Boltzmann factor due to its lower excitation energy, and is already in LTE in both scenarios). From this comparison, a high O-zone density is not favored by the [O I] λ5577/[O I] $\lambda\lambda$6300, 6364 line ratio. This is however not consistent with the constraints imposed by the fine structure analysis of the oxygen lines (E14b) and by magnesium recombination lines (Sect. 4.7). This analysis suggest that a too strong mixing between the ^{56}Ni clumps and the oxygen clumps is more likely to explain the [O I] λ5577/[O I] $\lambda\lambda$6300, 6364 line ratio discrepancy. We note, however, that also other factors, such as line blending, line blocking (see Sect. 4.16), and molecular cooling may affect the line ratio. As Fig. 23 shows, there is [Fe II] emission contaminating both [O I] λ5577 and [O I] $\lambda\lambda$6300, 6364 at

Table 5. Measurements of the [O I] λ5577 / [O I] $\lambda\lambda$6300, 6364 line ratio in SN 1993J, SN 2008ax, and SN 2011dh, the derived LTE temperature (assuming optically thin emission) and the thermally emitting O I mass (with the same assumptions). The error bars on the O I mass include the systematic uncertainties in distance and extinction.

Time (days)	Ratio	$T_{\mathrm{LTE},\tau<1}$ (K)	$M(\mathrm{O\,I})_{\mathrm{LTE},\tau<1}$ ($M_\odot$)
SN2011dh			
152	$0.16^{+0.02}_{-0.02}$	4700^{+100}_{-100}	$0.29^{+0.034}_{-0.027}$
SN2008ax			
143	$0.15^{+0.02}_{-0.02}$	4640^{+110}_{-120}	$0.76^{+0.30}_{-0.30}$
SN1993J			
172	$0.14^{+0.05}_{0.05}$	4590^{+270}_{-330}	$0.68^{+0.31}_{-0.31}$

100 days, and the discrepancy may be related to this line blending.

In Table 5 we report the LTE temperatures and O I masses derived from the [O I] λ5577 and [O I] $\lambda\lambda$6300, 6364 luminosities (using Eq. 3 in Jerkstrand et al. (2014)), assuming optically thin emission and no blending or blocking. From the spectral models we find an epoch of ∼150 days to be most relevant for the application of this method; before this time the lines are significantly blended and/or blocked, and at later times the [O I] λ5577 line starts to deviate strongly from LTE. That the oxygen masses determined with this method are roughly consistent with the ones inferred from the detailed modeling means that the factor ∼ 2 difference in the [O I] λ[5577]/[O I] $\lambda\lambda$6300, 6364 ratio between the observations and those models does not translate to any large differences in the derived oxygen mass.

4.5.3. Oxygen recombination lines

There are four recombination lines predicted to be detectable and which are also appear detected in the spectra of SN 2011dh : O I λ7774, O I λ9263, O I λ1.129 μm + O I λ1.130 μm and O I λ1.316 μm (Fig. 15, A.2)[7]. These are allowed transitions from high-lying states (excitation energies > 10 eV) which cannot be populated by thermal collisions. Inspection of the solutions for the non-thermal energy deposition channels shows that, at all epochs, at least ten times more energy goes into ionizing oxygen than exciting it. Emission lines from high-lying states are thus to a larger extent driven by recombination than by non-thermal excitations. This result was also obtained by a similar calculation by Maurer et al. (2010).

Letting ψ denote the fraction of the electrons provided by oxygen ionizations ($\psi = n_{\mathrm{OII}}/n_{\mathrm{e}}$), the recombination line luminosity is

$$L^{\mathrm{ul}}_{\mathrm{rec}} = \frac{4\pi}{3}\,(V_{\mathrm{core}}t)^3\, f_{\mathrm{O}}\psi n_{\mathrm{e}}^2 \alpha^{\mathrm{ul}}_{\mathrm{eff}} h\nu_{\mathrm{ul}}\,, \qquad (3)$$

where f_{O} is the oxygen zone filling factor, and u and l refer to the upper and lower levels. The factor ψ is close to unity at early times (as the electron fraction is of same order or greater than the fraction of other elements in the O zones), in our model range we find $\psi \approx 0.5$ between 100-200 days in the O/Ne/Mg zone. The effective recombination rates $\alpha^{\mathrm{ul}}_{\mathrm{eff}}$ are (for the purpose of the analytical formulae here) computed in the purely radiative limit (no collisional de-excitation), using Case B for the optical depths (see Appendix C for details). These are considered accurate as the recombination cascade of O I is well known (Nahar 1999).

[7] Note that O I λ8446 has a recombination emissivity similar to these four lines, but this flux scatters and/or blends into the Ca II $\lambda\lambda$8498, 8552, 8662 lines and is not directly observable.

We analyze the models for the amount of line blending and scattering that is present for each line. The presence of blending and scattering still allows a determination of an upper limit to the recombination luminosity in the line of interest, which from Eq. 3 translates to an upper limit for $f_{\mathrm{O}}n_{\mathrm{e}}^2$.

In our models, O I λ7774 is relatively uncontaminated between 100-500 days. It is optically thick up to ∼400 days. Pure recombination emission is thus present only after this time. O I λ9263 is at all times strongly blended with [Co II] λ9338 in particular, but also with S I $\lambda\lambda$9218, 9228, 9237 and Mg II $\lambda\lambda$9218, 9244. It becomes optically thin at ∼200 days. Pure recombination emission is never present. The O I λ1.129 + λ1.130 μm line has little contamination in the model at 100 and 150 days, but from 200 days and later [S I] λ1.311 μm contaminates. Na I $\lambda\lambda$1.138, 1.140 μm typically contributes ∼10%. The line becomes optically thin at ∼200 days. Pure recombination emission is never present. The O I λ1.316 μm line has little contamination in the model early on (Fig. A.2), but for $t \gtrsim 200$ days becomes overtaken by [Fe II] λ1.321 μm + [Fe II] 1.328 μm (Fig. A.4). It becomes optically thin at ∼200 days. Pure recombination emission is present between ∼ 150-200 days.

We use these considerations to derive either direct estimates (when pure recombination is indicated) or upper limits (when blending and/or scattering is indicated) of the quantity $n_{\mathrm{e}}f_{\mathrm{O}}^{1/2}$, presented in Table 6. All recombination lines give fairly consistent values of $n_{\mathrm{e}}f_{\mathrm{O}}^{1/2}$, which for $\psi = 0.5$ are $n_{\mathrm{e}}f_{\mathrm{O}}^{1/2} \sim 3\times10^8$ cm^{-3} at 100 days, and $n_{\mathrm{e}}f_{\mathrm{O}}^{1/2} \sim 3\times10^7$ cm^{-3} at 200 days.

The quantity $n_{\mathrm{e}}f_{\mathrm{O}}^{1/2}$ does not have any strong dependence on f_{O}; doubling the volume (i.e. halving f_{O}) leads to (approximately) a factor two reduction of ionization rates per unit volume, which under the steady-state constraint must lead to a factor two reduction of the recombination rates per unit volume ($n_{\mathrm{e}}n_+\alpha$) as well. If ψ stays constant, this means a factor two reduction in n_{e}^2, i.e. a factor $2^{1/2}$ reduction in n_{e}, and $n_{\mathrm{e}}f_{\mathrm{O}}^{1/2}$ stays constant. This is confirmed by comparing models 13C and 13E with respect to the oxygen recombination lines - their luminosities are similar despite a factor 5 different densities (Fig. 15). The low density model has (for the O/Ne/Mg zone) $f = 0.13$ and $n_{\mathrm{e}} = 6\times10^7$ cm^{-3} so $n_{\mathrm{e}}f^{1/2} = 2.2\times10^7$ cm^{-3}. The high density model has $f = 0.026$, $n_{\mathrm{e}} = 1.5\times10^8$ cm^{-3}, so $n_{\mathrm{e}}f^{1/2} = 2.4\times10^7$ cm^{-3}.

From Figs. 1 and 2, model 12C does a good reproduction of O I λ7774 and O I λ9263 at 100 days, but underproduces O I λ7774, O I λ1.129 μm + λ1.130 μm and O I λ1.316 μm at 200 days. At this time, the O/Ne/Mg zone has $n_{\mathrm{e}}f^{1/2} = 1.5\times10^7$ cm^{-3}. The O/Si/S and O/C zones have similar values and the total $n_{\mathrm{e}}f^{1/2}$ value is therefore close to the required $\sim 3\times10^7$ cm^{-3}, so from Eq. 3 we would expect the recombination lines to be well reproduced. The reason for the discrepancy lies in the ψ factor. Closer inspection of the ionization balance at 200 days shows that the O II ions in the O/Si/S and O/C zones are completely neutralized by charge transfer with Si I, S I, and C I, and $\psi \approx 0$ in these zones. The ion pools in these zones instead consist of Mg II, Si II, and S II (O/Si/S zone) and C II and Mg II (O/C zone). If these charge transfer reactions are overestimated, the recombination lines from O I become underestimated.

The critical charge transfer reactions are O II + Si I, O II + S I, O II + C I, and O II + Mg I, as all other species in the oxygen zones are too rare to affect the pool of oxygen ions. To our knowledge, no published calculations for these rates exist. We use fast reactions rates of 10^{-9} cm^3 s^{-1} for the first three, and a small reaction rate for the last - these are based only on the presence or absence of transitions with typical resonance val-

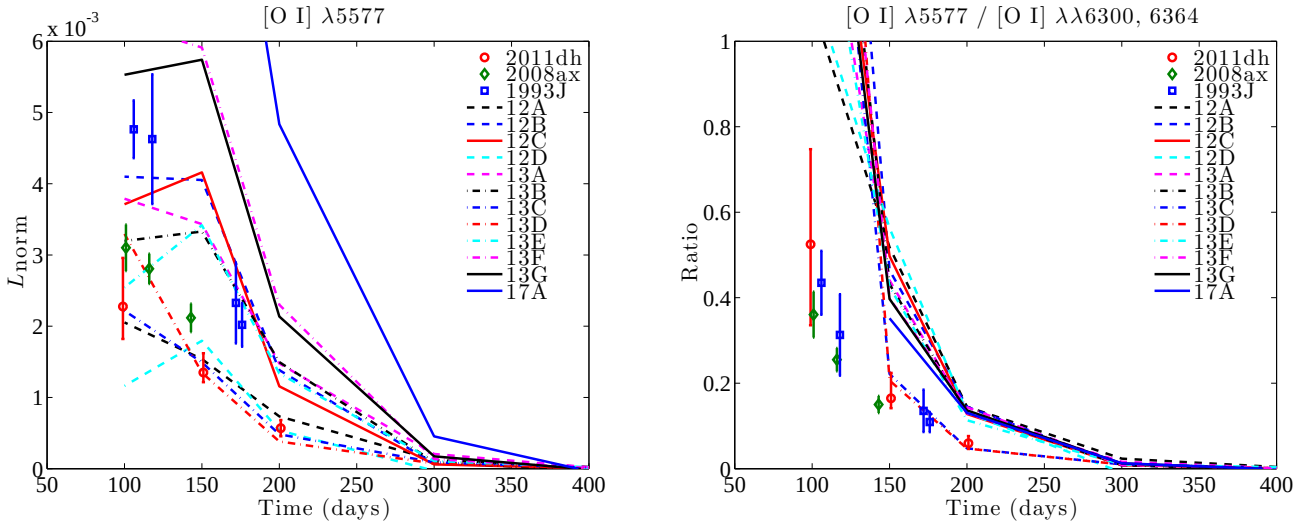

Fig. 14. Left : The luminosity in [O I] λ5577 relative to the ^{56}Co decay power in the models and in SN 1993J, SN 2008ax, and SN 2011dh. Right: The [O I] λ5577 / [O I] $\lambda\lambda$6300, 6364 line ratio.

ues (Rutherford et al. 1971; Pequignot & Aldrovandi 1986). The uncertainty in the rates above affect the oxygen ionization balance mainly in the O/Si/S and O/C zones, which are rich in Si, S and C, respectively. Little Mg I exists in the O/Ne/Mg zone since magnesium is heavily photoionized. Since the O/Si/S and O/C zones contain about 2/3 of the oxygen mass in low M_{ZAMS} models, there is thus a factor ~ 3 uncertainty in the O I recombination line luminosities introduced by the uncertainty in these rates. This is roughly the underproduction of the O I recombination lines in 12 $M_\odot$ models at 200 days, and we therefore do not consider this discrepancy to be critical. At higher ZAMS mass, the fraction of the oxygen that resides in the O/Ne/Mg zone increases, and this reduces the uncertainty in the "effective" ψ (which mainly comes from the O/Si/S and O/C zones).

Charge transfer also break the independency of $n_e^2 V_O$ with f_O, because charge transfer neutralization of O II operates more efficiently at high densities when there are more neutral Si, S and C available per oxygen ion. Looking again at models 13C and 13E, the O II density (in the O/Ne/Mg zone) changes from $n_{OII} = 4.7{\times}10^7$ cm^{-3} in the low-density model to $n_{OII} = 7.3{\times}10^7$ cm^{-3} in the high density model (factor 1.6). Whereas n_e goes up by a factor 2.5 ($\approx \sqrt{5}$), n_{OII} goes up only by a factor 1.6, as charge transfer neutralization of O II is more efficient in the high-density case. The result is that, past some threshold, O I recombination lines can become weaker with increasing density.

4.6. Sodium lines

Sodium has only one detectable line throughout the optical/NIR region; the Na I D doublet (Fig. A.2). Even small amounts of Na I can produce optically thick D-lines throughout a SN nebula for a long time, giving a strong P-Cygni component. Any He I λ5876 emission would scatter in these optically thick D-lines. In model 12C, the Na I D lines are optically thick throughout most of the helium envelope over the whole 100-500 day interval. The optical depths in fact increase with time as the neutral fraction of sodium grows faster than t^2, the rate at which the Sobolev optical depths decrease with time for a constant number of atoms. For example, the neutral fraction of sodium in the outermost He shell is 1.3×10^{-5} at 100 days and 2.7×10^{-3} at 500 days, a 200-fold increase compared to a factor 25 drop in t^{-2} term. The exact location in the helium envelope where the Na I lines become optically thin goes from 7500 km s^{-1} at 100 days to 9400 km s^{-1} at 500 days. As the lines are optically thin in the H envelope, this produces a distinct absorption trough from ~ 5890 Å $\times \left(1 - 9000/3 \times 10^5\right) = 5700$ Å which is clearly seen in both modelled and observed spectra (Fig. 1, 22). Note however that emission lines from the helium envelope itself (e.g. [N II] λ5754) is less efficiently blocked than emission lines from the core, as these have to pass through a smaller velocity range of blocking Na I atoms.

On top of the P-Cygni component is a component from the O/Ne/Mg zone, where most of the synthesized sodium resides and emits recombination and cooling emission. In the 12 and 13 $M_\odot$ models, this emission component is relatively weak, making up about 25−50% of the total luminosity in the line. In the 17 $M_\odot$ model, however, this component is stronger than the scattering component.

4.7. Magnesium lines

The solar Mg abundance is log N = 7.60 ± 0.04 (Asplund et al. 2009), making the solar Mg/O ratio (by number) n(Mg)/n(O) = 0.081 ± 0.012, or equivalently Mg/O = 0.12 ± 0.018 by mass. The WH07 models produce a factor two lower ratio (Mg/O = 0.05 – 0.09, see Table 2). As galactic nucleosynthesis of oxygen and magnesium should be dominated by massive stars (Timmes et al. 1995), this difference will persist in galactic chemical evolution models.

From this perspective it is interesting to see what constraints SNe with distinct oxygen and magnesium emission lines, such as Type IIb SNe, can provide on the relative Mg/O production in individual stars. We begin by considering line formation of Mg I] λ4571. The relative contributions of collisional excitation and recombination for populating 3p(^{3}P) (the parent state of Mg I] λ4571) is (letting u and l denote the upper and lower states 3p(^{3}P) and 3s^2(^{1}S), respectively, and making the approximation that most Mg I atoms in the ground state, the ratio between the collisional and recombination populating rates are

$$\frac{R_{\rm coll}}{R_{\rm rec}} = \frac{n_{\rm MgI} n_{\rm e} 8.629 \times 10^{-6} T^{-1/2} \Upsilon_{\rm ul}(T) g_{\rm l}^{-1} e^{-(E_{\rm u}-E_{\rm l})/kT}}{\alpha_{\rm eff}^{3p(^3P)}(T) n_{\rm MgII} n_{\rm e}}$$

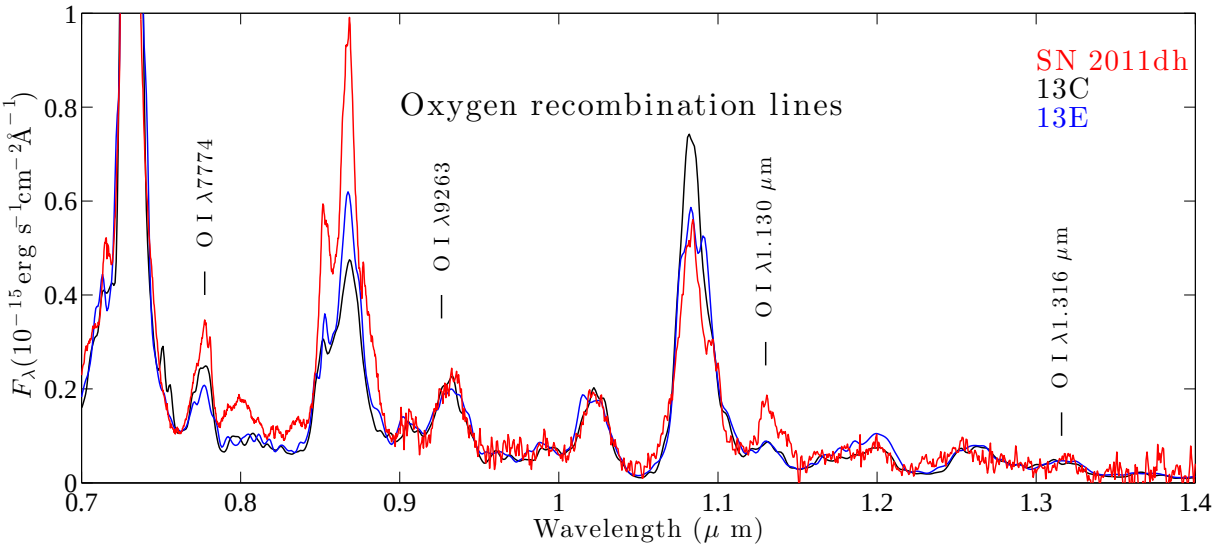

Fig. 15. Models with low (13C, black) and high (13E, blue) density in the oxygen region show similar O I recombination line luminosities, here at 200 days. Observed spectrum of SN 2011dh (optical part : 202 days, NIR part 198 days) in red (dereddened and redshift corrected).

Table 6. Measured luminosities of the O I recombination lines of SN 2011dh at 99 and 198/202 days, and the corresponding $n_e f_O^{1/2}$ factors derived from Eq. 3, using effective recombination coefficients $\alpha_{\rm eff}^{7774} = 1.6\times10^{-13}$ cm^3 s^{-1}, $\alpha_{\rm eff}^{9263} = 6.4\times10^{-14}$ cm^3 s^{-1}, $\alpha_{\rm eff}^{1.129+1.130} = 1.1\times10^{-13}$ cm^3 s^{-1}, $\alpha_{\rm eff}^{1.316} = 2.6\times10^{-14}$ cm^3 s^{-1} (Appendix C), and $\psi = 0.5$. Where the model calculations suggest line blending or scattering contributions, we add a $\lesssim$ symbol.

Time (days)	$L_{7774}(n_e^{7774} f_O^{1/2})$ (erg s^{-1}(cm^{-3}))	$L_{9263}(n_e^{9263} f_O^{1/2})$ (erg s^{-1}(cm^{-3}))	$L_{1.129+1.130}(n_e^{1.129+1.130} f_O^{1/2})$ (erg s^{-1}(cm^{-3}))	$L_{1.316}(n_e^{1.316} f_O^{1/2})$ (erg s^{-1}(cm^{-3}))
99	2.0×10^{39} ($\lesssim 3.0\times10^{8}$)	1.1×10^{39}($\lesssim 3.8\times10^{8}$)	...	...
198/202	2.0×10^{38} ($\lesssim 3.3\times10^{7}$)	1.1×10^{38} ($\lesssim 4.1\times10^{7}$)	1.0×10^{38} ($\lesssim 3.4\times10^{7}$)	3.0×10^{37} (4.1×10^{7})

$$= \left(\frac{x_{\rm MgI}}{1.1\times10^{-3}}\right)\times\exp\left[\frac{-(E_{\rm u}-E_{\rm l})}{k}\left(\frac{1}{T}-\frac{1}{5000}\right)\right] \qquad (4)$$

where $n_{\rm MgI}$, $n_{\rm MgII}$, $n_{\rm e}$ are the number densities of Mg I atoms, Mg II ions, and electrons, $g_{\rm l}$ is the statistical weight of the lower level (=1), $E_{\rm u}-E_{\rm l}$ is the energy difference between the upper and lower states (2.71 eV), $\Upsilon_{\rm ul}(T)$ is the velocity-averaged collision strength (we use a value $\Upsilon_{\rm ul}(T) = 1.95\,(T/5000\ K)^{1/2}$ which is a fit to values in (Mauas et al. 1988)), $\alpha_{\rm eff}^{\rm 3p(3P)}$ is the effective recombination rate to 3p(^{3}P) (we compute a value 5×10^{-13} cm^3 s^{-1} in Appendix B.2), and $x_{\rm MgI} = n_{\rm MgI}/n_{\rm MgII}$ is the ratio of neutral to ionized magnesium. In the models, the ionization balance of magnesium is controlled by the radiation field as photoionization rates are typically $\sim 10^3$ times higher than the non-thermal ionization rates for Mg I. The radiation field is strong enough to leave almost all magnesium in the Mg II state throughout the nebular phase, so $x_{\rm MgI} \ll 1$, with $x_{\rm MgI} = 10^{-3}$ being a typical value. This means that $R_{\rm coll}/R_{\rm rec}$ is close to unity, and the Mg I] λ4571 emissivity is sensitive to the exact value of $x_{\rm MgI}$.

Figure 16 shows the regimes in $\left[x_{\rm MgI}, T\right]$ space where collisional excitation and recombination dominate, respectively (the line corresponds to $R_{\rm coll}/R_{\rm rec} = 1$). The evolution of $x_{\rm MgI}$ and T in the O/Ne/Mg zones of models 13C and 13E are also plotted, showing that physical conditions are close to the dividing lines between the regimes, and in general both processes could be important. With time, the neutral fraction $x_{\rm MgI}$ increases in the models (which increases the $R_{\rm coll}/R_{\rm rec}$ ratio), and the temperature decreases (which decreases the $R_{\rm coll}/R_{\rm rec}$ ratio). The effects roughly cancel out so that the $R_{\rm coll}/R_{\rm rec}$ ratio evolves relatively little over the 100-500 day period. Note how the higher density model (13E) is initially hotter and have a lower $x_{\rm MgI}$ value than the lower density model (13C), but at later times is cooler and with more neutral magnesium. This difference likely arises due to the important of radiative trapping at early times.

All other Mg I lines come from high lying states that are more difficult to populate by collisional excitation, and will form mainly through recombinations. Some empirical verification for this can be found by considering the relative line luminosities of Mg I λ1.183 μm and Mg I λ1.504 μm. The Mg I 1.183 μm line arises from a lower level than Mg I λ1.504 μm and has a larger collision strength relative to the ground state; consequently collisional excitation should lead to a higher luminosity than in Mg I 1.504 μm (both lines are allowed transitions to excited states and are thus de-excited by spontaneous radiative decay). But the observed feature at 1.183 μm in SN 2011dh is significantly weaker (not even clearly detected) than the 1.504 μm feature (Fig. 2), which cannot be achieved in a collisional excitation scenario. The dominance of Mg I] λ4571 and Mg I λ1.504 μm in the observed spectra of these SNe is instead naturally explained in a recombination scenario, since these lines arise from triplet states which generally take most of the recombinations, whereas Mg I λ1.183 μm (as well as Mg I λ8806) arise from singlet states. The situation is analogous to the ratio of triplet to singlet recombination channels in He I, where $\sim 3/4$ of all recombinations go to the triplet ladder and $\sim 1/4$ to the singlet ladder (e.g. Benjamin et al. 1999). Two other lines in the triplet cascade that should be reasonably strong are Mg I $\lambda\lambda$5167, 5172, 5183 and Mg I λ1.577

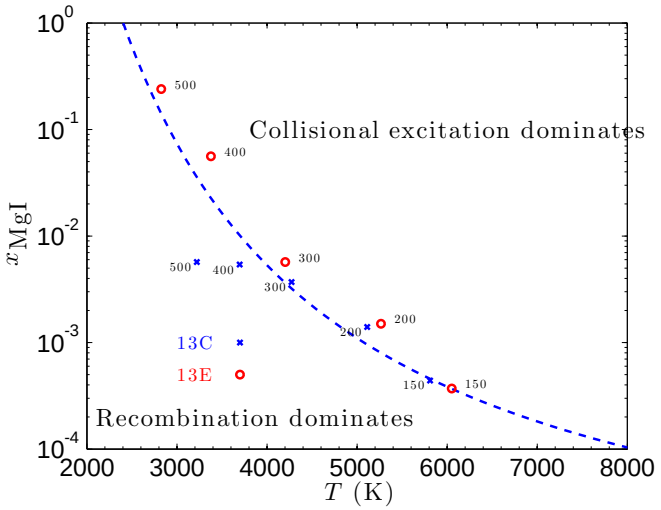

Fig. 16. The regimes of Mg I] λ4571 line formation in the [$x_{\rm MgI}$, T] plane. The values as function of time for models 13C (blue crosses) and 13E (red circles) are also shown. The proximity to the dividing line between the two regimes means that both recombination and collisional excitation may contribute to the Mg I] λ4571 luminosity.

μm, but they are both predicted to be too weak to be clearly discerned in the spectra.

Having established that the nebular Mg I lines likely arise by recombination, with collisional excitation making some uncertain contribution to Mg I] λ4571, we can attempt an understanding of their luminosities. The critical density $n^{4571}_{\rm e,crit}$ (above which collisional de-excitation is important) for Mg I] λ4571 (at 5000 K) is found from equating the collisional and radiative de-excitation rates

$$n^{4571}_{\rm e,crit} 8.629\times10^{-6} T^{-1/2} \frac{\Upsilon_{4571}}{g_{\rm u}} = A_{4571}\beta_{4571} \quad (5)$$

where β_{4571} is the escape probability. With $A_{4571} = 217$ s^{-1}, $T = 5000$ K, $g_{\rm u} = 9$, and previously specified values for other quantities, $n^{4571}_{\rm e,crit} = 8\times10^9\beta_{4571}$ cm^{-3}. We find in our models that the optical depth of the Mg I] λ4571 line is of order unity in the nebular phase, so $\beta_{4571} \gtrsim 0.1$ and $n^{4571}_{\rm e,crit} \gtrsim 10^9$ cm^{-3}. This is always higher than the electron density in the oxygen/magnesium zone in our models, so collisional de-excitation is unimportant and most populations of 3p(^{3}P) will lead to emission of a 4571 Å photon. We can therefore write the luminosity of the Mg I] λ4571 line (assuming that recombination dominates and using the result that $x_{\rm MgI} \ll 1$) as

$$L_{4571} = 1.1\times10^{40}\left(\frac{M_{\rm Mg}}{1\ M_\odot}\right)\left(\frac{n_{\rm e}}{10^8\ {\rm cm^{-3}}}\right)\times \left(\frac{\alpha^{\rm 3p(3P)}_{\rm eff}}{5\times10^{-13}\ {\rm cm^3\ s^{-1}}}\right) p^{\rm esc}_{4571}\ {\rm erg\ s^{-1}} \quad (6)$$

where $p^{\rm esc}_{4571}$ is the escape probability for the photon to pass through the SN ejecta without being absorbed by line blocking by other elements. The model calculations show that $p^{\rm esc}_{4571}$ can be significantly smaller than unity far into the nebular phase (Sect. 4.16). For given $M_{\rm Mg}$ and $p^{\rm esc}_{4571}$, a higher electron density gives higher Mg I] λ4571 emissivity, so higher density of the magnesium clumps favors brighter emission lines (up to the limit when the critical density is reached or when $x_{\rm MgI} \ll 1$ is no longer fulfilled).

The other distinct Mg I line observed is Mg I λ1.504 μm (Figs. 2, 3). There is no strong blending of this line with any other lines in the models, and it has therefore good diagnostic potential for the magnesium mass in the ejecta. Having a much higher critical density than Mg I] λ4571 (as it is an allowed transition to an excited lower level) and suffering no significant line blocking in the NIR, its luminosity should be well approximated by

$$L_{1.504\ \mu m} = 6.6\times10^{38}\left(\frac{M_{\rm Mg}}{1\ M_\odot}\right)\left(\frac{n_{\rm e}}{10^8\ {\rm cm^{-3}}}\right)\times \left(\frac{\alpha^{\rm 4p(^3P)}_{\rm eff}}{1\times10^{-13}\ {\rm cm^3\ s^{-1}}}\right) {\rm erg\ s^{-1}}\ . \quad (7)$$

In Appendix B.2 we compute the effective recombination coefficient $\alpha^{\rm 4p(^3P)}_{\rm eff}$ in both Case B and Case C at various temperatures. The physical conditions in the models at 200 days is close to Case C and $T \sim 5000$ K, for which $\alpha^{\rm 4p(^3P)}_{\rm eff} \approx 1\times10^{-13}$ cm^3 s^{-1}. Note that also the Mg I λ1.148 μm recombination line will blend with Mg I λ1.504 μm, but we find this contribution to be $\lesssim 10\%$ and is ignored here.

Table 7 shows the measured luminosities in Mg I] λ4571 and Mg I λ1.504 μm in SN 2011dh, and the corresponding quantities $n_{\rm e}M_{\rm Mg}$ derived from Eqs. 6 and 7. We see that at 200 days the Mg I λ1.504 μm line gives an order of magnitude higher $n_{\rm e}M_{\rm Mg}$ value than the Mg I] λ4571 line does, if $p^{\rm esc}_{4571}$ would be zero. Contribution by collisional excitation to Mg I λ4571 only exacerbates this difference. This suggests that $p^{\rm esc}_{4571} \ll 1$, as the observed blueshift of the Mg I] λ4571 line also suggests (the peak of the line is blueshifted by 1300 km s^{-1} at 200 days, see Fig. 17). The Mg I λ1.504 μm line shows no blueshift, likely as there is much less line opacity in the NIR compared to the optical. If $p^{\rm esc}_{4571}$ ~0.1 at 200 days, the derived $n_{\rm e}M_{\rm Mg}$ values agree. As shown in Sect. 4.16, this is a typical value obtained when explicitly computing the line blocking opacity. The expected blueshift for a uniform sphere with a smooth radial opacity τ is $\Delta V/V = -1 + \ln(1+\tau)/\tau$ (Lucy et al. 1991), which has a value $\Delta V/V = -0.45$ for $\tau = 2$ ($e^{-2} \sim 0.1$). This matches the observed blueshift of Mg I] λ4571 (ΔV ~1300 km s^{-1}) if $V \sim 3000$ km s^{-1}, in good agreement with the observed line widths [8].

The blueshift of Mg I] λ4571 gradually disappears with time in SN 2011dh (Fig. 17) (as also obtained in the line blocking scenario, Sect. 4.16), reaching $\Delta V < 400$ km s^{-1} at 400 days. The shift at 400 days requires $\tau \lesssim 0.3$ from the Lucy formula, and so the $n_{\rm e}M_{\rm Mg}$ values derived from the Mg I] λ4571 line listed in Table 7 at these epochs should be close to the true ones. Figure 18 shows how the Mg I] λ4571 line profile evolves in model 13E (chosen for having distinct Mg lines and no dust) between 200 days (where there is significant line blocking) and 300 days (where most line blocking is gone). The total line profile is, as for the O I lines, affected in a complex way by both line blocking from the receding side and from blending with other emission lines.

4.7.1. The magnesium mass in SN 2011dh

The optical to NIR spectral coverage at 200 days of SN 2011dh allows us to combine the constraints from the oxygen and

[8] Note that the use of formulae for continuous opacities is only strictly applicable if the line opacity is made up by a large number of equally spaced and equally strong lines, so its use here is only for rough estimates of the line blocking effect.

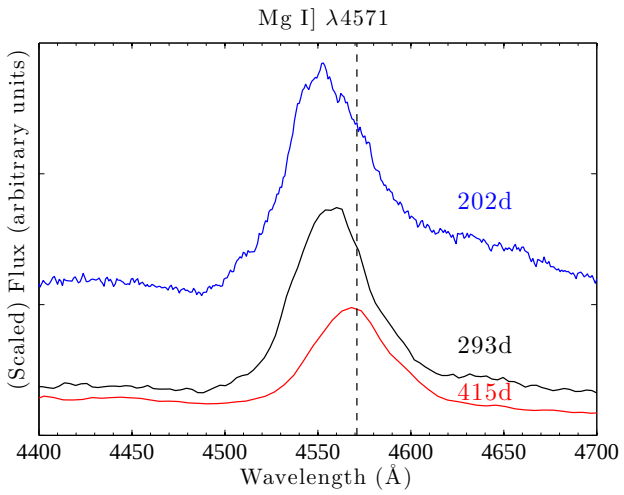

Fig. 17. The Mg I] λ4571 feature in SN 2011dh. The line peak shows a blueshift of 1300 km s^{-1} at 200 days, which gradually diminishes and is smaller than 400 km s^{-1} at 415 days.

Table 7. Measured luminosities of Mg I] λ4571 and Mg I λ1.504 μm in SN 2011dh, and the corresponding quantities $n_e\left(M_{Mg}/M_\odot\right)$ from Eq. 6 and 7. We have here used effective recombination rates of $\alpha_{eff}^{4571} = 5\times10^{-13}$ cm^{-3} and $\alpha_{eff}^{1.504} = 1\times10^{-13}$ cm^{-3}. Since collisional excitation may contribute to the Mg I] λ4571 luminosity, we add a $\lesssim$ symbol to the derived $n_e\left(\frac{M_{Mg}}{M_\odot}\right)p_{4571}^{esc}$ factor.

Time (days)	$L_{4571}\left(n_e\left(\frac{M_{Mg}}{M_\odot}\right)p_{4571}^{esc}\right)$ (erg s^{-1})(cm^{-3})	$L_{1.504\ \mu m}\left(n_e\left(\frac{M_{Mg}}{M_\odot}\right)\right)$ (erg s^{-1})(cm^{-3})
202/206	2.8×10^{38} $\left(\lesssim 2.5\times10^{6}\right)$	9.7×10^{37} $\left(1.5\times10^{7}\right)$
239	2.2×10^{38} $\left(\lesssim 2.0\times10^{6}\right)$	...
293	1.7×10^{38} $\left(\lesssim 1.5\times10^{6}\right)$	...
359	6.7×10^{37} $\left(\lesssim 6.1\times10^{5}\right)$	...
415	2.7×10^{37} $\left(\lesssim 2.5\times10^{5}\right)$	...

magnesium recombination lines to eliminate dependencies on the electron number density. From the oxygen recombination lines (Sect. 4.5) we have (estimating a 30% error) $n_e f_O^{1/2} = (3\pm1)\times10^7$ cm^{-3}, and from the Mg I λ1.504 μm line we have (estimating a similar error) $n_e\left(M_{Mg}/M_\odot\right) = (1.5\pm0.5)\times10^7$ cm^{-3}. Combining these we obtain a constraint $M_{Mg} = (0.50\pm0.24)\,f_O^{1/2}$ M$_\odot$. This range is plotted in Fig. 20. For a filling factor $f_O = 10^{-2}$, a magnesium mass of $\sim$0.05 M$_\odot$ is thus needed to reproduce the observed Mg I λ1.504 μm recombination line, whereas for $f_O = 0.1$ a mass $\sim$0.15 M$_\odot$ is needed. A formal limit can be stated if we take the $f_O \gtrsim 10^{-2}$ constraint needed to make the [O I] $\lambda\lambda$6300, 6364 lines optically thin early enough (Sect. 4.5, and allowing for a factor 2 margin), and $f_O < 0.07$ from the fine-structure analysis in E14b, giving $0.026\,M_\odot < M_{Mg} < 0.19\,M_\odot$. If we take the oxygen mass to have been constrained to 0.3 – 0.5 M$_\odot$ (from the acceptable fits of the [O I] $\lambda\lambda$6300, 6364 line luminosites, Fig. 12), the Mg/O mass ratio falls in the 0.05 – 0.6 range, or Mg/O = (0.4 – 5) (Mg/O)$_\odot$. Thus, this analysis gives a Mg and O production in SN 2011dh consistent with the solar ratio, but with relatively large error bars. The Mg/O $\sim$ 1/2 (Mg/O)$_\odot$ production in the WH07 models is difficult to reconcile with SN 2011dh, lying at the edge of the tolerance interval.

Figure 19 shows Mg I] λ4571 and Mg I λ1.504 μm line luminosities in the observed spectra and in the models. Inspection of the model spectra shows that the Mg I] λ4571 line is often blended and/or has a very strongly varying continuum (see e.g. Fig. 1). Before 300 days these effects are generally so large that the line luminosity extraction algorithm does not give any meaningful estimates for the line luminosity, and we therefore do not plot these. After 300 days these effects are less severe, but still sometimes significant in some of the models.

With these caveats in mind, the general trend from the Mg I] λ4571 and Mg I λ1.504 μm lines is an underproduction by the models. From the analysis above, there are likely two contributing factors to this - the factor $\sim$2 underproduction of magnesium in the KEPLER models relative to the solar value, and too large filling factors f_O assumed for the O/Ne/Mg zone in the models. The strong impact of the filling factor is illustrated by comparing model 13C (large filling factor, $f_O = 0.32$) and model 13E (lower filling factor, $f_O = 0.061$) tracks. The Mg I λ1.504 μm line depends mostly on the density, and is a factor 2-4 stronger i model 13E. The Mg mass is 0.043 M$_\odot$ in these models. From the relationship between Mg mass and filling factor derived above, we would need $f_O \approx 0.01$ to reproduce the Mg I λ1.504 μm line.

An even larger difference between 13C and 13E is seen with respect to Mg I] λ4571. Whereas 13E underproduces Mg I λ1.504 μm, it overproduces Mg I] 4571 at late times. Figure 16 shows that model 13E is in the regime of collisional pumping of Mg I] λ4571 at all times, whereas model 13E moves into the recombination regime after $\sim$300 days. The growing difference in Mg I] λ4571 luminosities between 13C and 13E is thus due to the removal of collisional excitation contribution in the 13C model with time. In model 13E, Mg I] λ4571 does 5-10% of the cooling of the O/Ne/Mg zone throughout 100-500 days, whereas in 13C its cooling fraction is $\sim$3% up to 300 days and then drops to to <1%.

4.8. Silicon lines

Figure A.3 (middle) shows the contribution by Si I to the model spectrum (higher ions produce negligible emission). The detectable lines are [Si I] λ1.099 μm, Si I λ1.200 μm, and [Si I] $\lambda\lambda$1.607, 1.646 μm. No detectable optical lines are predicted. The emission comes from the explosively synthesized silicon in the Si/S and the O/Si/S zones.

The [Si I] λ1.099 μm line blends with the red wing of [S I] λ1.082 μm + He I λ1.083 μm and is difficult to observationally disentangle. The [Si I] λ1.200 μm line appears to be seen in the observed spectra (Fig. 2, 3). There is also a distinct line seen around 1.64 μm (Fig. 2), the model gives at this epoch about equal contributions from [Si I] λ1.646 μm and [Fe II] λ1.644 μm to this feature.

4.9. Sulphur lines

Figure A.3 (bottom) shows the contribution by S I and S II to the model spectrum (higher ions produce negligible emission). The sulphur lines arise from explosively made sulphur in the Si/S and O/Si/S zones (Fig. A.6). The only lines predicted to be strong are [S I] $\lambda\lambda$1.082, 1.131 μm (the 1.082 μm line can be as strong as He I λ1.083 μm at late times). S I 9213 Å causes some blending with O I λ9263 at early times. At late times [S I] λ1.131 μm is stronger than O I λ1.129 + λ1.130 μm. Note also [S II] $\lambda\lambda$10336, 10370. No detectable optical lines are predicted.

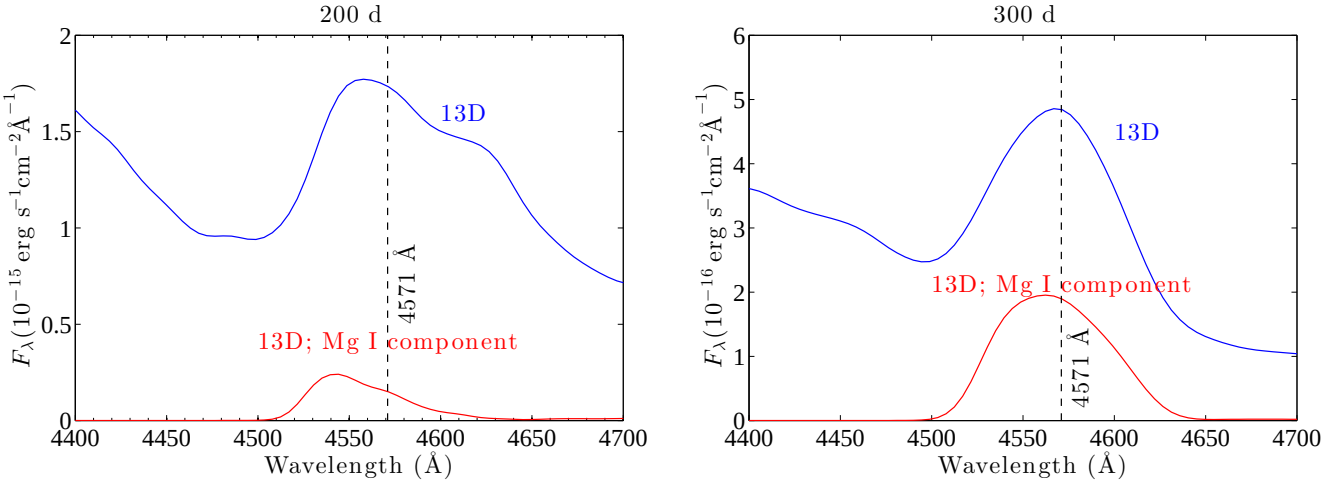

Fig. 18. Zoom-in on Mg I] λ4571 in model 13E (blue) at 200 (left) and 300 (right) days. The total flux is in blue, the contribution by Mg I in red. At 200 days there is significant line blocking of the red side of the Mg I emission (as well as a blend with some iron-group line emission). At 300 days both the line blocking and blending have abated.

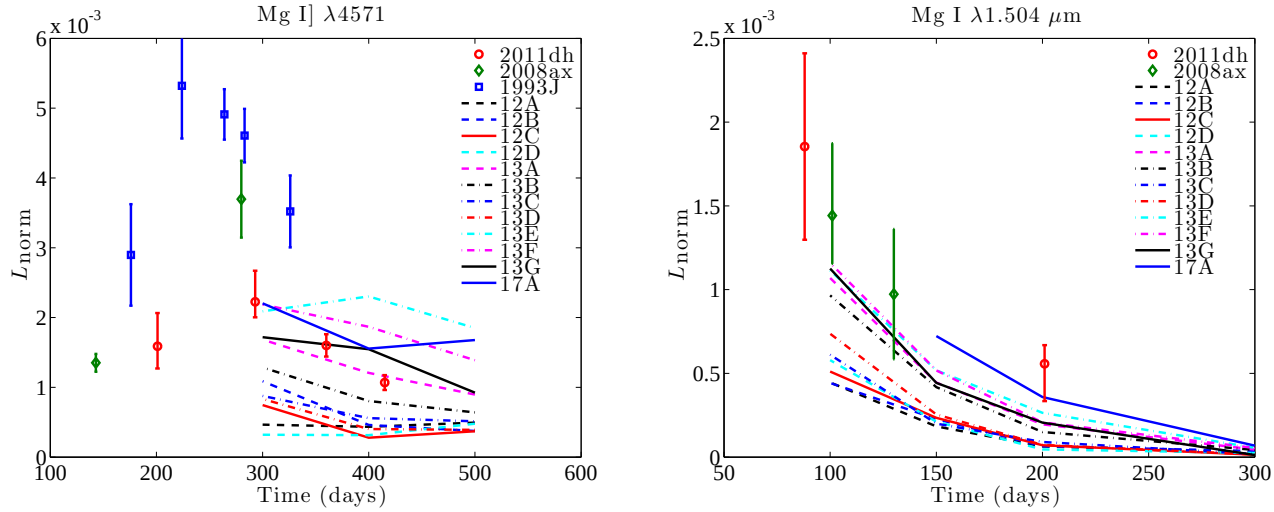

Fig. 19. The luminosity in Mg I] λ4571 (left) and Mg I λ1.504 μm (right) relative to the ^{56}Co decay power in SN 1993J, SN 2008ax, and SN 2011dh, and in the models. The Mg I] λ4571 line is typically very blended in the models before 300 days, we therefore do not plot the output of the line extraction algorithm before this time.

4.10. Calcium lines

Most of the calcium nucleosynthesis in SNe occurs in explosive oxygen burning, producing a Si/S zone that contains a few percent calcium by mass. In hydrogen-rich SNe this calcium is not visible as it is overwhelmed by emission from primordial calcium in the hydrogen envelope (Li & McCray 1993). Here, we find that in SN ejecta without such an envelope, the [Ca II] $\lambda\lambda$7291, 7323 emission comes indeed from the newly synthesized calcium. Calcium is not as prominent a cooler of the He envelope as the H envelope, as the radiation field here is harder, ionizing most of the calcium to Ca III in the nebular phase. After ~500 days, however, photoionization rates have dropped enough that Ca II starts forming in the He envelope, and eventually takes over from the calcium in the Si/S clumps in producing the [Ca II] $\lambda\lambda$7291, 7323 emission lines.

Figure 21 shows the observed and modelled [Ca II] $\lambda\lambda$7291, 7323 and Ca II $\lambda\lambda$8498, 8542, 8662 lines. In model 12C, the fraction of the cooling of the Si/S zone that is done by Ca II (and mainly [Ca II] $\lambda\lambda$7291, 7323) is 100%, 83%, 67%, and 42% at 100, 200, 300 and 400 days, respectively. We are thus in a regime where the cooling of the Si/S zone is dominated by Ca II, and the Ca II luminosity is therefore not particularly sensitive to the Ca II mass, but rather depends on the amount of gamma-ray and positron energy being reprocessed by the Si/Si zone, which in turn depends on the mass of the Si/S zone. The satisfactory agreement between observed and modelled Ca II lines (Fig. 21) thus supports the mass of the explosive oxygen burning ashes in the models used; 0.06 - 0.1 $M_\odot$.

We find that most of the Ca II $\lambda\lambda$8498, 8542, 8662 emission does not originate from the calcium in the Si/S zone; this zone is generally too cool ($T < 3000$ K after 200 days) to excite the 4p(^{2}P) parent state. They instead arise primarily by fluorescence following absorption in the H&K lines by Ca II in the Fe/Co/He clumps as well as in the helium envelope. The radiative de-excitation rate for the return transition in H&K is $A^{\rm eff}_{\rm HK} = 1.5 \times 10^8 \beta_{\rm HK}$ s^{-1}, and for the IR channel $A^{\rm eff}_{\rm IR} = 1.1 \times 10^7 \beta_{\rm IR}$ s^{-1}. The optical depth in the IR channel is always smaller than

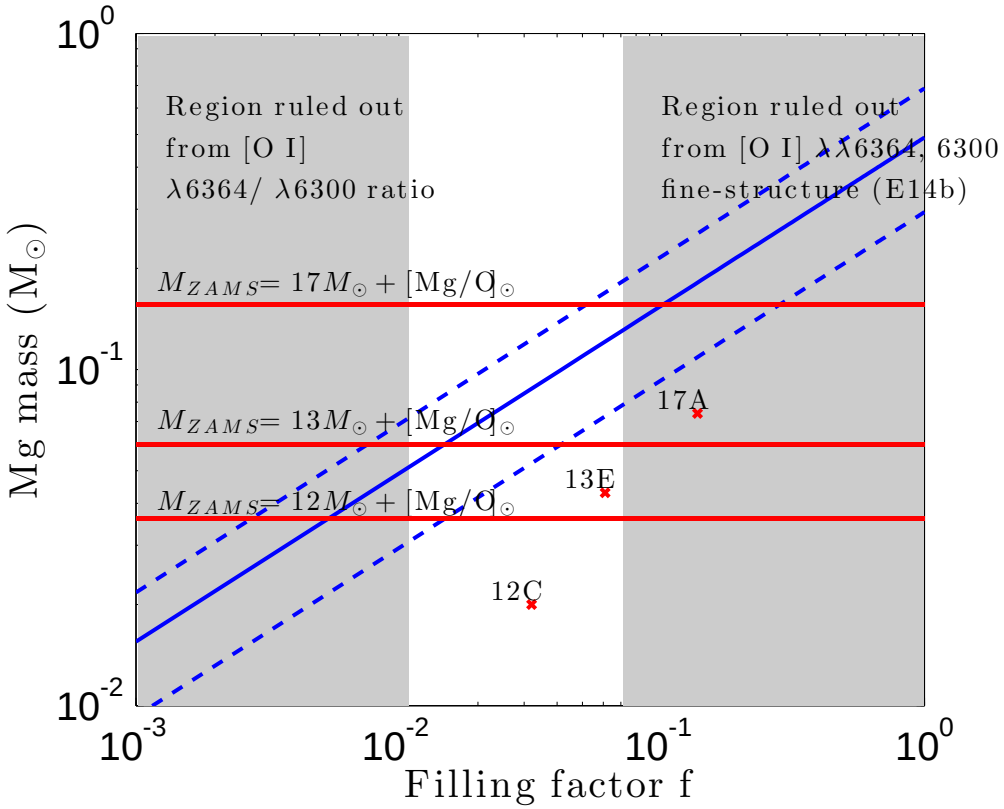

Fig. 20. The relationship between magnesium mass and oxygen zone filling factor derived from the oxygen and magnesium (Mg I λ1.504 μm) recombination lines in SN 2011dh (the solid blue line is best estimate and the dashed blue lines show the error bars). The $M_{\rm Mg}$-f combinations of some models are shown as red crosses. Also shown (as red solid lines) are the magnesium masses corresponding to a solar Mg/O ratio for the O masses for different $M_{\rm ZAMS}$ from WH07. The Mg/O ratio in the models is about half the solar Mg/O ratio. The regions ruled out by constraints from the [O I] $\lambda\lambda$6300, 6364 lines are shaded gray.

in the H&K channel, as the IR transitions go to the excited state 3d(^{2}D) which always has a much smaller population than the ground state. Since also $\beta_{\rm H\&K} << 1$ in the Fe/Co/He zone at all times, the result it that $A^{\rm eff}_{\rm IR} > A^{\rm eff}_{\rm HK}$, and most H&K absorptions in the Fe/Co/Ni zone are followed by fluorescence in the IR lines. In the helium and hydrogen envelopes, on the other hand, the density is low enough that significant de-excitation occurs back in the H&K lines (Fig. A.7).

4.11. Titanium lines

Figure A.4 shows the contribution by titanium to the spectrum, which can be seen to be significant. Titanium is an effective line blocking agent, and provides much of the quasi-continuum through scattering and fluorescence at early times.

4.12. Iron lines

Figure A.4 shows the contribution by Fe I, Fe II and Fe III to the model spectrum. These components are strong at all times. The iron lines arise from both cooling and recombination of the iron from decayed ^{56}Co, but also from scattering in this component and from primordial iron in the rest of the nebula.

The most distinct iron lines emerging in the model are [Fe II] λ7155, [Fe II] λ1.257 μm, and [Fe II] λ1.644 μm, but also a [Fe II] complex between 1.27-1.32 μm, [Fe II] λ1.534 μm, and [Fe II] $\lambda\lambda$1.801, 1.810 μm are quite distinct. Most of these lines appear to be present in the spectra of SN 2011dh (Figs. 1, 2).

The [Fe II] λ7155 line has an excitation temperature of 22 800 K whereas the [Fe II] λ1.257 μm line has an excitation temperature of 11 500 K, so their ratio is temperature sensitive. Both lines are optically thin from 100 days in model 12C. In the models, the 4s(a^{4}D) level (giving the [Fe II] λ1.257 μm line) is in LTE for a few hundred days, but 3d^7(a^{2}G) (giving the [Fe II] λ7155 line) is in NLTE already at 100 days. In the LTE and optically thin limit

$$\frac{L_{7155}}{L_{1.26}} \approx 60 \exp\left(-\frac{11\,300\ K}{T}\right). \quad (8)$$

The [Fe II] λ7155 line is quite heavily blended with [Ca II] $\lambda\lambda$7291, 7323 on the red side and He I λ7065 on the blue side, and its flux is therefore hard to determine. At 100 days it is not visible. At 200 days we estimate the [Fe II] λ7155 luminosity to $L_{7155} \approx 4 \times 10^{37}$ erg s^{-1}. The [Fe II] λ1.257 μm line is noisy but we estimate $L_{1.257} \approx 3 \times 10^{37}$ erg s^{-1}, giving a ratio of 1.3. Allowing for a factor two error up and down, the LTE temperature is $T_{\rm LTE} = 3000^{+800}_{-400}$ K. The model temperature in the Fe/Co/He zone is 4000 K at 200 days, in reasonable agreement. The deviation from LTE for level 3d^7(a^{2}G) is about a factor two in the model at this time, which means that the LTE assumption gives a somewhat too low temperature.

For a given temperature, the Fe II mass can be estimated from

$$L_{1.257} = \frac{M({\rm Fe\ II})}{56 m_p} \frac{g_{4s(a^4D)}}{Z(T)} e^{-E_{4s(a^4D)}/kT} A h\nu \quad (9)$$

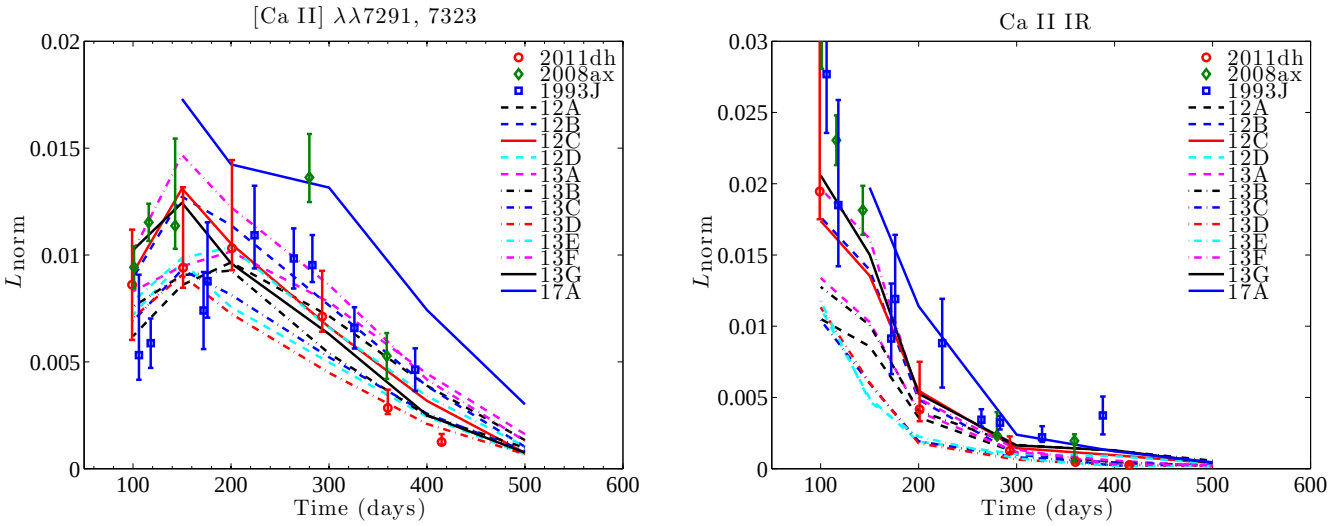

Fig. 21. LEFT : The luminosity in [Ca II] $\lambda\lambda$7291, 7323 relative to the ^{56}Co decay power in SN 1993J, SN 2008ax, SN 2011dh, and in the models. RIGHT : The same for the Ca II IR lines.

which gives M(Fe II) = $0.033^{+0.022}_{-0.017}$ M$_\odot$. Assuming that M(Fe) $\approx$ M(Fe II) and that this iron comes from ^{56}Ni, the initial ^{56}Ni mass is $M(^{56}\mathrm{Ni}) = 0.18^{+0.12}_{-0.090}$ M$_\odot$. The iron lines are thus consistent with of order 0.1 M$_\odot$ ^{56}Ni being synthesized in the SN explosion, although uncertainty in the line luminosity measurements and deviations from the LTE approximation make the exact ^{56}Ni mass more reliably determined from the light curve phase (Bersten et al. 2012, E14b).

4.13. Cobalt lines

Figure A.5 shows the contribution by Co II to the spectrum (contributions by other cobalt ions are negligible). The models predict strong [Co II] $\lambda\lambda$9338, 9344, [Co II] $\lambda\lambda$1.019, 1.025, 1.028 μm, and [Co II] λ1.547 μm at early times, arising from the radioactive ^{56}Co. At later times most of the ^{56}Co has decayed and the lines become weaker. All lines suffers some blending; [Co II] $\lambda\lambda$9338, 9334 with O I λ9263, [Co II] $\lambda\lambda$1.019, 1.025, 1.028 μm with [S II] $\lambda\lambda$1.034, 1.037 μm, and [Co II] λ1.547 μm with [Fe II] λ1.534 μm. The [Co II] $\lambda\lambda$1.019, 1.025, 1.028 μm triplet is the strongest predicted cobalt feature and suffers the least blending of these three, it is therefore the most promising diagnostic of the ^{56}Co mass.

The early spectra of SN 2011dh are consistent with the presence of these lines (Figs. 1 and 2). The satisfactory fit of the modeled [Co II] $\lambda\lambda$1.019, 1.025, 1.028 μm line (as well as the other weaker Co II lines) to the observed line in SN 2011dh (Fig. 2) shows that a synthesized ^{56}Ni mass of 0.075 M$_\odot$ is a good estimate.

4.14. Nickel lines

Figure A.5 (middle) shows the contribution by Ni II to the spectrum (emission from other nickel ions is negligible). The radioactive nickel quickly decays and is not present in large enough quantities to be visible in the nebular phase. However, some stable nickel (mainly ^{58}Ni) is created alongside the ^{56}Ni, which gives rise to [Ni II] $\lambda\lambda$7377, 7411 emission. This doublet will in general blend with the red wing of [Ca II] λ7291, 7323.

Figure A.5 shows that identification of ^{58}Ni may also be done by [Ni II] λ1.939 μm, which arises from the same upper level as [Ni II] $\lambda\lambda$7377, 7411. The day 201 spectrum of SN 2011dh shows an emission line at this wavelength (Fig. 2).

4.15. Other lines

Figure A.5 (lower) shows the contribution to the spectrum by all other elements not covered in previous sections; these are Ne, Al, Ar, Sc, V, Cr, and Mn. It is clear that emission and scattering by these elements make up a relatively minor part of the spectrum, and that the individual elements analyzed in previous sections together account for most the total optical/NIR flux.

4.16. Radiative transfer effects on line profiles

The strong velocity gradients in SN ejecta allow lines to collectively provide significant opacity as photons redshift through a significant wavelength range with respect to the comoving frame as they traverse the ejecta. The collective opacity is referred to as line blocking, and can be significant long after the ejecta have become optically thin in the continuum. This line blocking opacity is especially important in the UV and at short optical wavelengths, where thousands of iron-group lines reside.

Figure 22 shows that the observed line profiles of both [O I] λ5577 and [O I] $\lambda\lambda$6300, 6364 evolve quite significantly between 100 and 200 days in SN 2011dh. At 100 days the peaks of the lines are both blue-shifted by $\sim$1500 km s^{-1}. A plausible interpretation is that this arises as a result of line blocking, which preferentially absorbs emission from the receding side of the ejecta, and is an effect which diminishes with time. Note that the Na I-D line is not noticeably affected, as it is mainly formed by scattering in the envelope (giving a P-Cygni like profile) and experiences little transfer through the core.

This idea is supported by the radiative transfer simulations which give significant line blocking throughout the optical region at 100 days. In Fig. 23 we show the model spectra at 100 and 200 days zoomed in on the oxygen lines. We obtain significant blue-shifts of [O I] λ5577 and [O I] $\lambda\lambda$6300, 6364 at 100 days, due to a combination of line blending and line blocking of the flux from the receding side (notice the lack of emergent [O I] λ6300 emission redward of 6300 Å). At later times the line

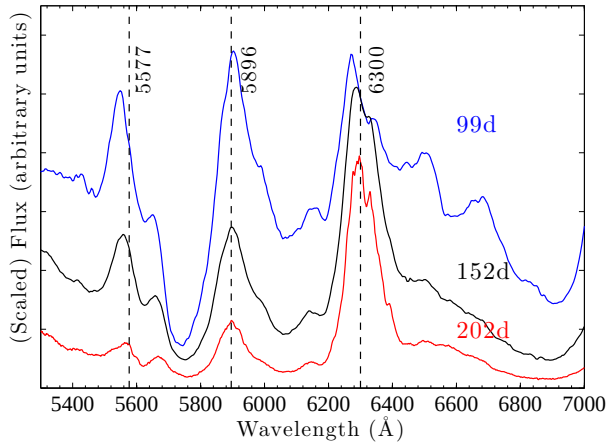

Fig. 22. Zoom-in on the [O I] λ5577, Na I $\lambda\lambda$5890, 5896 and [O I] $\lambda\lambda$6300, 6364 lines in SN2011dh at 99, 152, and 201 days. Both oxygen lines show blue-shifted line profiles at 99 days, but the peaks then gradually move towards zero velocity. The Na I D lines show no blueshift as they mainly arise from envelope scattering (giving a P-Cygni like profile) rather than the obscured core.

blocking decreases and the model gives more symmetric lines profiles, as observed in SN 2011dh.

A similar effect is seen in most other stripped envelope SNe with respect to Mg I] λ4571, [O I] λ5577, and [O I] $\lambda\lambda$6300, 6364 (Taubenberger et al. 2009; Milisavljevic et al. 2010). In SN 2008ax and SN 1993J, the [O I] λ5577 line also showed a $\sim$ 2000 km s^{-1} blue-shifted peak at early times. In SN 2008ax the blue-shift slowly diminished with time (Milisavljevic et al. 2010) but in SN 1993J there was no discernible shift until the line disappeared (Spyromilio 1994).

In cases where line asymmetries persist for several hundred days, ejecta asymmetries are often invoked. The consistency of blueshifts (only unshifted or blueshifted cases were observed for Mg I] λ4571, [O I] λ5577, [O I] $\lambda\lambda$6300, 6364 in a sample of stripped-envelope SNe presented by Milisavljevic et al. (2010)) seem to make both asymmetries and line blending unlikely explanations. The only scenario that can explain such systematic line shifts towards the blue is selective absorption of emission from the receding side of the SN, which as discussed above is seen when the radiative transfer problem is solved (Fig. 23). The temporal decrease of the line blocking depends on the density of the homologously expanding ejecta. One possible scenario is that SNe which show slow line profile changes have higher density ejecta and therefore maintain the line-blocking opacity for a longer time.

Figure 24 shows the integrated line optical depth between λ and $\lambda(1 + V_{\rm core}/c)$ ($V_{\rm core}$ = 3500 km s^{-1}), multiplied by zone filling factor $f_{\rm i}$, for model 13D. This gives some information about the line opacity in the core of the SN. This quantity mainly tells us the wavelength variation of the opacity, and the relative importance of the different zones for the line blocking. Both the iron-group element zones (Fe/Co/He + Si/S) and the oxygen-rich zones (O/Si/S, O/Ne/Mg, O/C) provide significant opacity, with the heavy-element zones providing relatively more opacity at shorter wavelengths.

Figure 25 shows, for model 13E, the escape probability for a photon emitted at the center of the core to reach the surface without being absorbed by a line, computed as

$$P^{\rm esc}(\lambda) = \prod_{\rm i=1}^{\rm Ncore} \prod_{\rm j\in resonance} \left(1 - f_{\rm i}\left(1 - \exp\left(-\tau_{\rm j}\right)\right)\right) \quad (10)$$

where a line belongs to the resonance set if its wavelength is between λ and $\lambda(1 + V_{\rm core}/c)$. The figure demonstrates that below $\sim$6000 Å, the ejecta are opaque for hundreds of days due to line blocking. At longer wavelengths the core is mostly transparent after $\sim$ 200 days, apart from some individual lines such as the Ca II NIR triplet. The emergent spectrum at these wavelength still depends, however, on the radiative transport through the influence of absorption by $\lambda \lesssim 6000$ Å photons on temperature, ionization, and excitation.

Figure 26 shows the time evolution of the escape probability at 4571 and 6300 Å. There is, as expected, a continuous increase of $p^{\rm esc}$ as the optical depths drop with time.

5. Discussion

5.1. Influence of model parameters

5.1.1. Progenitor mass

The model combinations that differ only in the progenitor mass are 12C, 13G, and 17A. Figure 27 shows the optical/NIR spectra of these models at 300 days. As illustrated here (and in Fig. 12) one of the key differences between these models is the [O I] $\lambda\lambda$6300, 6364 luminosity - it is about a factor four higher for ejecta from a 17 M$_\odot$ progenitor compared to a 12 M$_\odot$ progenitor.

The [O I] λ5577 line (which is only visible at earlier times) has a similar dependency on the progenitor mass (Fig. 14), and the [O I] λ5577/[O I] $\lambda\lambda$6300, 6364 ratio is little affected. This can be understood from the fact that we are in the regime where the ejecta are optically thin to the gamma rays, and the energy deposition per unit mass (which governs the temperature) is therefore roughly independent of the ejecta mass. Indeed, we find in the 12C, 13G and 17A models at 300 days an O/Ne/Mg zone temperature of 4000 K, with a variation less than 100 K.

Mg I] λ4571 also becomes stronger for higher progenitor masses (Fig. 27). As the oxygen zone density is similar in the three models, the neutral fraction of magnesium is similar, leading to a small varaition in the relative contributions by collisional excitation and recombination to the Mg I] λ4571 emissivity (Sect. 4.7). The Mg I λ1.504 μm line is weak at 300 days and difficult to discern, but is also stronger for higher mass progenitor models.

As discussed in Sect. 4.6, the Na I D lines have contributions from both a scattering component and a cooling/recombination component from the synthesized sodium. Figure 27 shows that a distinct recombination component is produced in the 17 M$_\odot$ ejecta, clearly distinguishable from the scattering-dominated component seen at lower masses.

The [Ca II] λ7291, 7323 lines also increase in strength with progenitor mass, although quite weakly (Fig. 21). As the [Ca II] $\lambda\lambda$7291, 7323 lines dominate the cooling of the oxygen burning ashes (the Si/S zone), their luminosities are mainly dependent on the mass of this zone. The Si/S zone mass varies only between 0.06 to 0.10 M$_\odot$ over the $M_{\rm ZAMS}$ = 12 – 17 M$_\odot$ range.

Except from very early on, the Ca II IR triplet does not arise from the synthesized calcium (Sect. 4.10), and in these models [C I] λ8727 cooling of the O/C zone overwhelms the Ca II IR

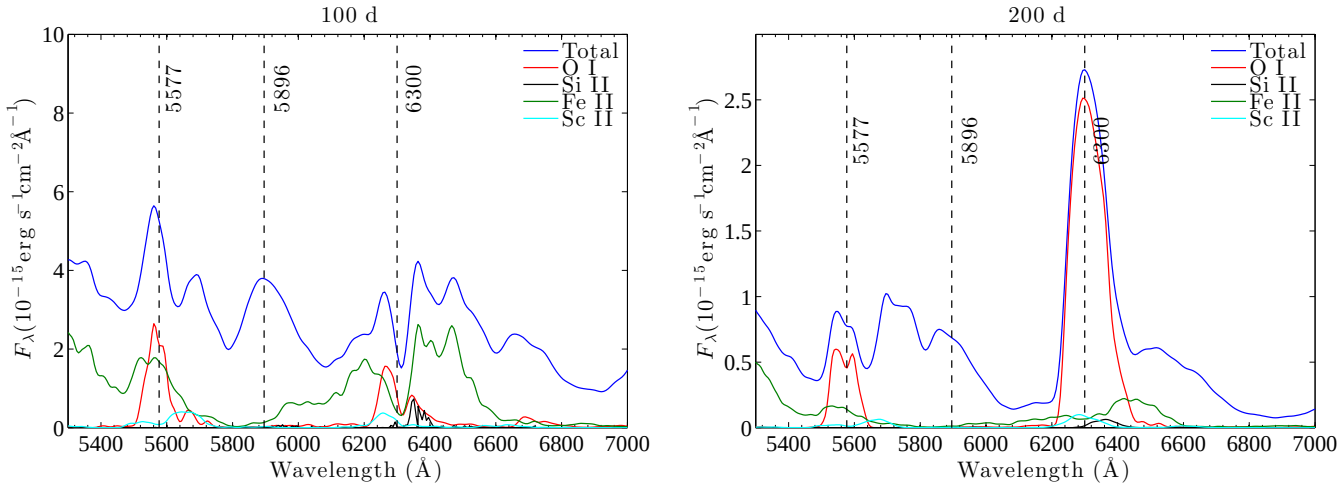

Fig. 23. Model spectra (model 13E, chosen for not having any dust to influence the line profiles) at 100 days (left) and 200 days (right), showing total flux (blue) and the contributions by O I (red), Si II (black), Fe II (green) and Sc II (cyan). Distinct blueshifts of [O I] λ5577 and [O I] $\lambda\lambda$6300, 6364 occur in the model at 100 days, due to a combination of radiative transfer effects (line blocking) and line blending. At 200 days these effects are less severe and the model gives more symmetric line profiles.

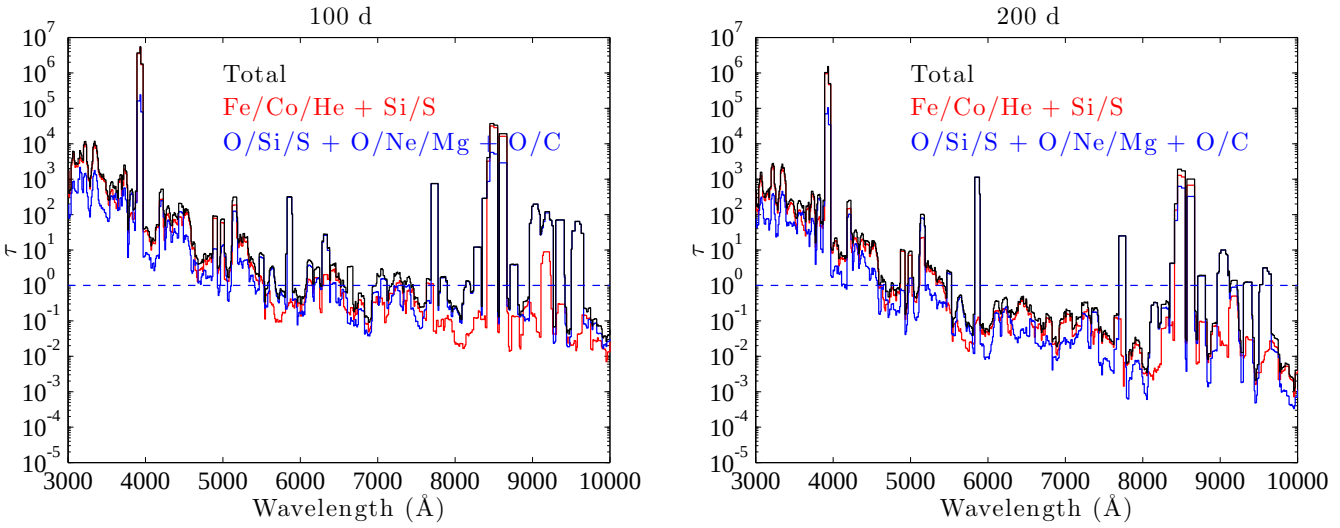

Fig. 24. Integrated optical depth times filling factor ($\tau = f_\mathrm{i} \times \int_\lambda^{\lambda(1+V_\mathrm{core}/c)} \tau_\lambda d\lambda$) in model 13E. The iron-sulphur clumps and the oxygen clumps make similar contributions to the line optical depth.

triplet at 300 days. Higher-mass models therefore give a brighter emission feature at this wavelength (dominated by [C I] λ8727).

In the NIR, the largest differences are seen for [S I] λ1.082 μm, and [Si I] $\lambda\lambda$1.607, 1.646 μm (Fig. 27).

5.1.2. Mixing

The macroscopic mixing of the ^{56}Ni with the rest of the ejecta determines the energy deposition in the various zones. More outmixed ^{56}Ni gives lower total gamma-ray deposition and dimmer nebular spectra (Fig. 28). Very temperature-sensitive lines, such as [O I] λ5577 show the strongest drops when the deposition decreases, but also lines such as [O I] $\lambda\lambda$6300, 6364 and O I λ7774 lose significant luminosity. The lines from the Fe/Co/He zone both become dimmer (because of the lower energy deposition) but also less distinct as the line profile obtains a broader base and a less pronounced peak.

A second effect is that, since different zones have different opacities (due to their differing metal content), the mixing affects the radiative transport and the line blocking effects discussed earlier, but we leave a detailed investigation of this for a future analysis.

5.1.3. Positron trapping

For the first 200-300 days gamma-rays dominate the energy deposition throughout the ejecta, and the treatment of the positrons has little impact. After that time, however, the trapping of the gamma-rays becomes low enough that the positron contribution to the energy budget becomes important and the treatment of where this positron energy is deposited makes a difference for the emergent spectrum.

To study the influence of the positron treatment, we compare models 13A (non-local e^+ absorption) and 13B (local e^+ absorption). The late-time deposition of positron energy in the oxygen

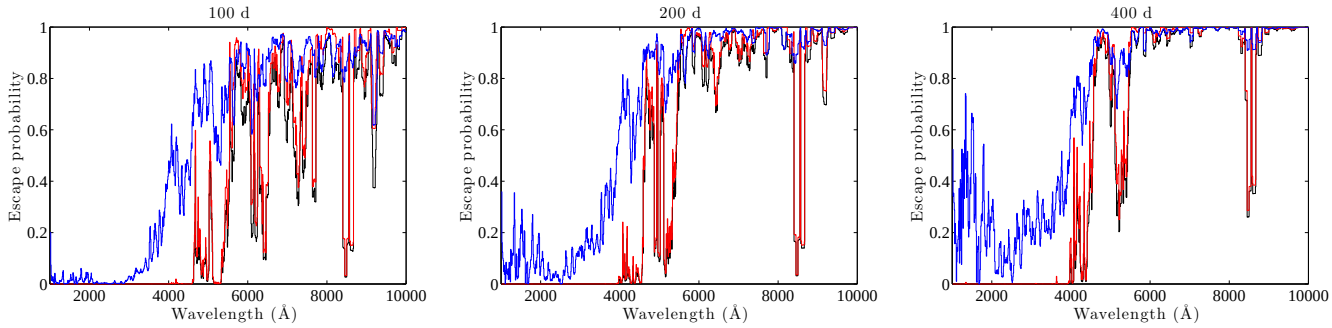

Fig. 25. The escape probability for a photon to pass through 3500 km s^{-1} of core material in model 13E, at 100 (left), 200 (middle) and 400 (right) days (black). Also plotted are escape probabilities to pass through the Fe/Co/He and Si/S clumps (red) and the O/Si/S, O/Ne/Mg and O/C clumps (blue).

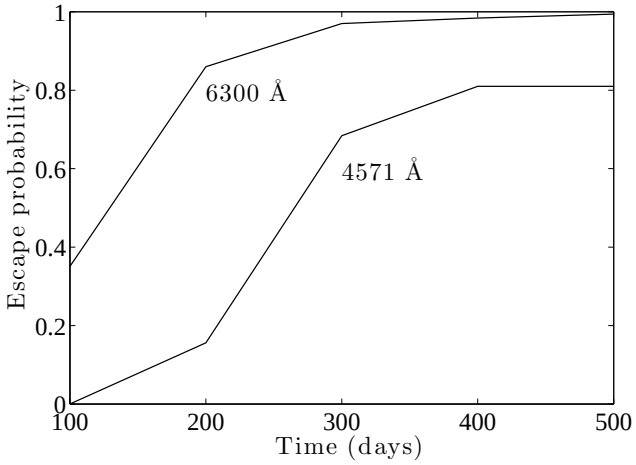

Fig. 26. The core escape probability (from Eq. 10) at 4571 and 6300 Å as function of time, for model 13E.

clumps gives model 13A an [O I] $\lambda\lambda$6300, 6364 doublet that does not fall off in time as observed (Fig. 12), but is too bright after 300 days. The local deposition model (13B) gives a better reproduction of the evolution (but is also somewhat too bright at late times). A caveat here, however, is that if molecular cooling is strongly time-dependent, it could lower both these curves at late times, while changing them little at earlier times. Without a detailed calculation of the molecular cooling (which would need the incorporation of molecular networks such as those described in e.g. Cherchneff & Dwek (2009)), it is therefore difficult to draw firm conclusions regarding the positrons from the late-time behaviour of [O I] $\lambda\lambda$6300, 6364.

The magnesium lines also become brighter with non-local positron deposition (Fig. 19), as the higher electron density produced by the higher ionization level gives stronger recombination.

Figure 29 compares models 13A and 13B at 400 days. As the Fe/Co/He clumps receive less energy input in the non-local model, they are cooler and emit weaker lines. The [Co II] $\lambda\lambda$1.109, 1.025, 1.028 μm feature is about 1/3 weaker in model 13A than in 13B. Unfortunately, at the time of the last NIR spectrum in our data set (200 days for SN 2011dh), the difference for this line, as well as for the iron lines, is not yet large enough (of order 10%) to differentiate between the scenarios. In the optical, however, [Fe II] λ7155 is observed at late times. With local positron absorption, this line is significantly stronger than with non-local absorption. The observed line at late times in SN 2011dh appears to fit the non-local scenario better (Figs. 1, 29), although the vicinity to the strong [Ca II] doublet complicates the analysis. At 400 days, the non-local model produces no detectable line at all, whereas the local model produces one that is several times too strong, so neither model is fully satisfactory.

Putting all the comparisons with data together, we thus find no model that is fully satisfactory in terms of the positron treatment. It appears that wherever the positrons are taken to deposit their energy, they produce too strong emission lines - too strong [O I] $\lambda\lambda$6300, 6364 if allowed to stream into the oxygen zones, and too strong [Fe II] λ7155 if trapped locally in the iron clumps. The situation is reminiscent of attempts to understand the spectrum of SN 1987A at an age of eight years, where similar results were obtained (but here either [O I] $\lambda\lambda$6300, 6364 or [Fe II] 26 μm were overproduced instead of [O I] $\lambda\lambda$6300, 6364 or [Fe II] λ7155) (Jerkstrand et al. 2011). One possible solution could be significant reemission by dust or molecules from whatever zones the positrons deposit their energy in. This is an attractive scenario given the strong MIR emission observed from SN 2011dh at late times (E14b).

5.1.4. Molecular cooling

Models with molecular cooling have their thermal emission from the O/Si/S and O/C zones damped out. The lines that are mainly affected are [Ca II] $\lambda\lambda$7291, 7323 (from the O/Si/S zone), [S I] λ1.082 μm (O/Si/S zone), [O I] $\lambda\lambda$6300, 6364 (O/Si/S and O/C zones), and [C I] λ8727 (O/C zone). As Fig. 30 shows, the impact is significant on the cooling lines of [O I] λ5577 and [O I] $\lambda\lambda$6300, 6364, [C I] λ8727 (a strong coolant of the O/C zone in the absence of CO cooling) and [S I] λ1.082 μm and [Ca II] $\lambda\lambda$7291, 7323 (strong coolants of the O/Si/S zone in the absence of Si/O cooling). The observed blend of the Ca II IR triplet and the [C I] λ8727 line at 200 days is better reproduced in models with no CO cooling than those with complete CO cooling (as seen by comparing Fig. 1 (middle) and Fig. 30), suggesting that CO cooling still plays a minor role at this time.

The impact of the molecular cooling depends on the progenitor mass, as the relative masses of the O/Si/S, O/Ne/Mg, and O/C zones vary significantly with progenitor mass. For instance, at $M_{\rm ZAMS}$ = 12 M$_\odot$, these zone masses are 0.12, 0.13 and 0.15 M$_\odot$, whereas at $M_{\rm ZAMS}$ = 18 M$_\odot$ they are 0.24, 1.4 and and 0.55. Since the O/Ne/Mg zone is much more massive than the others in high-mass progenitors, the impact of molecular cooling on the oxygen lines is smaller, since molecules form mainly in the

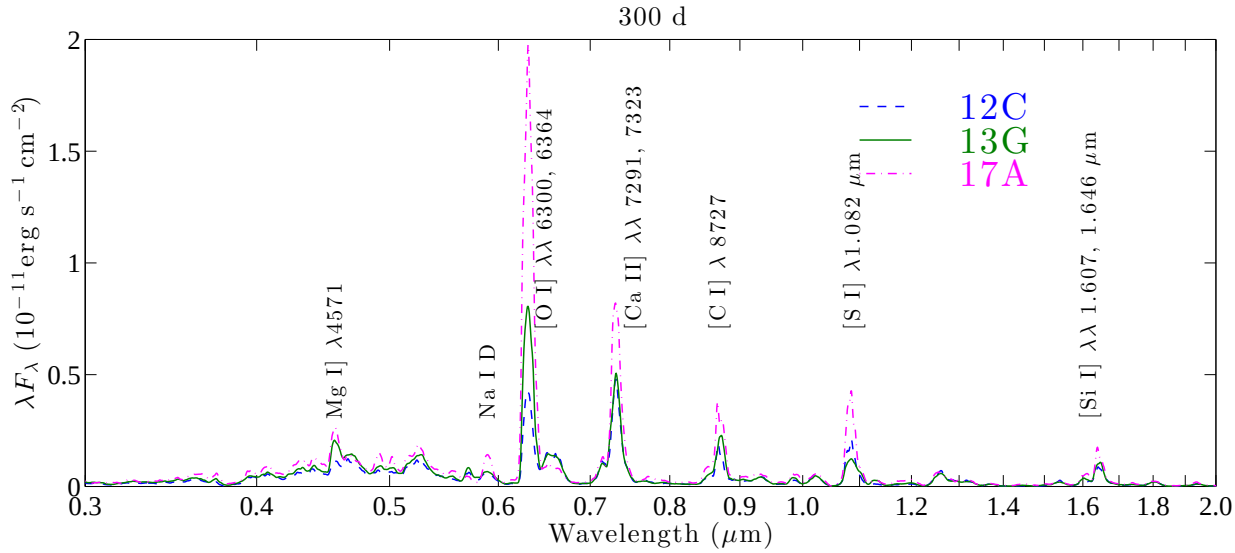

Fig. 27. The optical/NIR spectrum at 300 days for different progenitor masses (models 12C, 13G, and 17A). The most sensitive lines are marked.

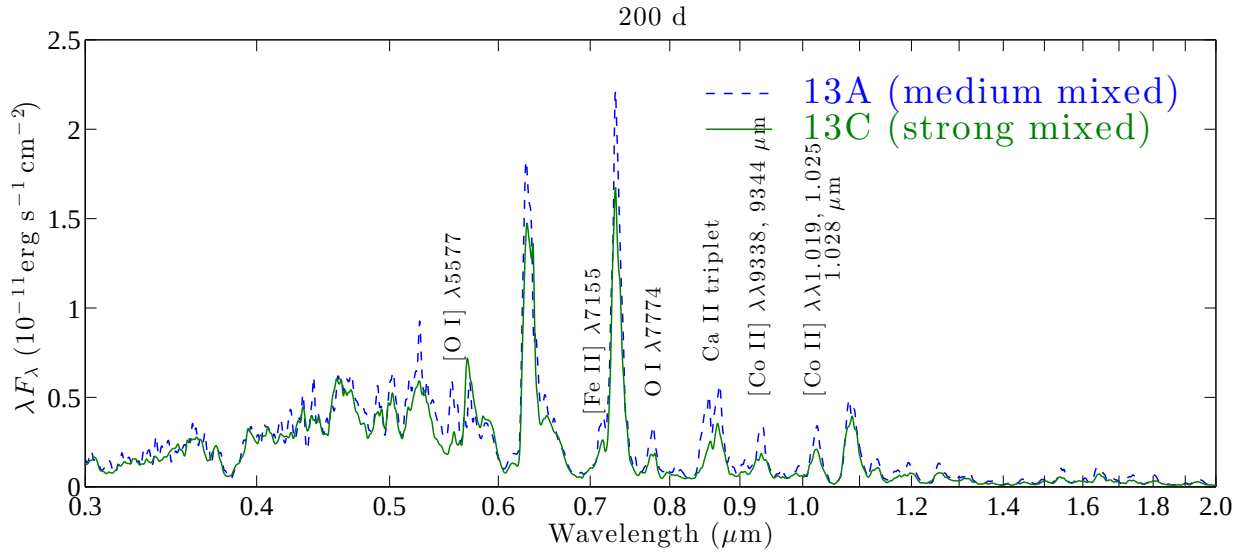

Fig. 28. A comparison of models with medium mixing (13A, blue dashed) and strong mixing (13C, green solid) at 200 days. The lines showing the strongest sensitivity to the mixing are marked.

O/Si/S and O/C zones. The consequence is that the conclusions regarding upper limits to the progenitor masses based on the [O I] $\lambda\lambda$6300, 6364 lines are robust with respect to uncertainties in molecular cooling. A 17 $M_\odot$ model with molecular cooling has only ∼1/3 weaker [O I] λ6300, 6364 emission lines compared to a model without molecular cooling, and still overproduces the observed [O I] $\lambda\lambda$6300, 6364 emission in all three SNe studied here. For low-mass progenitors, on the other hand, ∼2/3 of the oxygen mass is in the the O/Si/S and O/C layers, and the oxygen emission is more sensitive to molecular cooling.

5.1.5. Dust

There are two main influences of dust on the optical/NIR spectrum; the dust suppresses the flux levels approximately by $1 - \exp(-\tau_{\rm dust})$ and secondly it leads to line profile distortions due to the preferential absorption of emission from the receding side. The dominance of radioactivity for the total energy deposition in the various zones means that the influence on physical conditions (temperature, ionization, excitation) through the damping of the radiation field is small.

The emission line profiles become distorted (with blueshifted peaks) due to the preferential blocking of emission from the receding side of the ejecta. In a situation of a uniform distribution of emission and dust absorption, the peaks are blueshifted by an amount given by (Lucy et al. 1991) $\Delta V = V_{\rm emit}\left[(\ln(1+\tau))/\tau - 1\right]$ which is $\sim$ 400 km s^{-1} for $V_{\rm emit}$ = 3500 km s^{-1} and τ = 0.25. This distortion further complicates the interpretation of the observed line profiles, as the mechanism is similar to the one of line opacity discussed in Sect. 4.5. Whereas the line blocking must always decrease with time, dust blocking can both increase and decrease with

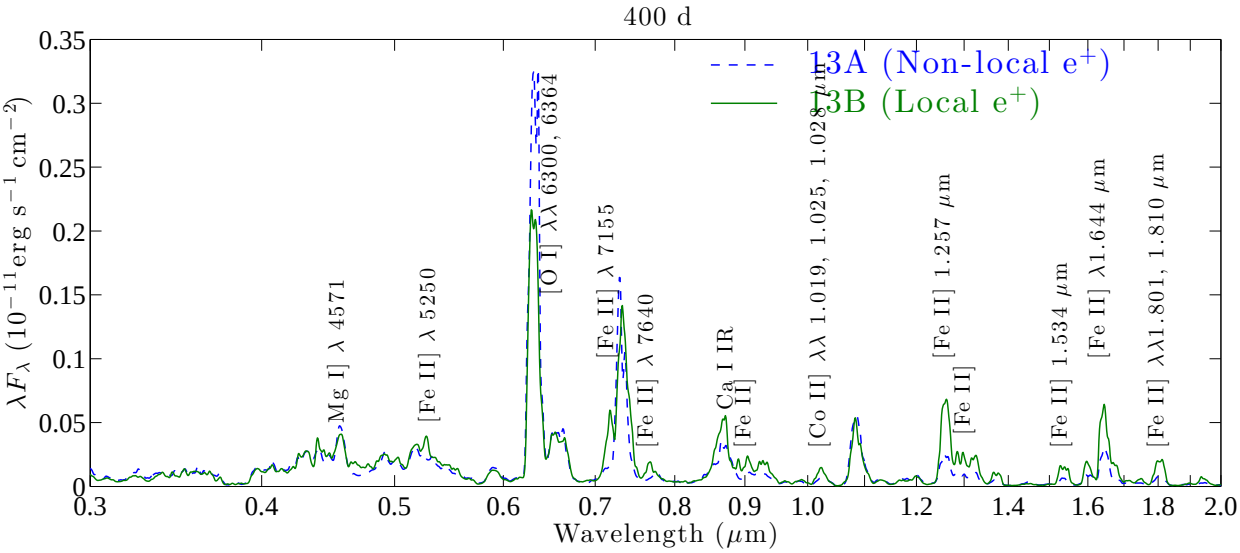

Fig. 29. A comparison of models with non-locally (13A, blue dashed) and locally (13B, green solid) absorbed positrons, at 400 days. The lines showing the strongest sensitivity to the positron treatment are marked.

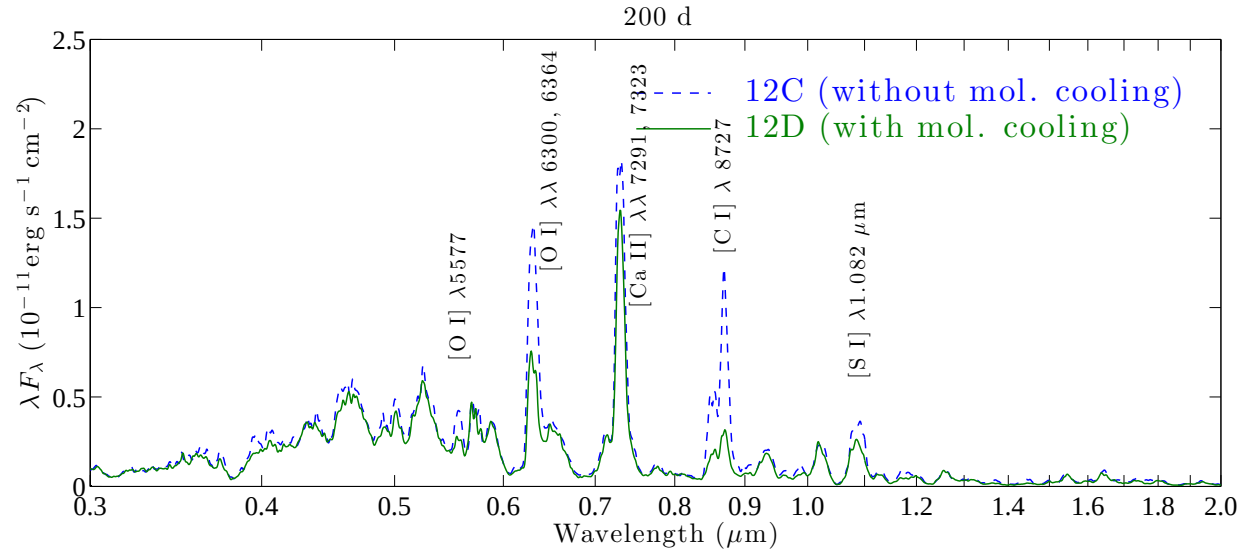

Fig. 30. A comparison of models without (12C, blue dashed) and with (12D, green solid) molecular cooling of the O/Si/S and O/C zones, at 200 days. The lines showing the strongest sensitivity are marked.

time, depending on how the dust formation process evolves. If the dust is optically thin, an increase of its blocking may occur if the dust formation occurs faster than the t^{-2} decline of the column densities. If the dust is optically thick, the blocking will depend on how many optically thick clumps are present at any given time.

5.1.6. Density contrast factor χ

The influence of the core zone densities was discussed in some detail in Sections 4.5 and 4.7 from the perspective of high or low oxygen zone density. To recap, the influence on the [O I] $\lambda\lambda$6300, 6364 cooling lines is relatively small, as oxygen is dominantly neutral over the whole density range analyzed ($\chi = 30 - 210$), reemits a large fraction of the thermal energy deposited in the oxygen clumps, and the fraction of the non-thermal energy going into heating depends only weakly on the density (Kozma & Fransson 1992). That this is the case is evidenced by comparing the strength of the [O I] $\lambda\lambda$6300, 6364 lines between models 13C and 13E, which differ only in contrast factor χ (13C has a low χ (low oxygen zone density) and 13E has high χ (high oxygen zone density)). Figure 31 shows that the [O I] $\lambda\lambda$6300, 6364 lines are ~20% brighter in the high-density model at 300 days, and Fig. 12 shows that this holds true between 100-350 days. After that the low-density model becomes brighter.

The charge transfer quenching of oxygen recombination lines that can occur at high densities (Sect. 4.5) is clearly illustrated in Fig. 31; the high-density model 13E has very weak oxygen recombination lines. For minor species like magnesium

and sodium, higher density instead leads to stronger recombination lines. The situation for these elements is that the radiation field is strong enough to keep them fully ionized over a broad range of densities, rather than becoming more neutral at higher densities as happens with oxygen (a process which is accelerated by charge transfer). The recombination emission is then proportional to the electron density (see Sect. 4.7), which grows approximately with the square root of the density.

6. Summary and conclusions

We have investigated optical/NIR line formation processes in Type IIb SNe from 100 to 500 days post-explosion using NLTE radiative transfer simulations, and compared these models with the three best observed Type IIb SNe to-date; SN 1993J, SN 2008ax, and SN 2011dh. We find the principal components of the model spectra to be cooling and recombination emission from hydrostatic hydrogen burning ashes (He I λ1.083 μm, He I λ2.058 μm, [N II] $\lambda\lambda$6548, 6483), helium burning ashes ([C I] λ8727, [C I] $\lambda\lambda$9824, 9850), carbon burning ashes ([O I] λ5577, [O I] $\lambda\lambda$6300, 6364, O I λ7774, O I λ9263, O I λ1.129 μm + λ1.130 μm, O I λ1.316 μm, Mg I] λ4571, Mg I λ1.504 μm, Na I-D) and from explosive burning ashes ([Si I] λ1.200 μm, [Si I] $\lambda\lambda$1.607, 1.646 μm, [S I] $\lambda\lambda$1.082, 1.311 μm, [Ca II] $\lambda\lambda$7291, 7323, [Fe II] λ7155, and [Co II] $\lambda\lambda$1.019, 1.025, 1.028 μm). These strong emission lines sit atop a quasi-continuum of weaker lines, mainly from iron and titanium, arising by emission as well as scattering/fluorescence from the iron clumps and from the helium envelope. This fluorescent component also produces the Ca II NIR triplet.

Nitrogen left by CNO burning in the helium envelope leads to strong [N II] $\lambda\lambda$6548, 6583 emission lines in the models, which dominate over the Hα emission. We find the H envelopes in Type IIb SNe to have too small mass to produce any detectable Hα, or any other emission lines, after ~150 days post-explosion. Although interaction-powered Hα was clearly present in the spectrum of SN 1993J at late times, our models closely reproduce the evolution of SN 2008ax and SN 2011dh with [N II] $\lambda\lambda$6548, 6483 dominating the emission.

Oxygen and magnesium lines are particularly distinct in Type IIb SNe, and we therefore investigate the diagnostic use of these lines. The cooling lines of [O I] λ5577 and [O I] $\lambda\lambda$6300, 6364 are suitable for estimating the helium core mass of the progenitor. We find that ejecta models from helium cores $M_{\rm He-core} = 3-5$ M$_\odot$ ($M_{\rm ZAMS} = 12-16$ M$_\odot$, oxygen masses $0.3-0.9$ M$_\odot$) satisfactorily reproduce these collisionally excited oxygen lines in all three SNe. Nucleosynthesis analysis thus supports a low/moderate mass origin for Type IIb SNe, and by implication binary progenitor systems.

Magnesium has two distinct emission lines, Mg I] λ4571 and Mg I λ1.504 μm. We find that Mg I] 4571 has contributions from both thermal collisional excitation and recombination, whereas Mg I λ1.504 μm is a recombination line. Based on the regime of physical conditions that the model calculations give, semi-analytical formulae are derived that allows a determination of the magnesium mass from the combined use of magnesium (Mg I λ1.504 μm) and oxygen (O I λ7774, O I λ9263, O I λ1.129 μm + λ1.130 μm, and O I λ1.316 μm) recombination lines. For SN 2011dh, we determine a magnesium mass of $0.03-0.2$ M$_\odot$ which allows for a solar Mg/O production ratio.

We find that the ejecta models investigated here give good reproduction of the near-infrared helium lines in SN 2008ax and SN 2011dh, indicating ejected helium masses of order 1 M$_\odot$. These helium lines are mainly formed by recombination, although cooling and non-thermal excitations contribute at late times to He I λ1.083 μm and He I λ2.058 μm, respectively.

The [Ca II] $\lambda\lambda$7293, 7323 lines constrain the mass of the oxygen burning layer, and we find a good fit with the $0.06-0.11$ M$_\odot$ Si/Si zone used in the models here.

Even as steady-state conditions set in after ~50-100 days in Type IIb and Ib ejecta, the large velocity gradients lead to significant line blocking effects for several hundred days. These radiative transfer effects lead to blue-shifted emission line profiles for lines such as Mg I] λ4571 and [O I] $\lambda\lambda$6300, 6364, an effect which gradually diminishes with time as the densities decrease. The model evolution of this effect reproduces the observed line profile evolution in SN 2011dh well.

For the Type IIb class, observations and modeling of progenitor luminosities, diffusion phase light curves, and nebular phase spectra are at this point in relatively satisfactory agreement with each other regarding at least some physical parameters. Of the three best observed events, at least two (SN 1993J and SN 2011dh) had yellow supergiant progenitors (Aldering et al. 1994; Maund et al. 2011), all three had ejecta masses of ~2-3 M$_\odot$ (Woosley et al. 1994; Bersten et al. 2012, E14b), with nucleosynthesis products (in particular oxygen) in agreement with $12-16$ M$_\odot$ progenitors (Houck & Fransson 1996; Shivvers et al. 2013, this paper). Binary stellar evolution codes can explain the progenitor structures by Roche lobe overflow, although attempts to reproduce the observed rates have so far not been successful (Claeys et al. 2011). The search for a binary companion to SN 2011dh will provide a crucial test for the binary hypothesis, as it did for SN 1993J (Maund et al. 2004).

Appendix A: Element and zone contributions

Figs. A.1 to A.5 show the contribution by all major elements and zones to the emergent spectra in the 100 - 500 day interval, which allows an overview for the various contributions and can be used for future guidance in line identifications.

Appendix B: Code updates

B.1. Lorentz factors

The velocities of stripped envelope core-collapse SNe are high enough (up to $0.1c$) that relativistic effects have some significance. We find that including the Lorentz factor in the Doppler formula

$$\lambda = \lambda' \gamma(v) \left(1 - \frac{v}{c} \cos\theta\right) \quad \text{(B.1)}$$

where λ and λ' are the wavelengths, v is the velocity, c is the speed of light, θ is the angle between velocity and photon propagation direction, and

$$\gamma(v) = \frac{1}{\sqrt{1-(v/c)^2}} \quad \text{(B.2)}$$

produces noticeable wavelength shifts (of order $\gamma \sim 1\%$) in the emergent spectrum, and is therefore applied. The γ factor is more important to include in a co-moving frame code (such as the one used here) compared to a stellar-frame code, as errors due to its omission can accumulate in the series of frame transformations occuring in the co-moving frame treatment.

The relativistic effects on the intensity of the radiation is of less importance, and we postpone a treatment of this for future code upgrades.

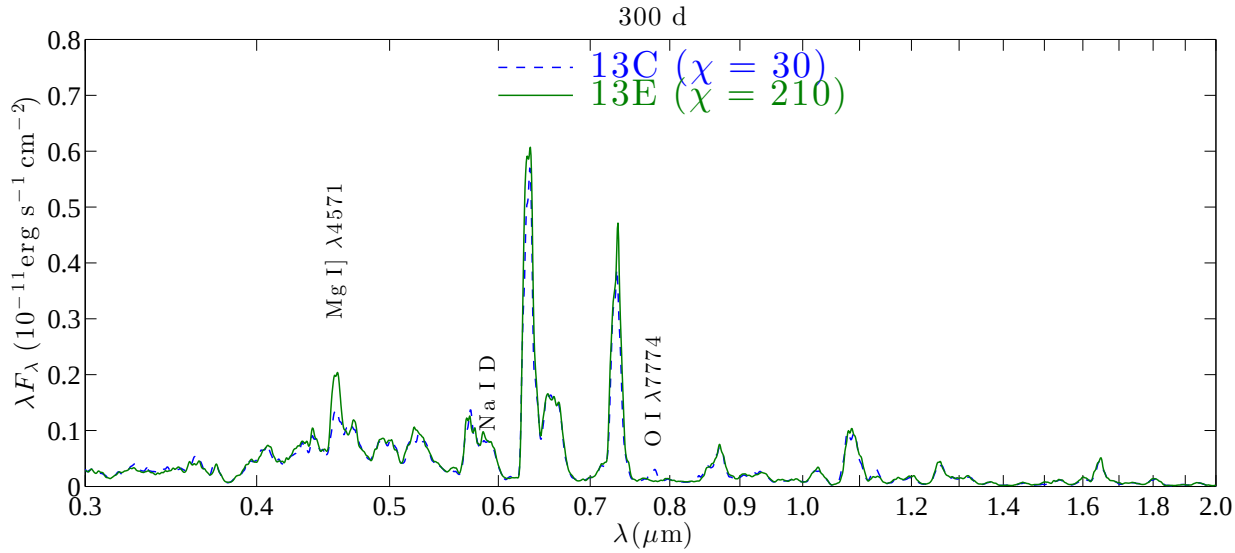

Fig. 31. A comparison of models with low (13C) and high (13E) contrast factor χ, at 300 days. The lines showing the strongest sensitivity are marked.

B.2. Atomic data

- Mg I. Radiative recombination rate updated, now from Badnell (2006). The dielectronic recombination rate is from Nussbaumer & Storey (1986). We compute specific recombination rates by applying the Milne relations to the TOPBASE photoionization cross sections (Cunto et al. 1993) for the first 30 (up to s6d^{1}D) multiplets. For higher states allocation of the remaining part of the total rate occurs in proportion to statistical weights, as described in Jerkstrand et al. (2011). There are some issues with applying the Milne relations to the TOPBASE cross sections; these include ionization to excited states, whereas we need the bound-free cross section for ionization to the ground state of the ion. The first excited state in Mg II has, however, an excitation energy of 4.42 eV, so for the moderate temperatures ($T \lesssim 10^4$ K) of interest here, the contribution by excited states is small, and it is a good approximation to use the full TOPBASE cross sections. Another complication is that the ionization thresholds presented in TOPBASE are often somewhat offset from their correct values. One may choose to renormalize all energies to the correct threshold, here we have not done so (so we simply ignore any listed cross sections at energies below the ionization edge).
  We solve for statistical equilibrium for a 112 level atom (up to 15f(^{3}F), for higher levels our dataset on radiative transitions is incomplete and using a larger atomic model would therefore give a biased recombination cascade).
- Na I. Total recombination rate from Verner & Ferland (1996). Specific recombination rates for first 15 terms (up to 6d^{2}D) computed from TOPBASE photoionization cross sections (same as in Jerkstrand et al. (2011)). The collision strengths come from Trail et al. (1994) for the D line, and from Park (1971) for the other transitions. The Trail et al. (1994) value is in good agreement with the more recent calculation by Gao et al. (2010).
- O I. Specific recombination rates from Nahar (1999) implemented for the first 26 terms (up to 5f^{3}F).
- S I. Forbidden line transition rates updated with values from Froese Fischer et al. (2006).
- Others. Added Ni III, with energy levels from Sugar & Corliss (1985) (up to 3d^8 1G), A-values from Garstang (1958), collision strengths (from ground multiplet only) from Bautista (2001). Added dielectronic recombination rates for Si I, Si II, S I, Ca I, Fe I, and Ni I (Shull & van Steenberg 1982). Added forbidden lines for Fe III, Co III, Al I, Al II, Ti I, Ti II, Ti III, Cr I, Cr II, Mn II, V I, V II, Sc I, Sc II (kurucz.harvard.edu). Added Fe III collision strengths from Zhang & Pradhan (1995b). Fe II collision strengths for the first 16 levels in Fe II now from Ramsbottom et al. (2007) (higher levels from Zhang & Pradhan (1995a) and Bautista & Pradhan (1996)).

Appendix C: Effective recombination rates

We calculate effective recombination rates by computing the recombination cascade in the Case B and Case C limits; here taken to mean that transitions with $A > 10^4$ s^{-1} have infinite optical depth if the lower level belongs to the ground state multiplet (Case B), or to the ground multiplet and first excited multiplet (Case C), and all other transitions have zero optical depth. If all radiative de-excitation channels from a given level obtain infinite optical depth, we let the cascade go to the next level below (mimicking a collisional de-excitation).

Once the effective recombination rate to the parent state of a line has been computed, the rate to use for the line is this value times the fraction of de-excitations going to spontaneous radiative de-excitation in the line, which was computed with the same optical depth treatment as above (for all lines listed here this fraction is close to unity).

C.1. Oxygen

We solve for a 135 level atom (up to 8d(^{3}D)), using total and specific recombination rates from Nahar (1999), which include both radiative and dielectronic recombination. The specific recombination rates were implemented for $n = 1 - 5$, with rates for higher levels being allocated in proportion to the statistical weights.

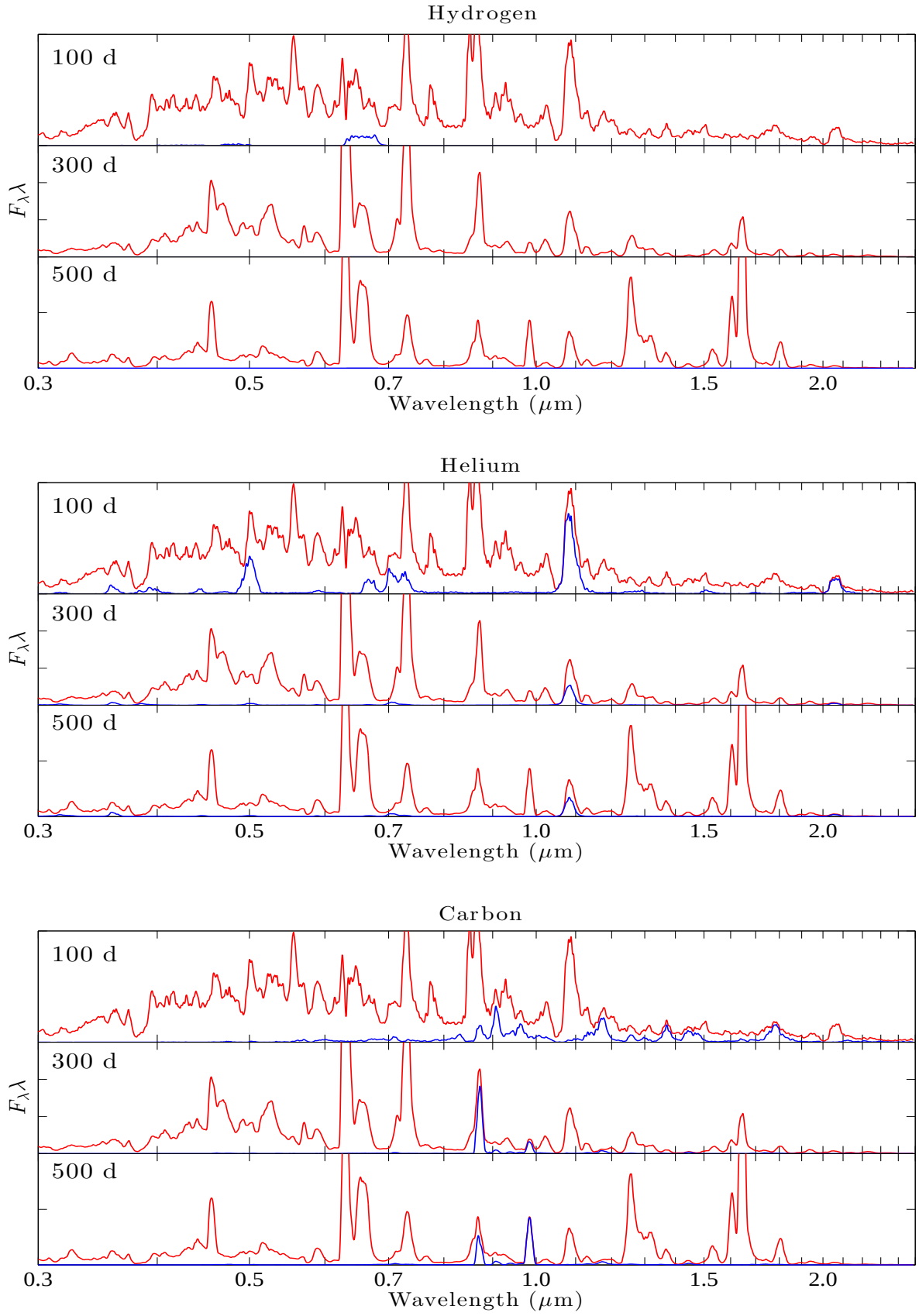

Fig. A.1. TOP : The contribution by H I lines (blue) to the spectrum in model 13G (red), at 100, 300 and 500 days. MIDDLE : Same for He I. BOTTOM : Same for C I.

For the four lines investigated here, three (O I λ7774, O I λ9263, and O I λ1.316 μm) arise from a single parent multiplet. For O I λ1.130 μm, however, both O I 4s(^{5}S)-3p(^{5}P) λ1.130 μm and O I 3d(^{3}D)-3p(^{3}P) λ1.129 μm contribute, and the relevant effective rate for the line is the sum of these.

The resulting values for the effective recombination rates were compared with those computed by Maurer et al. (2010). These include only radiative recombination, bit since dielectronic contribution is relatively weak below 10^4 K, this is a reasonable approximation. Since Table C.1 shows that the agreement is good, within a factor 2 for all lines at all temperatures.

C.2. Magnesium

Table C.2 shows the effective recombination rates computed for Mg I. Note the turn-up at higher temperatures, caused by the dielectronic contribution.

Appendix D: Ejecta models

References

Aldering, G., Humphreys, R. M., & Richmond, M. 1994, AJ, 107, 662
Asplund, M., Grevesse, N., Sauval, A. J., & Scott, P. 2009, ARA&A, 47, 481
Axelrod, T. S. 1980, PhD thesis, California Univ., Santa Cruz.
Badnell, N. R. 2006, A&A, 447, 389
Barbon, R., Benetti, S., Cappellaro, E., et al. 1995, A&AS, 110, 513
Bautista, M. A. 2001, A&A, 365, 268
Bautista, M. A. & Pradhan, A. K. 1996, A&AS, 115, 551
Benjamin, R. A., Skillman, E. D., & Smits, D. P. 1999, ApJ, 514, 307
Bersten, M. C., Benvenuto, O. G., Nomoto, K., et al. 2012, ApJ, 757, 31
Branch, D., Benetti, S., Kasen, D., et al. 2002, ApJ, 566, 1005
Bufano, F., Pignata, G., Bersten, M., et al. 2014, MNRAS, 439, 1807
Cherchneff, I. & Dwek, E. 2009, ApJ, 703, 642
Chiosi, C. & Maeder, A. 1986, ARA&A, 24, 329
Claeys, J. S. W., de Mink, S. E., Pols, O. R., Eldridge, J. J., & Baes, M. 2011, A&A, 528, A131
Colgate, S. A., Petschek, A. G., & Kriese, J. T. 1980, ApJ, 237, L81
Cunto, W., Mendoza, C., Ochsenbein, F., & Zeippen, C. J. 1993, A&A, 275, L5
Dessart, L. & Hillier, D. J. 2011, MNRAS, 410, 1739
Eldridge, J. J., Fraser, M., Smartt, S. J., Maund, J. R., & Crockett, R. M. 2013, MNRAS, 436, 774
Elias, J. H., Matthews, K., Neugebauer, G., & Persson, S. E. 1985, ApJ, 296, 379
Elmhamdi, A., Danziger, I. J., Branch, D., et al. 2006, A&A, 450, 305
Ennis, J. A., Rudnick, L., Reach, W. T., et al. 2006, ApJ, 652, 376
Ensman, L. M. & Woosley, S. E. 1988, ApJ, 333, 754
Ergon, M., Sollerman, J., Fraser, M., et al. 2014a, A&A, 562, A17, (E14a)
Ergon, M., Jerkstrand, A., Sollerman, J., et al. 2014b, A&A, (E14b (in prep))
Ferrarese, L., Ford, H. C., Huchra, J., et al. 2000, ApJS, 128, 431
Filippenko, A. V. 1988, AJ, 96, 1941
Filippenko, A. V., Matheson, T., & Barth, A. J. 1994, AJ, 108, 2220
Filippenko, A. V., Matheson, T., & Ho, L. C. 1993, ApJ, 415, L103
Fransson, C., Challis, P. M., Chevalier, R. A., et al. 2005, ApJ, 622, 991
Fransson, C. & Chevalier, R. A. 1989, ApJ, 343, 323
Fransson, C. & Kozma, C. 1993, ApJ, 408, L25
Freedman, W. L., Hughes, S. M., Madore, B. F., et al. 1994, ApJ, 427, 628
Froese Fischer, C., Tachiev, G., & Irimia, A. 2006, Atomic Data and Nuclear Data Tables, 92, 607
Fryxell, B., Arnett, D., & Mueller, E. 1991, ApJ, 367, 619
Gao, X., Han, X.-Y., Voky, L., Feautrier, N., & Li, J.-M. 2010, Phys. Rev. A, 81, 022703
Garstang, R. H. 1958, MNRAS, 118, 234
Gaskell, C. M., Cappellaro, E., Dinerstein, H. L., et al. 1986, ApJ, 306, L77
Gearhart, R. A., Wheeler, J. C., & Swartz, D. A. 1999, ApJ, 510, 944
Gerardy, C. L., Fesen, R. A., Nomoto, K., et al. 2002, PASJ, 54, 905
Hachisu, I., Matsuda, T., Nomoto, K., & Shigeyama, T. 1991, ApJ, 368, L27
Hachisu, I., Matsuda, T., Nomoto, K., & Shigeyama, T. 1994, A&AS, 104, 341
Hamuy, M., Deng, J., Mazzali, P. A., et al. 2009, ApJ, 703, 1612
Harkness, R. P., Wheeler, J. C., Margon, B., et al. 1987, ApJ, 317, 355
Herant, M. & Benz, W. 1991, ApJ, 370, L81
Houck, J. C. & Fransson, C. 1996, ApJ, 456, 811
Hunter, D. J., Valenti, S., Kotak, R., et al. 2009, A&A, 508, 371
Iwamoto, K., Young, T. R., Nakasato, N., et al. 1997, ApJ, 477, 865
Jerkstrand, A., Fransson, C., & Kozma, C. 2011, A&A, 530, A45
Jerkstrand, A., Fransson, C., Maguire, K., et al. 2012, A&A, 546, A28, (J12)
Jerkstrand, A., Smartt, S. J., Fraser, M., et al. 2014, MNRAS, 439, 3694
Kjær, K., Leibundgut, B., Fransson, C., Jerkstrand, A., & Spyromilio, J. 2010, A&A, 517, A51
Kozma, C. & Fransson, C. 1992, ApJ, 390, 602
Kozma, C. & Fransson, C. 1998, ApJ, 497, 431
Lewis, J. R., Walton, N. A., Meikle, W. P. S., et al. 1994, MNRAS, 266, L27
Li, H. & McCray, R. 1992, ApJ, 387, 309
Li, H. & McCray, R. 1993, ApJ, 405, 730
Li, H. & McCray, R. 1995, ApJ, 441, 821
Li, H. & McCray, R. 1996, ApJ, 456, 370
Li, W., Leaman, J., Chornock, R., et al. 2011, MNRAS, 412, 1441
Liu, W. & Dalgarno, A. 1994, ApJ, 428, 769
Liu, W. & Dalgarno, A. 1996, ApJ, 471, 480
Liu, W., Dalgarno, A., & Lepp, S. 1992, ApJ, 396, 679
Lucy, L. B., Danziger, I. J., Gouiffes, C., & Bouchet, P. 1991, in Supernovae, ed. S. E. Woosley, 82
Matheson, T., Filippenko, A. V., Ho, L. C., Barth, A. J., & Leonard, D. C. 2000, AJ, 120, 1499
Matthews, K., Neugebauer, G., Armus, L., & Soifer, B. T. 2002, AJ, 123, 753
Mauas, P. J., Avrett, E. H., & Loeser, R. 1988, ApJ, 330, 1008
Maund, J. R., Fraser, M., Ergon, M., et al. 2011, ApJ, 739, L37
Maund, J. R., Smartt, S. J., Kudritzki, R. P., Podsiadlowski, P., & Gilmore, G. F. 2004, Nature, 427, 129
Maurer, I., Jerkstrand, A., Mazzali, P. A., et al. 2011, MNRAS, 418, 1517
Maurer, I., Mazzali, P. A., Taubenberger, S., & Hachinger, S. 2010, MNRAS, 409, 1441
Mazzali, P. A., Deng, J., Hamuy, M., & Nomoto, K. 2009, ApJ, 703, 1624
Mazzali, P. A., Maurer, I., Valenti, S., Kotak, R., & Hunter, D. 2010, MNRAS, 408, 87
McCray, R. 1993, ARA&A, 31, 175
Milisavljevic, D., Fesen, R. A., Gerardy, C. L., Kirshner, R. P., & Challis, P. 2010, ApJ, 709, 1343, (M10)
Milisavljevic, D., Margutti, R., Soderberg, A. M., et al. 2013, ApJ, 767, 71
Nahar, S. N. 1999, ApJS, 120, 131
Nomoto, K., Suzuki, T., Shigeyama, T., et al. 1993, Nature, 364, 507
Nomoto, K. I., Iwamoto, K., & Suzuki, T. 1995, Phys. Rep., 256, 173
Nussbaumer, H. & Storey, P. J. 1986, A&AS, 64, 545
Panagia, N., Sramek, R. A., & Weiler, K. W. 1986, ApJ, 300, L55
Park, C. 1971, J. Quant. Spec. Radiat. Transf., 11, 7
Pastorello, A., Kasliwal, M. M., Crockett, R. M., et al. 2008, MNRAS, 389, 955
Patat, F., Chugai, N., & Mazzali, P. A. 1995, A&A, 299, 715
Pequignot, D. & Aldrovandi, S. M. V. 1986, A&A, 161, 169
Podsiadlowski, P., Joss, P. C., & Hsu, J. J. L. 1992, ApJ, 391, 246
Porter, A. C. & Filippenko, A. V. 1987, AJ, 93, 1372
Ramsbottom, C. A., Hudson, C. E., Norrington, P. H., & Scott, M. P. 2007, A&A, 475, 765
Rutherford, J. A., Mathis, R. F., Turner, B. R., & Vroom, D. A. 1971, J. Chem. Phys., 55, 3785
Sana, H., de Mink, S. E., de Koter, A., et al. 2012, Science, 337, 444
Schlegel, E. M. & Kirshner, R. P. 1989, AJ, 98, 577
Shigeyama, T., Nomoto, K., Tsujimoto, T., & Hashimoto, M.-A. 1990, ApJ, 361, L23
Shigeyama, T., Suzuki, T., Kumagai, S., et al. 1994, ApJ, 420, 341
Shivvers, I., Mazzali, P., Silverman, J. M., et al. 2013, MNRAS, 436, 3614
Shull, J. M. & van Steenberg, M. 1982, ApJS, 48, 95
Silverman, J. M., Mazzali, P., Chornock, R., et al. 2009, PASP, 121, 689
Smith, N., Li, W., Filippenko, A. V., & Chornock, R. 2011, MNRAS, 412, 1522
Sollerman, J., Holland, S. T., Challis, P., et al. 2002, A&A, 386, 944
Sollerman, J., Leibundgut, B., & Spyromilio, J. 1998, A&A, 337, 207
Spyromilio, J. 1994, MNRAS, 266, L61
Spyromilio, J. & Pinto, P. A. 1991, in European Southern Observatory Conference and Workshop Proceedings, Vol. 37, European Southern Observatory Conference and Workshop Proceedings, ed. I. J. Danziger & K. Kjaer, 423
Sramek, R. A., Panagia, N., & Weiler, K. W. 1984, ApJ, 285, L59
Stritzinger, M., Mazzali, P., Phillips, M. M., et al. 2009, ApJ, 696, 713
Sugar, J. & Corliss, C. 1985, Atomic energy levels of the iron-period elements: Potassium through Nickel
Tanaka, M., Tominaga, N., Nomoto, K., et al. 2009, ApJ, 692, 1131
Taubenberger, S., Navasardyan, H., Maurer, J. I., et al. 2011, MNRAS, 413, 2140
Taubenberger, S., Valenti, S., Benetti, S., et al. 2009, MNRAS, 397, 677
Timmes, F. X., Woosley, S. E., Hartmann, D. H., & Hoffman, R. D. 1996, ApJ, 464, 332
Timmes, F. X., Woosley, S. E., & Weaver, T. A. 1995, ApJS, 98, 617
Trail, W. K., Morrison, M. A., Zhou, H.-L., et al. 1994, Phys. Rev. A, 49, 3620
Uomoto, A. & Kirshner, R. P. 1985, A&A, 149, L7

Table C.1. Computed effective recombination rates (units cm^3 s^{-1}) for the O I λ7774, O I λ9263, O I λ1.129 μm, O I λ1.130 μm, and O I λ1.316 μm lines. The values are the same for both Case B and Case C (to the accuracy presented here). In parenthesis we show the values computed by Maurer et al. (2010) (pure radiative recombination approximation) for comparison.

Line	2500 K	5000 K	7500 K
	Case B and Case C		
$\alpha_{\rm eff}^{7774}$	$2.8\times10^{-13}(3.1\times10^{-13})$	$1.6\times10^{-13}(1.7\times10^{-13})$	$1.1\times10^{-14}(1.1\times10^{-13})$
$\alpha_{\rm eff}^{9263}$	$1.1\times10^{-13}(1.7\times10^{-13})$	$6.4\times10^{-14}(8.5\times10^{-14})$	$4.5\times10^{-14}(5.5\times10^{-14})$
$\alpha_{\rm eff}^{1.130}$	$6.8\times10^{-14}(5.0\times10^{-14})$	$3.7\times10^{-14}(2.8\times10^{-14})$	$2.6\times10^{-14}(1.9\times10^{-14})$
$\alpha_{\rm eff}^{1.129}$	$1.2\times10^{-13}(1.1\times10^{-13})$	$6.4\times10^{-14}(5.4\times10^{-14})$	$4.4\times10^{-14}(3.5\times10^{-14})$
$\alpha_{\rm eff}^{1.316}$	$4.9\times10^{-14}(2.8\times10^{-14})$	$2.6\times10^{-14}(1.5\times10^{-14})$	$1.8\times10^{-14}(1.0\times10^{-14})$

Table C.2. Computed effective recombination rates (units cm^3 s^{-1}) for the Mg I] λ4571 and Mg I λ1.504 μm lines.

Line	2500 K	5000 K	7500 K
	Case B		
$\alpha_{\rm eff}^{4571}$	7.3×10^{-13}	6.1×10^{-13}	7.7×10^{-13}
$\alpha_{\rm eff}^{1.504}$	5.5×10^{-14}	4.3×10^{-14}	5.7×10^{-14}
	Case C		
$\alpha_{\rm eff}^{4571}$	5.1×10^{-13}	4.7×10^{-13}	6.6×10^{-13}
$\alpha_{\rm eff}^{1.504}$	1.1×10^{-13}	9.7×10^{-14}	1.6×10^{-13}

Table D.1. Zone masses (in $M_\odot$) in the models.

$M_{\rm ZAMS}$ / Zone	Fe/Co/He	Si/S	O/Si/S	O/Ne/Mg	O/C	He/C	He/N	H
12	0.098	0.061	0.13	0.13	0.15	0.15	0.91	0.10
13	0.095	0.068	0.18	0.31	0.25	0.24	0.90	0.10
17	0.10	0.11	0.27	1.2	0.58	0.92	0.22	0.10

Valenti, S., Fraser, M., Benetti, S., et al. 2011, MNRAS, 416, 3138
Van Dyk, S. D., Li, W., Cenko, S. B., et al. 2011, ApJ, 741, L28
Van Dyk, S. D., Zheng, W., Clubb, K. I., et al. 2013, ApJ, 772, L32
Verner, D. A. & Ferland, G. J. 1996, ApJS, 103, 467
Wheeler, J. C. & Levreault, R. 1985, ApJ, 294, L17
Woosley, S. E., Eastman, R. G., Weaver, T. A., & Pinto, P. A. 1994, ApJ, 429, 300
Woosley, S. E. & Heger, A. 2007, Phys. Rep., 442, 269
Woosley, S. E., Pinto, P. A., & Ensman, L. 1988, ApJ, 324, 466
Yoon, S.-C., Woosley, S. E., & Langer, N. 2010, ApJ, 725, 940
Zhang, H. L. & Pradhan, A. K. 1995a, A&A, 293, 953
Zhang, H. L. & Pradhan, A. K. 1995b, Journal of Physics B Atomic Molecular Physics, 28, 3403
Zhang, T., Wang, X., Zhou, X., et al. 2004, AJ, 128, 1857

Acknowledgments

We thank R. Kotak, N. Elias-Rosa, A. Pastorello, S. Benetti, and L. Tomasella for agreeing to the use of proprietary data of SN 2011dh (in particular we acknowledge the use of the William Herschel Telescope, the Gran Telescopio Canarias, the Telescopio Nazionale Galileo, and the Asiago 1.8m telescope). We thank Peter Meikle and Dan Milisavljevic for providing observational data on SN 1993J and SN 2008ax, respectively. Thanks to Nigel Badnell and Sultana Nahar for atomic data discussions. We have made use of observational data provided by the SUSPECT database. This research has been supported by the European Research Council under the European Union's Seventh Framework Programme (FP7/2007-2013)/ERC grant agreement no [291222] (PI: S.J.Smartt). S.T. acknowledges support by TRR 33 "The Dark Universe" of the German Research Foundation.

Table D.2. The zone compositions (mass fractions) of the 12 $M_\odot$ models. Abundances smaller than 10^{-9} are listed as zero.

Element/Zone	Fe/Co/He	Si/S	O/Si/S	O/Ne/Mg	O/C	He/C	He/N	H
^{56}Ni + ^{56}Co	6.5×10^{-1}	1.8×10^{-1}	2.6×10^{-6}	2.2×10^{-5}	1.3×10^{-5}	1.0×10^{-6}	1.1×10^{-7}	0
^{57}Ni + ^{57}Co	3.5×10^{-2}	2.7×10^{-3}	7.7×10^{-6}	1.5×10^{-6}	4.9×10^{-8}	4.4×10^{-9}	2.9×10^{-9}	0
^{44}Ti	5.2×10^{-4}	2.6×10^{-5}	3.0×10^{-7}	0	0	0	0	0
H	5.2×10^{-6}	1.2×10^{-6}	6.2×10^{-8}	7.0×10^{-9}	2.9×10^{-9}	2.0×10^{-9}	6.6×10^{-8}	5.4×10^{-1}
He	2.8×10^{-1}	7.3×10^{-6}	5.3×10^{-6}	4.4×10^{-6}	1.4×10^{-2}	6.7×10^{-1}	9.8×10^{-1}	4.4×10^{-1}
C	2.0×10^{-6}	2.1×10^{-5}	9.0×10^{-4}	3.8×10^{-3}	2.3×10^{-1}	2.7×10^{-1}	2.0×10^{-3}	1.2×10^{-4}
N	3.4×10^{-6}	4.6×10^{-7}	2.6×10^{-5}	4.1×10^{-5}	1.8×10^{-5}	3.5×10^{-6}	7.9×10^{-3}	1.0×10^{-2}
O	2.1×10^{-5}	1.1×10^{-2}	7.6×10^{-1}	6.8×10^{-1}	6.5×10^{-1}	3.3×10^{-2}	8.1×10^{-4}	3.2×10^{-3}
Ne	2.3×10^{-5}	1.5×10^{-5}	1.1×10^{-3}	2.2×10^{-1}	8.2×10^{-2}	1.8×10^{-2}	2.3×10^{-3}	3.0×10^{-3}
Na	9.7×10^{-7}	6.6×10^{-7}	2.5×10^{-5}	4.5×10^{-3}	1.6×10^{-4}	1.9×10^{-4}	1.7×10^{-4}	7.0×10^{-5}
Mg	4.3×10^{-5}	1.1×10^{-4}	3.5×10^{-2}	6.8×10^{-2}	2.5×10^{-2}	8.1×10^{-3}	7.2×10^{-4}	7.2×10^{-4}
Al	8.1×10^{-6}	1.5×10^{-4}	3.8×10^{-3}	5.4×10^{-3}	1.6×10^{-4}	9.7×10^{-5}	7.5×10^{-5}	7.0×10^{-5}
Si	2.2×10^{-4}	3.2×10^{-1}	1.5×10^{-1}	1.4×10^{-2}	1.7×10^{-3}	9.5×10^{-4}	8.2×10^{-4}	8.2×10^{-4}
S	2.2×10^{-4}	3.3×10^{-1}	3.8×10^{-2}	9.2×10^{-4}	2.3×10^{-4}	3.0×10^{-4}	4.2×10^{-4}	4.2×10^{-4}
Ar	2.4×10^{-4}	5.4×10^{-2}	4.2×10^{-3}	8.5×10^{-5}	8.0×10^{-5}	8.4×10^{-5}	1.1×10^{-4}	1.1×10^{-4}
Ca	2.8×10^{-3}	4.2×10^{-2}	9.6×10^{-4}	3.6×10^{-5}	2.5×10^{-5}	3.9×10^{-5}	7.3×10^{-5}	7.4×10^{-5}
Sc	2.3×10^{-7}	4.7×10^{-7}	2.8×10^{-7}	1.1×10^{-6}	1.4×10^{-6}	8.6×10^{-7}	6.6×10^{-8}	4.5×10^{-8}
Ti	1.7×10^{-3}	7.0×10^{-4}	2.4×10^{-5}	5.8×10^{-6}	5.8×10^{-6}	3.5×10^{-6}	3.4×10^{-6}	3.4×10^{-6}
V	5.0×10^{-5}	1.5×10^{-4}	4.5×10^{-6}	6.2×10^{-7}	7.7×10^{-7}	7.6×10^{-7}	4.6×10^{-7}	4.3×10^{-7}
Cr	2.5×10^{-3}	1.1×10^{-2}	7.5×10^{-5}	1.5×10^{-5}	1.2×10^{-5}	1.4×10^{-5}	2.0×10^{-5}	2.0×10^{-5}
Mn	1.8×10^{-6}	3.5×10^{-4}	1.1×10^{-5}	6.9×10^{-6}	4.0×10^{-6}	6.3×10^{-6}	1.6×10^{-5}	1.5×10^{-5}
Fe	8.3×10^{-4}	4.2×10^{-2}	8.0×10^{-4}	8.9×10^{-4}	6.9×10^{-4}	1.1×10^{-3}	1.4×10^{-3}	1.4×10^{-3}
Co	2.3×10^{-8}	1.2×10^{-8}	1.2×10^{-4}	1.4×10^{-4}	1.5×10^{-4}	1.1×10^{-4}	4.8×10^{-6}	4.0×10^{-6}
Ni	2.7×10^{-2}	3.1×10^{-3}	6.9×10^{-4}	4.3×10^{-4}	5.3×10^{-4}	3.2×10^{-4}	8.2×10^{-5}	8.2×10^{-5}

Table D.3. Same as Table D.2 for the 13 $M_\odot$ models.

Element/Zone	Fe/Co/He	Si/S	O/Si/S	O/Ne/Mg	O/C	He/C	He/N	H
^{56}Ni + ^{56}Co	7.7×10^{-1}	7.2×10^{-2}	4.8×10^{-6}	3.0×10^{-5}	1.3×10^{-5}	1.3×10^{-6}	2.5×10^{-8}	0
^{57}Ni + ^{57}Co	3.3×10^{-2}	1.5×10^{-3}	9.6×10^{-6}	1.4×10^{-6}	3.0×10^{-8}	7.4×10^{-9}	3.0×10^{-9}	0
^{44}Ti	2.7×10^{-4}	2.0×10^{-5}	3.1×10^{-7}	0	0	0	0	0
H	5.5×10^{-6}	8.9×10^{-7}	4.5×10^{-8}	3.7×10^{-9}	1.5×10^{-9}	0	1.3×10^{-7}	5.4×10^{-1}
He	1.5×10^{-1}	9.1×10^{-6}	5.0×10^{-6}	3.6×10^{-6}	4.2×10^{-2}	8.2×10^{-1}	9.9×10^{-1}	4.4×10^{-1}
C	3.3×10^{-7}	2.0×10^{-5}	1.3×10^{-3}	6.6×10^{-3}	2.5×10^{-1}	1.5×10^{-1}	4.2×10^{-4}	1.2×10^{-4}
N	2.0×10^{-6}	5.1×10^{-7}	2.9×10^{-5}	3.5×10^{-5}	1.3×10^{-5}	4.1×10^{-5}	8.4×10^{-3}	1.0×10^{-2}
O	9.1×10^{-6}	1.1×10^{-2}	7.5×10^{-1}	7.2×10^{-1}	6.4×10^{-1}	1.3×10^{-2}	7.8×10^{-4}	3.2×10^{-3}
Ne	1.1×10^{-5}	1.8×10^{-5}	2.4×10^{-3}	1.4×10^{-1}	5.6×10^{-2}	1.4×10^{-2}	1.4×10^{-3}	3.0×10^{-3}
Na	7.0×10^{-7}	9.0×10^{-7}	3.7×10^{-5}	9.6×10^{-4}	1.9×10^{-4}	1.9×10^{-4}	1.7×10^{-4}	7.3×10^{-5}
Mg	2.0×10^{-5}	1.4×10^{-4}	4.8×10^{-2}	9.8×10^{-2}	1.5×10^{-2}	1.9×10^{-3}	7.2×10^{-4}	7.2×10^{-4}
Al	1.4×10^{-5}	2.2×10^{-4}	4.7×10^{-3}	8.0×10^{-3}	1.1×10^{-4}	6.5×10^{-5}	7.6×10^{-5}	7.0×10^{-5}
Si	2.9×10^{-3}	3.9×10^{-1}	1.5×10^{-1}	2.3×10^{-2}	9.8×10^{-4}	8.6×10^{-4}	8.2×10^{-4}	8.2×10^{-4}
S	5.5×10^{-3}	3.8×10^{-1}	3.4×10^{-2}	7.1×10^{-4}	2.4×10^{-4}	3.8×10^{-4}	4.2×10^{-4}	4.2×10^{-4}
Ar	1.7×10^{-3}	5.8×10^{-2}	3.8×10^{-3}	8.2×10^{-5}	7.9×10^{-5}	9.7×10^{-5}	1.1×10^{-4}	1.1×10^{-4}
Ca	3.5×10^{-3}	4.0×10^{-2}	1.0×10^{-3}	3.4×10^{-5}	2.7×10^{-5}	6.1×10^{-5}	7.4×10^{-5}	7.4×10^{-5}
Sc	2.2×10^{-7}	4.9×10^{-7}	4.3×10^{-7}	1.5×10^{-6}	1.3×10^{-6}	3.9×10^{-7}	6.1×10^{-8}	4.5×10^{-8}
Ti	8.4×10^{-4}	5.2×10^{-4}	2.3×10^{-5}	5.6×10^{-6}	5.1×10^{-6}	3.4×10^{-6}	3.4×10^{-6}	3.4×10^{-6}
V	3.2×10^{-5}	1.3×10^{-4}	4.2×10^{-6}	6.0×10^{-7}	7.1×10^{-7}	5.2×10^{-7}	4.5×10^{-7}	4.3×10^{-7}
Cr	2.4×10^{-3}	7.0×10^{-3}	7.6×10^{-5}	1.5×10^{-5}	1.2×10^{-5}	1.9×10^{-5}	2.0×10^{-5}	2.0×10^{-5}
Mn	1.7×10^{-5}	2.1×10^{-4}	1.2×10^{-5}	5.7×10^{-6}	4.2×10^{-6}	1.0×10^{-5}	1.6×10^{-5}	1.5×10^{-5}
Fe	2.8×10^{-3}	4.1×10^{-2}	9.3×10^{-4}	8.8×10^{-4}	8.0×10^{-4}	1.3×10^{-3}	1.4×10^{-3}	1.4×10^{-3}
Co	3.1×10^{-8}	1.8×10^{-8}	1.3×10^{-4}	1.3×10^{-4}	1.8×10^{-4}	6.7×10^{-5}	4.4×10^{-6}	4.0×10^{-6}
Ni	3.2×10^{-2}	2.4×10^{-3}	5.9×10^{-4}	4.5×10^{-4}	4.5×10^{-4}	9.3×10^{-5}	8.2×10^{-5}	8.2×10^{-5}

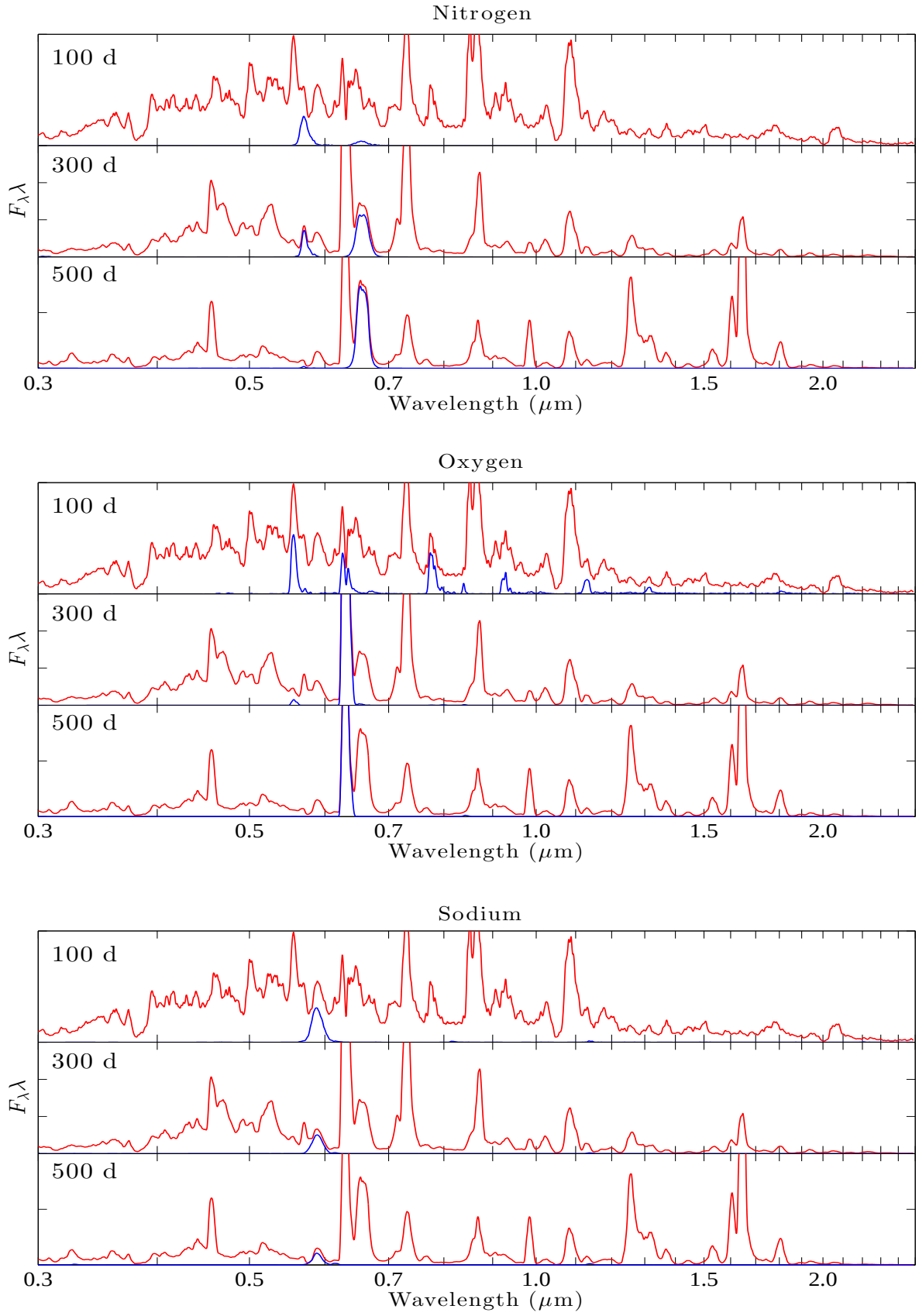

Fig. A.2. TOP : Same as Fig. A.1 for N II. MIDDLE : Same for O I. BOTTOM : Same for Na I.

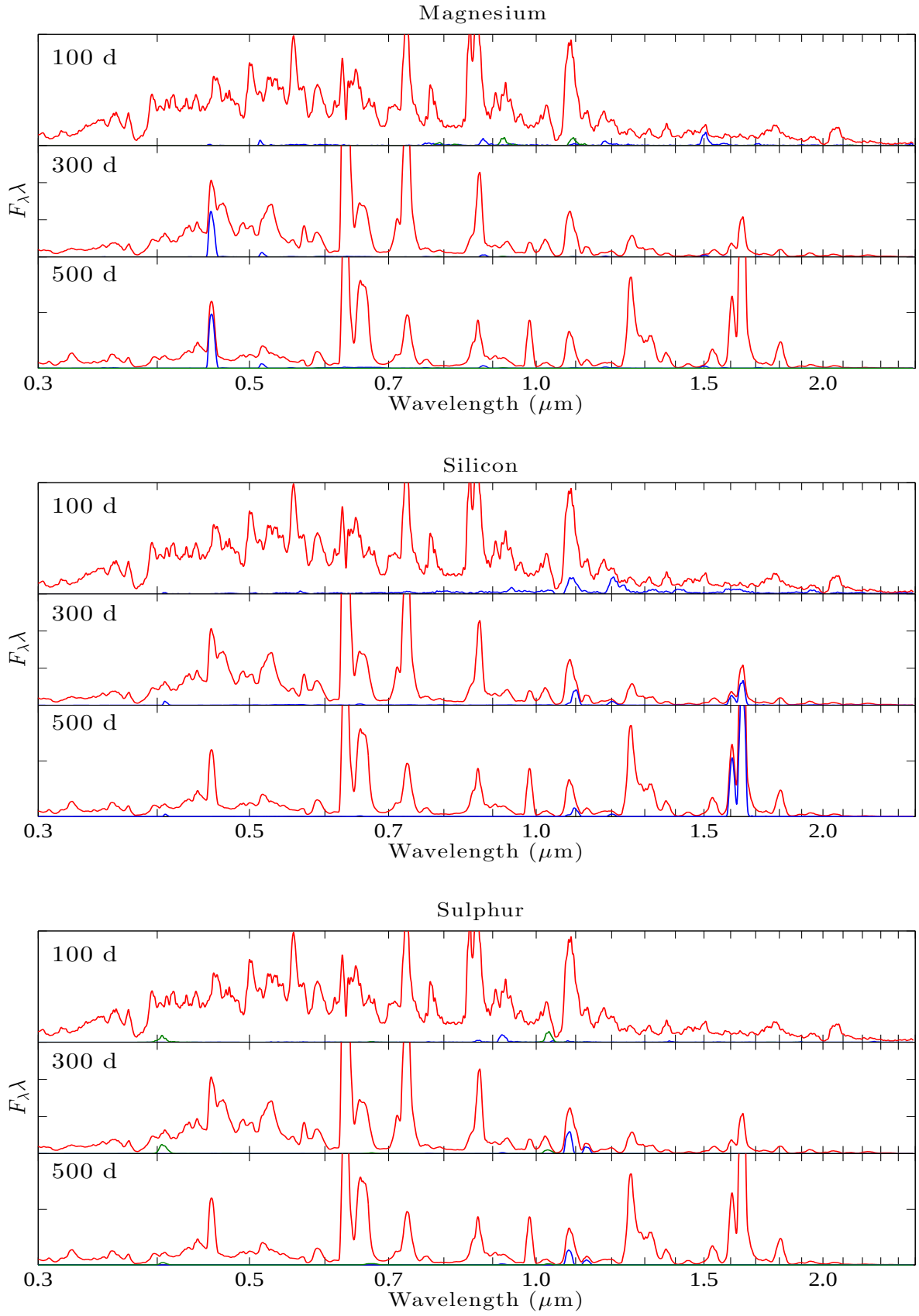

Fig. A.3. TOP : Same as Fig. A.1 for Mg I (blue) and Mg II (green). MIDDLE : Same for Si I. BOTTOM : Same for S I.

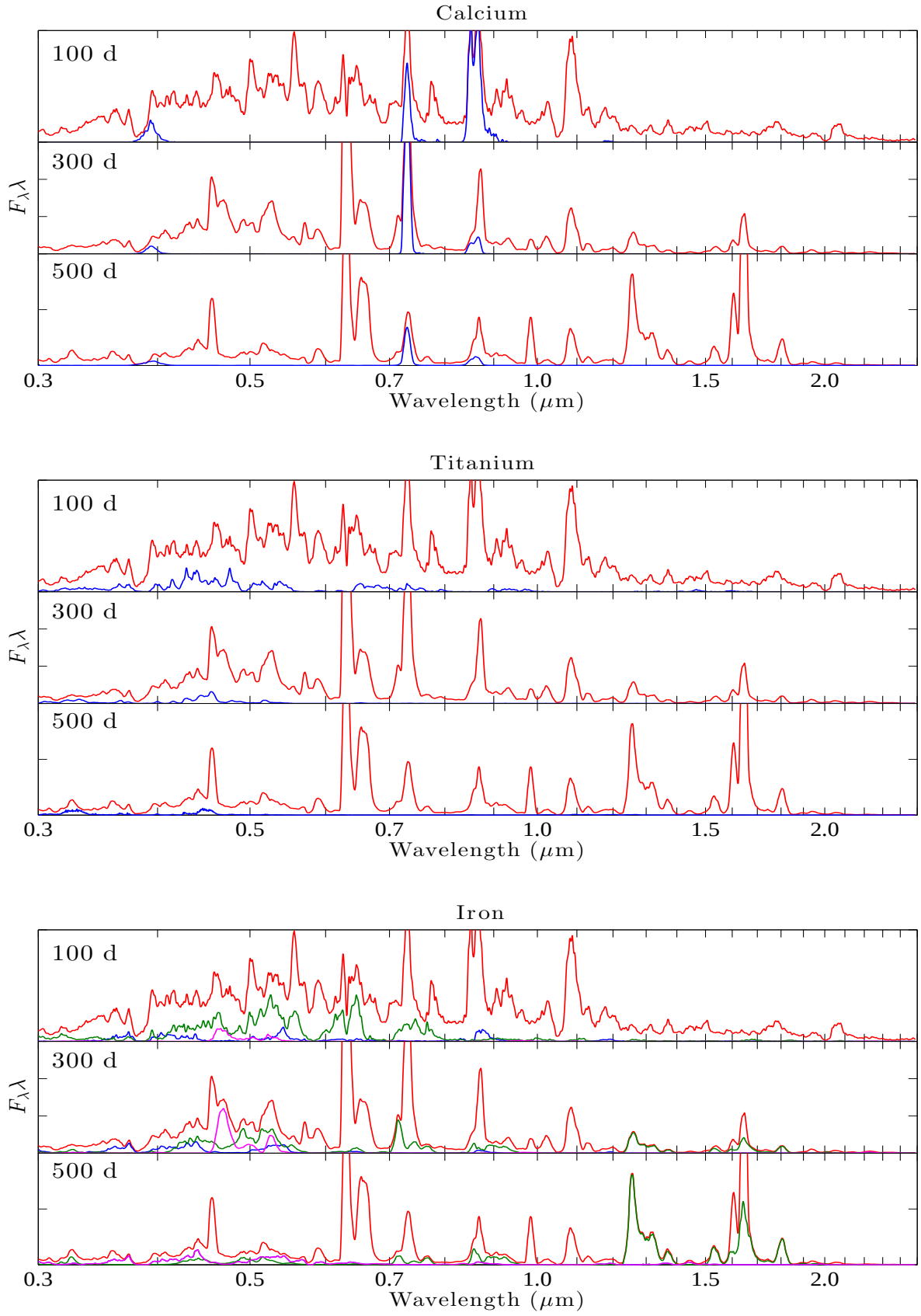

Fig. A.4. TOP : Same as Fig. A.1 for Ca II. MIDDLE : Same for Ti II. BOTTOM : Same for Fe I (blue), Fe II (green) and Fe III (magenta).

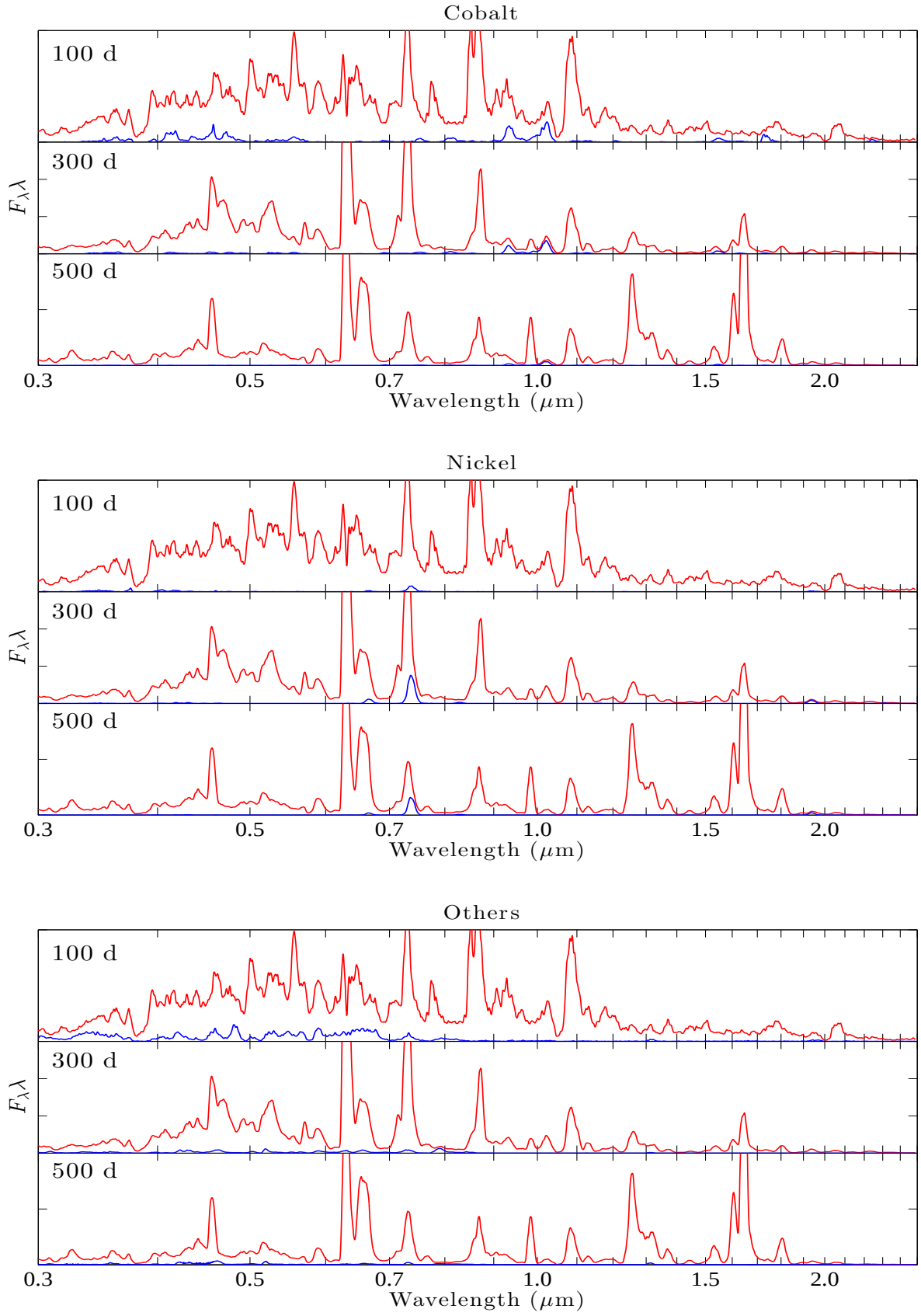

Fig. A.5. TOP : Same as Fig. A.1 for Co II. MIDDLE : Same for Ni II. BOTTOM : Same for all remaining elements.

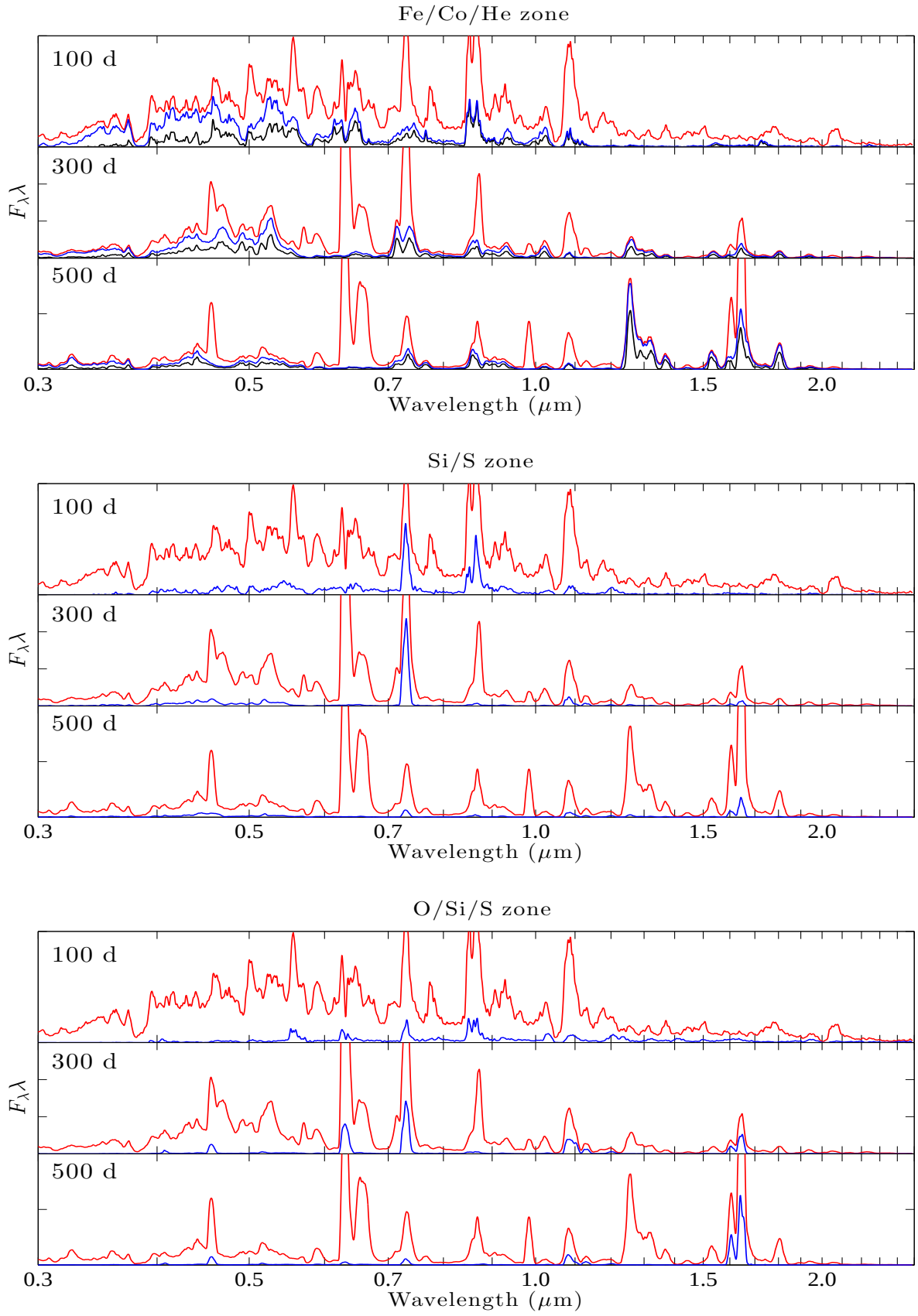

Fig. A.6. TOP : Same as Fig. A.1 for the Fe/Co/He zone (blue is the total contribution, black in the contribution by the Fe/Co/He zone in the core). MIDDLE : Same for the Si/S zone. BOTTOM : Same for the O/Si/S zone.

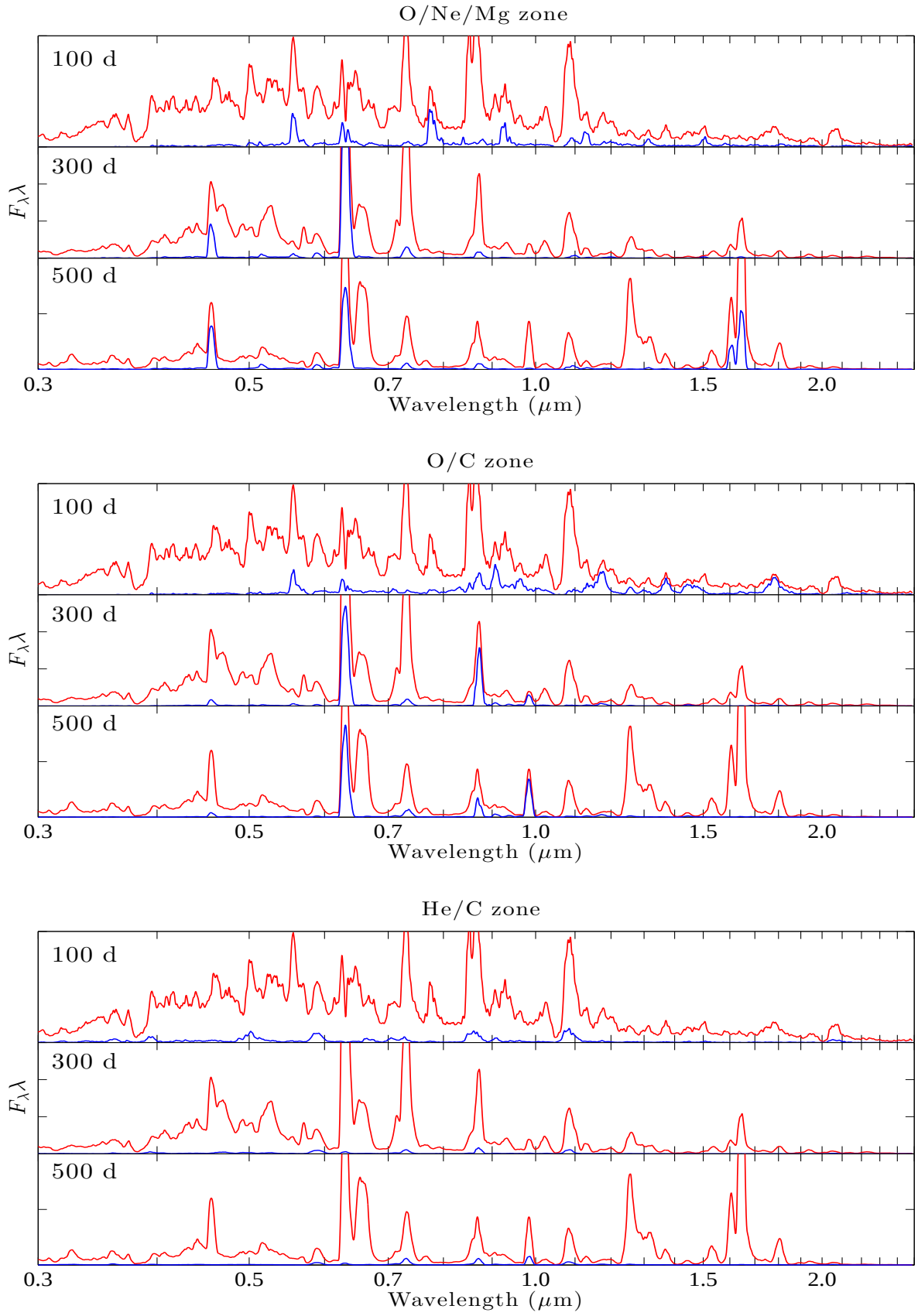

Fig. A.7. TOP : Same as Fig. A.1 for the O/Ne/Mg zone. MIDDLE : Same for the O/C zone. BOTTOM : Same for the He/C zone.

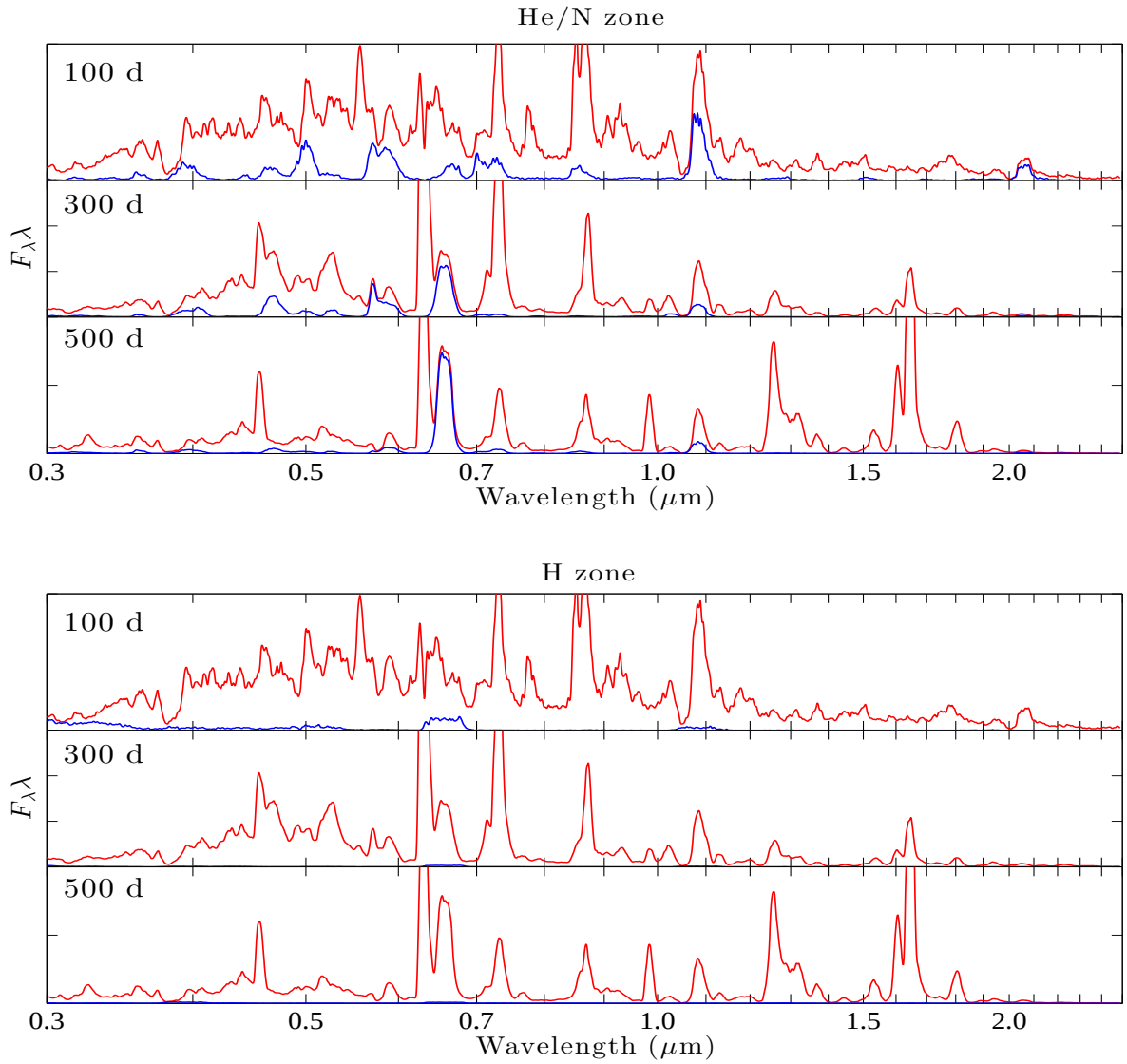

Fig. A.8. TOP : Same as Fig. A.1 for the He/N zone. BOTTOM : Same for the H zone.

Table D.4. Same as Table D.2, for the 17 $M_\odot$ models.

Element/Zone	Fe/Co/He	Si/S	O/Si/S	O/Ne/Mg	O/C	He/C	He/N	H
^{56}Ni + ^{56}Co	7.3×10^{-1}	3.1×10^{-2}	2.9×10^{-7}	1.7×10^{-5}	1.8×10^{-5}	2.6×10^{-7}	2.5×10^{-9}	0
^{57}Ni + ^{57}Co	2.8×10^{-2}	9.2×10^{-4}	1.6×10^{-5}	8.8×10^{-7}	3.0×10^{-8}	6.2×10^{-9}	0	0
^{44}Ti	2.6×10^{-4}	1.3×10^{-5}	5.8×10^{-6}	1.8×10^{-8}	0	0	0	0
H	2.5×10^{-6}	1.2×10^{-7}	6.0×10^{-8}	1.7×10^{-9}	0	0	3.8×10^{-8}	5.4×10^{-1}
He	1.3×10^{-1}	7.7×10^{-6}	3.3×10^{-6}	2.9×10^{-6}	4.5×10^{-2}	9.3×10^{-1}	9.9×10^{-1}	4.4×10^{-1}
C	3.5×10^{-7}	2.0×10^{-5}	6.8×10^{-5}	1.5×10^{-2}	2.4×10^{-1}	4.5×10^{-2}	2.5×10^{-4}	1.2×10^{-4}
N	1.5×10^{-6}	8.0×10^{-7}	1.3×10^{-5}	3.8×10^{-5}	1.1×10^{-5}	1.1×10^{-3}	9.1×10^{-3}	1.0×10^{-2}
O	8.1×10^{-6}	1.6×10^{-2}	2.6×10^{-1}	6.9×10^{-1}	6.8×10^{-1}	1.1×10^{-2}	1.7×10^{-4}	3.2×10^{-3}
Ne	9.3×10^{-6}	2.5×10^{-5}	1.1×10^{-4}	2.1×10^{-1}	2.2×10^{-2}	9.2×10^{-3}	1.1×10^{-3}	3.0×10^{-3}
Na	9.0×10^{-7}	1.1×10^{-6}	1.3×10^{-6}	5.1×10^{-3}	2.0×10^{-4}	1.8×10^{-4}	1.8×10^{-4}	7.9×10^{-5}
Mg	1.9×10^{-5}	1.9×10^{-4}	5.4×10^{-4}	5.8×10^{-2}	6.7×10^{-3}	7.4×10^{-4}	7.0×10^{-4}	7.2×10^{-4}
Al	2.7×10^{-5}	2.8×10^{-4}	2.5×10^{-4}	4.5×10^{-3}	7.4×10^{-5}	7.3×10^{-5}	9.5×10^{-5}	6.9×10^{-5}
Si	1.5×10^{-2}	4.3×10^{-1}	3.5×10^{-1}	1.3×10^{-2}	9.0×10^{-4}	8.3×10^{-4}	8.2×10^{-4}	8.2×10^{-4}
S	2.7×10^{-2}	3.8×10^{-1}	3.2×10^{-1}	2.8×10^{-3}	3.0×10^{-4}	4.1×10^{-4}	4.2×10^{-4}	4.2×10^{-4}
Ar	7.6×10^{-3}	5.3×10^{-2}	5.4×10^{-2}	4.1×10^{-4}	8.6×10^{-5}	1.1×10^{-4}	1.1×10^{-4}	1.1×10^{-4}
Ca	1.1×10^{-2}	3.2×10^{-2}	2.2×10^{-2}	1.5×10^{-4}	4.4×10^{-5}	7.3×10^{-5}	7.4×10^{-5}	7.4×10^{-5}
Sc	3.2×10^{-7}	6.2×10^{-7}	1.3×10^{-6}	1.4×10^{-6}	7.1×10^{-7}	8.8×10^{-8}	4.5×10^{-8}	4.5×10^{-8}
Ti	1.1×10^{-3}	3.2×10^{-4}	1.6×10^{-4}	6.7×10^{-6}	4.9×10^{-6}	3.4×10^{-6}	3.4×10^{-6}	3.4×10^{-6}
V	7.1×10^{-5}	1.2×10^{-4}	1.2×10^{-5}	6.5×10^{-7}	3.2×10^{-7}	4.9×10^{-7}	4.3×10^{-7}	4.3×10^{-7}
Cr	7.4×10^{-3}	4.2×10^{-3}	2.0×10^{-4}	1.4×10^{-5}	1.6×10^{-5}	2.0×10^{-5}	2.0×10^{-5}	2.0×10^{-5}
Mn	1.5×10^{-4}	2.9×10^{-4}	1.7×10^{-5}	5.4×10^{-6}	7.8×10^{-6}	1.6×10^{-5}	1.5×10^{-5}	1.5×10^{-5}
Fe	1.2×10^{-2}	4.8×10^{-2}	1.4×10^{-3}	7.9×10^{-4}	1.0×10^{-3}	1.4×10^{-3}	1.4×10^{-3}	1.4×10^{-3}
Co	3.4×10^{-8}	4.7×10^{-8}	8.7×10^{-7}	1.6×10^{-4}	1.2×10^{-4}	4.8×10^{-6}	4.0×10^{-6}	4.0×10^{-6}
Ni	3.4×10^{-2}	2.3×10^{-3}	8.0×10^{-4}	4.8×10^{-4}	3.1×10^{-4}	8.2×10^{-5}	8.2×10^{-5}	8.2×10^{-5}